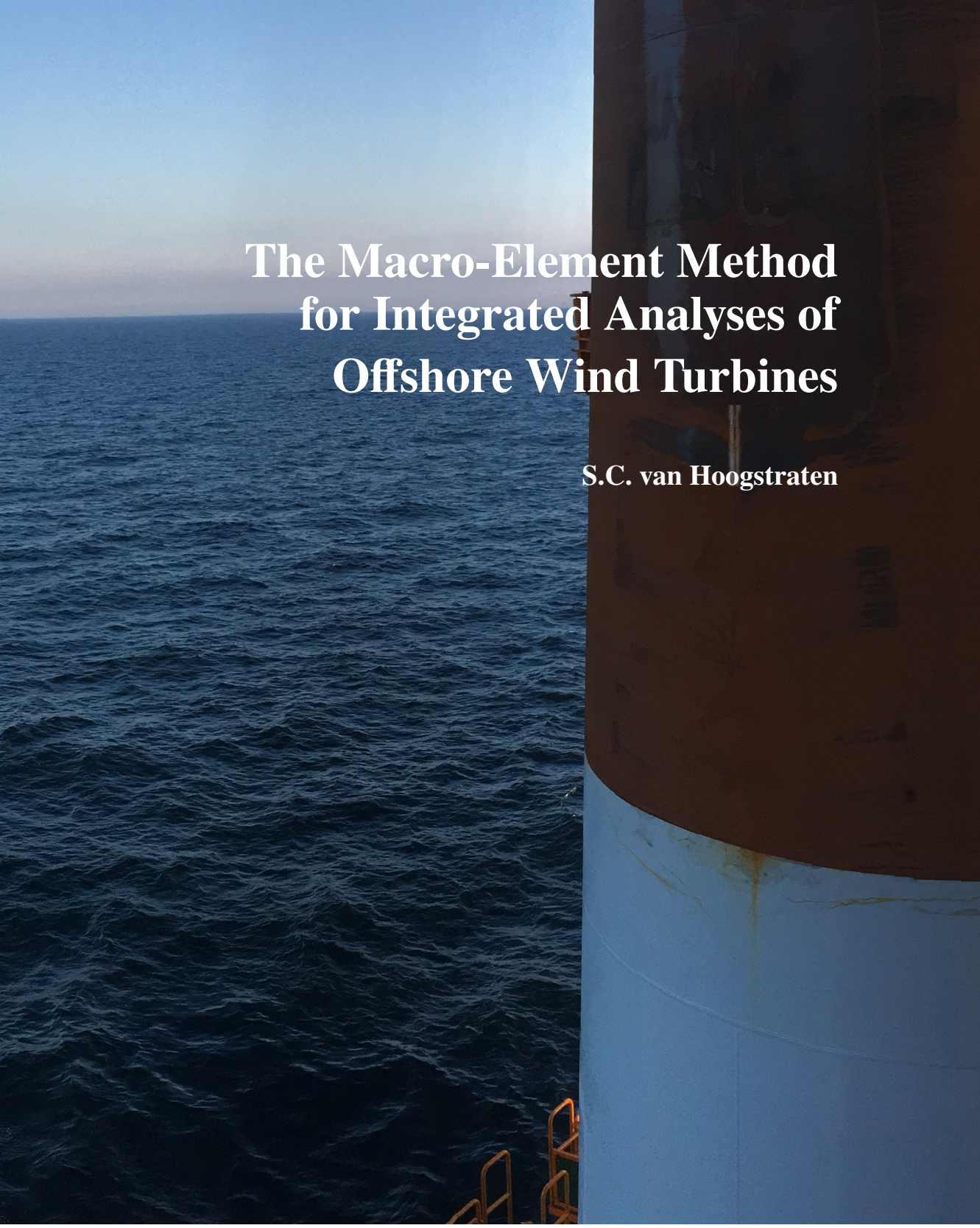

The Macro-Element Method for Integrated Analyses of Offshore Wind Turbines

S.C. van Hoogstraten

TU Delft Delft University of Technology
NGI
NTNU – Trondheim Norwegian University of Science and Technology
SIEMENS Gamesa RENEWABLE ENERGY

The Macro-Element Method for Integrated Analyses of Offshore Wind Turbines

in partial fulfillment of the requirements for the degree of

Master of Science

in *Offshore and Dredging Engineering* at Delft University of Technology and in *Technology-Wind Energy* at the Norwegian University of Science and Technology,

to be defended publicly on the 24th of July 2019.

Author	S.C. van Hoogstraten	
Committee	Prof.Dr. A.V. Metrikine	TU Delft - Chairman
	Dr. F. Pisanò	TU Delft
	Prof.Dr. G. Grimstad	NTNU
	Dr. A.M. Page	Norwegian Geotechnical Institute
	Ir. S.J. Hermans	Siemens Gamesa Renewable Energy
	Dr.Ir. W.G. Versteijlen	Siemens Gamesa Renewable Energy

TU Delft Delft University of Technology · NGI · NTNU – Trondheim Norwegian University of Science and Technology · SIEMENS Gamesa RENEWABLE ENERGY

Cover photo - Walney Extension

Preface

This is the master thesis that is required to obtain the degree of Master of Science in Offshore and Dredging Engineering at Delft University of Technology (TU Delft) and in Technology - Wind Energy at the Norwegian University of Science and Technology (NTNU), which is organised by the Offshore Engineering track of the *European Wind Energy Master*, a joint education program.

The master thesis work was carried out in the collaboration with Siemens Gamesa Renewable Energy (SGRE) in The Hague. The topic was proposed by SGRE and further defined in collaboration with TU Delft, NTNU and NGI. The work was performed during the spring semester of 2019 at SGRE in The Hague.

The summary as included in this thesis is for the major part the same as the abstract I have submitted for the ISFOG 2020 conference.

The Hague, July 18, 2019

S.C. van Hoogstraten

Acknowledgements

I would like to thank the following persons for their great help during the preparation of this master thesis. First and foremost, I would like to express my sincere gratitude to my committee members. From the TU Delft I want to thank Andrei Metrikine and Federico Pisanò. Andrei, thank you for introducing me to the interesting world of non-linear dynamics and your useful comments when I needed to find my way. Federico, thank you for your guidance in our meetings, your constructive feedback has been crucial in the development of this research.

Special thanks to my supervisors of Siemens Gamesa Renewable Energy, Sebastiaan Hermans and Pim Versteijlen. Both your guidance really was invaluable to this work. Thank you for our weekly discussions, where your critical view especially helped me to not get lost in the details. Sebastiaan, thank you for helping to organise my thoughts and introducing me to the 'cookbooks' of an engineer. Pim, I particularly enjoyed our discussions on non-linear dynamics, that really helped me to get a better grasp on the problem.

Besides help from the Netherlands, I was also very lucky to be supported by Gustav Grimstad of NTNU and Ana Page of NGI. Gustav, many thanks for your sharp mind and endless enthusiasm during our thesis discussions, that encouraged me to think critically. Additionally, I owe you a big thanks for finding and solving the bug in the user-defined constitutive model that was used in this thesis. Ana, thank you for sharing your expert knowledge on the macro-element model, this contributed largely to the work.

In addition to the committee members, thanks are given to Michael Armstrong and Axel Nernheim that contributed to this thesis by providing the input data. Further, thanks to Michiel van der Meulen and Gudmund Reidar Eiksund for taking the time to discuss the work.

The past six months at the SGRE office in The Hague have been very *gezellig*, which made the thesis experience so much more enjoyable. Therefore, I would like to thank all the colleagues of the sixth floor, and in particular Adriaan, Ronald, Friso and Tobias, for the

fussball, coffees and regular discussions about the thesis work. Thanks also to Sanne, Jelle, Johan, Matthijs en Wichert for the great experiences of the past two years.

Finally, I want to thank my family and friends for their support during these past months. My endless need to vent about this project must not always have been entertaining, so thank you for your unconditional interest and continuous encouragement.

S.C.v.H.

Summary

Offshore wind energy is considered a necessary renewable energy resource, that may stimulate the transition from fossil fuels. Following the successful development in Western Europe, offshore wind is quickly gaining momentum in the Asia-Pacific region. At variance with North Sea-based offshore wind turbines, structures installed in the Asia-Pacific region are prevalently exposed to typhoons, giving rise to severe wind speeds and, consequently, extreme waves. Such conditions have become design driving for support structures.

Considering that the response of the support structure due to these extreme waves is dependent on soil stiffness, a state-of-the-art foundation model accounting for non-linear, hysteretic soil-monopile behaviour is included in integrated time-domain simulations. Besides considering load-dependent hysteretic damping, the foundation model accounts accurately for the unloading-reloading stiffness. This multi-directional macro-element model has been primarily developed and verified for fatigue limit state analyses. In this thesis, the results of additional 3D finite element verification analyses are presented to identify potential model limitations under ultimate limit state conditions. With regard to different geotechnical and loading scenarios, it is observed that the macro-element model satisfactory predicts load-dependent stiffness and damping, even for the extreme load levels relevant to the Asia-Pacific region.

To capture the offshore wind turbine dynamic response to extreme loading, time-domain analyses are performed with two foundation models: 1) the current industry standard based on non-linear elastic API *p-y* curves, and 2) the non-linear elasto-plastic macro-element model. These models are calibrated against the API *p-y* curves and also against load-displacement curves from 3D finite element analyses. From the models calibrated against the API standard, the effect of accounting for the load-dependent stiffness and damping on the response at interface for extreme load cases is determined. A reduction of the moment at interface level is observed, due to an improved soil stiffness and damping estimation. Further, as the API *p-y* curves do not account for the correct initial stiffness, the response at interface level is additionally evaluated with the macro-element model calibrated to 3D

finite element analyses. The results show a further decrease of the response, that may be attributed to the (initial) stiffer response of the monopile at mudline from 3D finite element analyses.

One of the recommendations is to numerically evaluate the contribution of hysteretic damping with regards to the system damping. Therefore, the validity of the often-used linear damping estimation strategy is investigated for the non-linear system. The interference term in the response at mudline has shown to cause a phase difference, with respect to similar response that does not account for the interference term. The applicability of the logarithmic decrement method that is currently used for system damping estimation is therefore questioned. To evaluate this further, it is suggested to perform additional studies that account for a more adequate representation of the response spectrum.

Contents

Nomenclature

Latin symbols

$\boldsymbol{C}$	damping matrix	[Ns/m]
D	foundation diameter	[m]
f	yield function	-
G	shear stiffness	[m]
H	horizontal load	[kN]
$\boldsymbol{K}$	stiffness matrix	[N/m]
L	foundation length	[m]
$\boldsymbol{M}$	mass matrix	[kg]
M	moment load	[kNm]
N	number of yield surfaces	–
p	lateral soil resistance	[kN/m]
s_u	undrained shear strength	[kN/m^2]
u	displacement	[m]
y	lateral pile deflection	[m]
z	depth	[m]

Greek symbols

α	time integration dissipation parameter	–
δ	logarithmic decrement	–
ϵ	error	–
γ	shear strain	–
ν	Poissons Ratio	–
σ'	effective stress	[kN/m^2]

τ	shear stress	[kN/m^2]
θ	rotation	[rad]
ξ	damping ratio	–

Subscripts

a	average
cyc	cyclic
int	interface level
mp	monopile
$mudl$	mudline
v	vertical
vp	volume pile
x	direction
y	direction
z	direction

Superscripts

$\dot{}$	$\frac{d}{dt}$
e	elastic
ep	elasto-plastic
p	plastic

Abbreviations

BHawC	Load calculation tool Siemens Gamesa
DLC	Design Load Case
DoF	Degree of Freedom
DSS	Direct Simple Shear test
EoM	Equation of Motion
ESS	Extreme Sea State
F-A	Fore-Aft
FEA	Finite Element Analyses
FLS	Fatigue Limit State
FSP	Full Stiffness Profile
HSsmall	Hardening Soil Small Strain
LAT	Lowest Astronomical Tide

log. dec.	logarithmic decrement
(M)N-R	(Modified) Newton-Raphson
MEM1	Macro-element model calibrated against API *p-y* curves
MEM2	Macro-element model calibrated against 3D FEA with HSsmall model
OWE	Offshore Wind Energy
OWT	Offshore Wind Turbine
RSP	Reduced Stiffness Profile
S-S	Side-Side
SGRE	Siemens Gamesa Renewable Energy
SSI	Soil-Structure Interaction
UDSM	User-Defined Soil Model *VonMisesSeriesCoupled*
ULS	Ultimate Limit State

Terminology

Within this thesis, the terminology as shown in Figure 1 is used. The terminology is consistent with the terminology as described by DNV-GL [1].

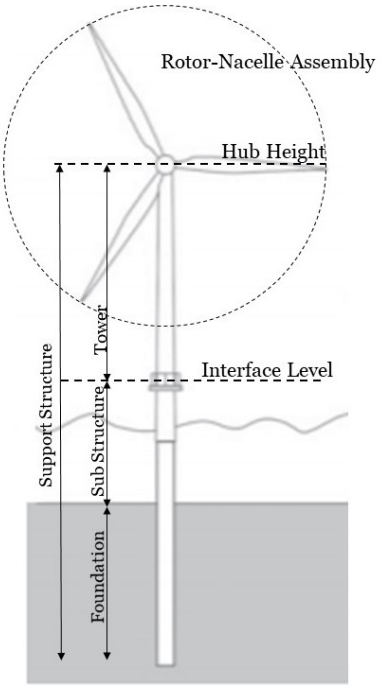

Figure 1: Terminology for an offshore wind turbine in accordance with DNV-GL [1] (adapted from Kallehave et al. [2])

Chapter 1

Introduction

1.1 Offshore Wind Energy

It is broadly accepted by the scientific community that there is a human induced contribution to global warming. Therefore, international agreements are formulated that focus on 1) reducing greenhouse gas emissions and 2) increasing the generation of renewable energy [3, 4]. Complying with these agreements, requires also national efforts: in the Netherlands, for instance, the new Dutch government made the claim to be the 'greenest government ever' [5], based on the newly formulated Climate Agreement. One of the main pillars of the Climate Agreement, is the generation of electricity from renewable resources, predominantly from (offshore) wind energy [6].

Despite most of the wind power capacity currently being installed onshore [7], offshore wind energy (OWE) has some advantages over onshore wind energy due to (stronger and) more consistent winds that are prevalent at sea. Moreover, the power output per site is usually higher, since larger turbines may be installed offshore [8]. As a comparison: in 2017 the average installed onshore and offshore turbine size is 2.7 MW and 5.9 MW at rated power, respectively [7, 9]. On account of this, it is convincing that the Netherlands aims for a majority of offshore wind energy in the renewable energy mix.

However, it is voiced, amongst others by the Netherlands Environmental Assessment Agency [10], that until 2030 the development of offshore wind is limited by the available subsidies. This is related to the fact that the levelised cost of energy (LCoE) is significantly lower for onshore than for offshore wind energy [11]. One of the reasons for the higher LCoE is that offshore wind turbines (OWTs) are exposed to higher loads and stand in the water,

thus requiring larger foundations. IRENA [12] reports that the foundation accounts for 16% of the Capital Expenditures (CAPEX), however, the exact number is site dependent. With increasing water depth, the costs of the foundation rise, as it becomes a larger part of the total structure. Considering that the market trend is to develop offshore wind farms (OWFs) further offshore, in deeper waters and with larger turbines, it is expected that the OWT foundations will increase in size [13].

The other trend that is observed is the decrease in investment costs. Both Ørsted [14] and Vattenfall [15] are developing zero-subsidy OWFs in Germany and the Netherlands, respectively. These are not very exceptional bids, as the low-subsidy bids are seen in the entire industry [16]. Besides the rapid growth of offshore wind energy in Western-Europe, a large expansion of these projects is expected in the Asia-Pacific region [17]. More severe environmental conditions in this region pose a challenge for the development of financial and technical viable projects. Thus, to develop the OWF within the proposed price range design optimisations are essential. As the foundations are a significant part of the CAPEX, it is necessary to review the current foundations and their design procedures.

1.2 Foundations for Offshore Wind Turbines

In Figure 1.1 a selection of foundations for bottom-founded OWTs is shown. Among these, the monopile foundation, a single large diameter tubular pile, is the most common OWT foundation with over 80% of the total installed units in 2017 [7]. Mainly, because monopiles are very suitable for mass-fabrication and have a straightforward installation procedure: pile driving with a hydraulic hammer [2]. Hence, this foundation is often the most cost-effective. As it is expected that this foundation class will remain leading, this thesis will focus on monopile foundations.

However, challenges exist for application of monopiles in the newly announced OWFs, since these encompass deep-water (> 40 m) sites [2]. As a result, due to pile stiffness requirements, the diameter of monopiles is expected to reach 10 m, while current monopile diameters range from 6-8 m [18]. The latter is already a 100% increase from the first generation monopiles, with $D \approx 4$ m. With these large foundations, a design optimisation may result in considerable mass, and thus economical, savings. Haghi et al. [19] analyse the effect of applying integrated design for support structures of OWTs and they report a mass saving of over 10%. In the next paragraph, the integrated design philosophy is outlined.

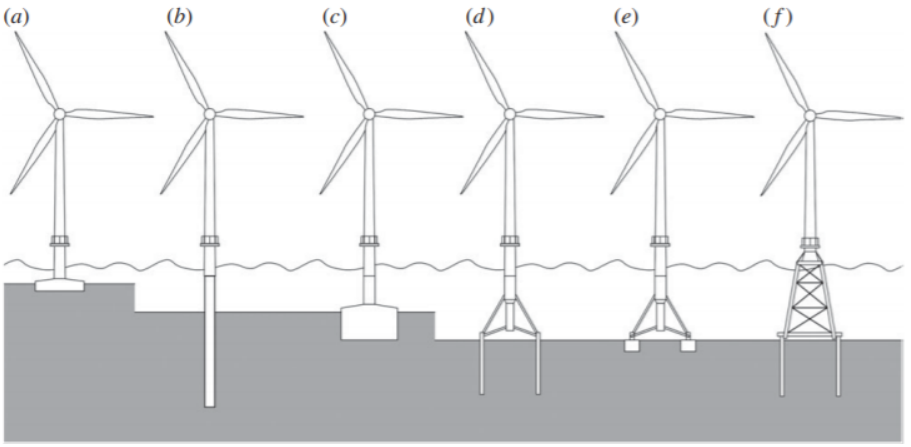

Figure 1.1: Foundation types for bottom founded offshore wind turbines: a) Gravity Based Foundation b) Monopile c) Monobucket d) Multipile foundation e) Multi caisson foundation f) Jacket [2]

Integrated Design for Offshore Wind Turbines

In general, in the design process the OWT tower + rotor-nacelle assembly (RNA) and foundation are separated by a so-called cold-link. This cold-link contains the load and stiffness matrices of the substructure or tower-RNA combination, resulting in an inefficient mass-distribution over the OWT [19, 2]. Thus, to improve the design approach integrated analyses have been proposed, that focus on a simultaneous optimisation of the support structure. It is described by, e.g. Haghi et al. [19], how simultaneously including aerodynamics, hydrodynamics, structural and soil mechanics in design results in a mass reduction of over 10%.

As the dynamic response of the OWT is largely dependent on the foundation behaviour, the soil-structure interaction (SSI) is an important part of the design loop. The SSI describes how the motion of the foundation is influenced by the response of the soil. It is considered that the modelling of SSI is a critical design input for load calculations of the support structure [20]. Therefore, an adequate representation of the SSI in integrated analyses is needed. As the lateral loading for OWTs is dominant over the vertical loading [8], the focus of this thesis is on accurately describing the lateral SSI.

Further, to account for the stochastic offshore environmental loads and system non-linearities, integrated analyses are performed in the time domain, using approximately 120,000 10-

minute load time series per location for an average design case [21]. Hence, there is a need for a computational efficient model that captures the essentials of SSI, like non-linear hysteretic soil behaviour.

Currently, the lateral soil-foundation interaction, is determined by methods described in the design standards, API [22] and DNV-GL [1]. The most common approach uses the so-called *p-y* curves. With this method, the foundation is modelled as a beam that is supported by discrete non-linear elastic springs. This is commonly named a Winkler foundation, as shown in Figure 1.2 [23]. The springs define the SSI, where the stiffness of the springs depends on the ratio between the mobilised lateral soil resistance, p, and the lateral deflection, y. The curves can either be obtained from predefined functions from e.g. *API-RP2A-WSD21* [22] standard or from finite element analysis (FEA).

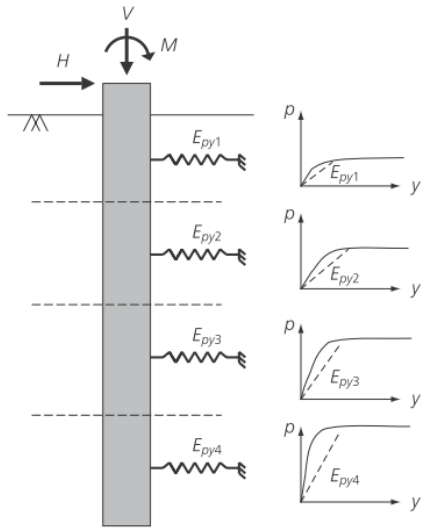

Figure 1.2: A Winkler model for laterally loaded piles [23]

Limitations of the Current Industry Practice in Foundation Modelling

Since some years the validity of the API [22] $p - y$ curves is questioned for application in monopile design, especially for the current and next generation of (X)XL monopiles. Primarily because the initial calibration and application range of the $p - y$ curves was

established for long, flexible piles with high L/D ratios. As a comparison, API [22] *p-y* curves where developed for piles with L/D > 30, while the current generation monopiles reaches an L/D of about 3-5. The latter is due to an increase in the foundation diameter and reduction in pile length, compared to offshore oil & gas piles [23]. Therefore, the main limitations of applying the *p-y* method in OWT foundation analyses are summarised hereafter.

First, as the L/D ratio of the pile decreases the pile behaves more rigidly, with the exact behaviour also dependent on the soil stiffness [23, 24]. As a result, additional soil reactions are induced, specifically a distributed moment along the pile and a moment and horizontal force at the base of the pile [25]. Further, since the $p - y$ curves are elastic, the unloading stiffness is the same as the loading stiffness. In reality, soils exhibit higher stiffness after load reversal. Additionally, the hysteretic damping, that is a consequence of plasticity, is neglected. It is therefore challenged to what extent the $p-y$ curves are a legitimate foundation model in dynamic analyses, as required for OWT foundation design [26].

The effect of the above limitations are observed when results of field investigations are compared to design predictions. Kallehave et al., Hald et al. and Versteijlen et al. [2, 27, 28] show, that the soil-pile stiffness at pile head is largely underestimated with the current method. This results in an underestimation of the natural frequency of the OWT structure. Since the $p - y$ curves overestimate the stiffness at depth, it is deduced that the shallow soil stiffness is of a greater influence on the natural frequency determination [29]. The natural frequency is an important parameter in monopile design and fatigue calculations.

State-of-the-Art Foundation Models

Due to the many concerns regarding the applicability of $p-y$ curves in integrated analyses of the current and next generation monopiles, new foundation models are essential to improve the accuracy in the design and to decrease conservatism. Therefore, multiple research projects have recently focused on improving foundation modelling. An example is the PISA, *PIle Soil Analysis*, joint industry project, that presents rule-based and numerical based methods for modelling the monopile foundation, based on the current *p-y* curve approach [26, 30]. Additionally, as part of the PISA project, Beuckelaers [31] proposes Winkler foundation models that include kinematic hardening and thus also the stiffer unloading of soil. Another method using 1D Winkler models is presented by Versteijlen et al. [21] that describe the non-local model. The non-local model, as opposed to the local model, couples the reaction forces from SSI over the full embedded length of the pile.

Further, the use of macro-element models in integrated design analyses for OWT foundations has recently been proposed by Page [32] and Skau [33]. Macro-element models condense the

response of the entire foundation in load-displacement relations, instead of integrating the *p-y* response along the length of the pile. The use of macro-element models is broadly accepted for design of shallow foundations, with initial research from e.g. Nova and Montrasio [34] for frequency independent and Gazetas [35] for frequency dependent models. The models of Page [32] and Skau [33] are developed as part of the REDWIN project (*REDucing the costs in offshore WINd by integrating structural and geotechnical design*). These macro-element models are computational efficient foundation models, that may provide accurate soil stiffness and damping, dependent on the load level.

It is shown that including the REDWIN model for monopile foundations in integrated design analyses has a positive effect on predicting 1) the natural frequency of the OWT and 2) the fatigue damage [36, 37]. For instance, Page et al. [37] implemented a planar macro-element model in an aero-servo-hydro-elastic code and compared the simulated response of a monopile-based OWT with results from field measurements. In addition, both results were compared with similar analyses, that included the SSI with API and FEA $p-y$ curves. The results demonstrate the inaccuracy of employing API $p-y$ curves for design analyses of more rigidly behaving monopile foundations, and they stress the importance of including hysteretic behaviour. Katsikogiannis et al. [38] use the macro-element model and two other foundation models to evaluate the fatigue sensitivity in different operational states. It is concluded that the impact of accounting for load-dependent stiffness and damping is especially eminent for load cases with insignificant aerodynamic damping.

Currently, the macro-element models are verified and may be used for fatigue limit state (FLS) analyses. In FLS analyses the effect of (small-amplitude) cyclic loading is evaluated. However, for other parts of the support structure and the pile penetration depth the ultimate limit state (ULS) may be governing the design. This is expected to be even more pronounced for recently announced offshore wind farms in the Asia-Pacific (APAC) region with high extreme loads due to the occurrence of typhoons. The multi-directional macro-element model of Page et al. [39], may currently be unsuitable to be employed in integrated ULS analyses, as some of the modelling assumptions may no longer be applicable for the expected load analyses [40].

1.3 Objective and Scope

The objective for the master thesis is to verify and examine the effect of the application of the multi-directional macro-element model of Page et al. [39] in the ultimate limit state. More specifically, to

qualify the impact of accounting for the non-linear hysteretic behaviour of soil in integrated analyses on the support structure design of monopile-based offshore wind turbines in ultimate limit state conditions.

The steps that will be completed in order to realise the objective, is schematically presented in Figure 1.3. The list below elaborates on the steps defined.

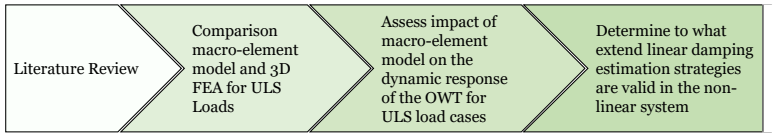

Figure 1.3: Schematic overview of scope of work

- Present a literature review on offshore foundation behaviour, focusing on unloading-reloading of soil, soil-structure interaction when exposed to ULS loads, macro-element foundation models, including formulations and their applicability in integrated dynamic analyses for design of monopile foundations for OWTs. Please note, this part of the scope is performed as part of the project thesis [41]. Chapter 2 of this thesis merely presents a summary of the project thesis.
- Compare the response of the macro-element model and 3D finite element analyses when exposed to ULS loads. The purpose is to assess the effect of the limitations within the macro-element model formulations on the predicted response.
- Include the macro-element model in the foundation design tools of Siemens Gamesa Renewable Energy (SGRE). Evaluate the effect on the dynamic response of the offshore wind turbine by including the macro-element model in integrated analyses for ULS loads.
- Determine to what extend linear damping estimation strategies are valid for the non-linear system, to allow for system damping estimation and, consequently, to identify the hysteretic damping contribution of the macro-element model.

1.4 Outline

In *Chapter 2* some theoretical background to the subject is given. The focus is on monopile foundations, especially the foundation behaviour to cyclic loads, macro-element foundation models and the formulations that the REDWIN models are based on.

Chapter 3 elaborates on the numerical analyses that are performed for the comparative analyses of the macro-element model vs. 3D finite element analyses. This includes the finite element model set-up, the selection of soil parameters and calibration of the numerical models. Also, the results of the comparative analyses are presented. Here, it is observed that for the geotechnical and loading scenarios considered, there is no adaptation of the macro-element model required.

Next, *Chapter 4* presents the results of the case study, that assesses the impact of three foundation models on the dynamic response of an offshore wind turbine exposed to extreme loads in the Asia-Pacific region. As the selected site is still under development, the site and support structure characteristics are normalised.

Chapter 5 discusses the consequences of non-linearity on linear damping estimation techniques, that are currently used to estimate the system damping and the soil damping contribution. Using steady-state forced vibration analyses, an effort is made to compare the response of the non-linear system with an equivalent linear system.

Lastly, *Chapter 6* offers the conclusions and recommendations for further work.

Chapter 2

Theoretical Background

2.1 Introduction

This chapter summarises the literature review that is performed for the project thesis [41]. The parts that are considered extraneous with respect to the research objective, are omitted. Additionally, the sections presented here may have been adjusted to fit the research objective as presented in the previous chapter. First, a concise overview is given on monopile foundation for offshore wind turbines. This concerns design considerations, but most importantly for this research, the foundation behaviour when exposed to cyclic loading. Next, Section 2.3 elaborates on how this offshore foundation behaviour may be captured in a foundation model. Please note, only macro-element models are discussed. For an examination that also includes state-of-the-art Winkler models, reference is made to Page et al. [42] or Chapter 3 of the project thesis, as well as the associated references [41]. Lastly, the multi-surface elasto-plasticity framework as included in the REDWIN macro-element models [33, 39, 40] is explained.

2.2 Monopile Foundations for Offshore Wind Turbines

Currently, monopile foundations are the predominant foundation type for OWTs. Also for new OWFs being developed in areas with deeper waters and increasing turbine sizes the monopile foundation is being considered. Since some time, it is stated by the research community that the current practice in foundation modelling causes conservatism in design

[23, 25, 26]. The current practice, API *p-y* curves, is a result of research efforts on pile foundations from the offshore oil & gas industry. However, the lateral behaviour of offshore oil & gas foundation piles is fundamentally different from monopiles, as cyclic loads from waves and wind determine the design of the OWT foundation [8, 43]. Additional to wave and wind loads, the behaviour of the OWT is influenced by the dynamic excitation its blades [8]. Lastly, there are multiple OWT (foundations) needed for one wind farm. Hence, a design that may be cost-effectively mass produced is required [8, 43]. This section discusses first the design considerations of a monopile foundation, after which the foundation behaviour to cyclic loads is outlined, that should be accounted for in the design of monopile foundations.

Design Considerations

The typically used design code for offshore wind turbine support structures, e.g. DNV-ST-0126 [1], is based on load and resistance factor design (LRFD). Within LRFD, the design is checked in four limit states: the fatigue limit state (FLS), ultimate limit state (ULS), accidental limit state (ALS) and serviceability limit state (SLS). Further, load factors and resistance factors are included to account for uncertainties in the determined loads and material parameters. The cumulative damage on the structure caused by cyclic loading, i.e. stress variations, is assessed in the FLS. As this predominantly concerns low-load levels, the design calculations are typically done for the linear elastic loading regime [1]. For the constructed North Sea wind farms, the FLS is often leading in monopile design [42]. However, for planned OWFs, in deep water and/or typhoon sensitive regions, the ULS may be governing (Siemens Gamesa, internal communication). In an ULS analysis, the maximum load carrying capacity is checked. SLS and ALS focus on verification of the accumulated rotations to be below a threshold and the integrity of the structure to remain intact during or after an accidental load, respectively [1].

Kallehave et al. [2] identify three factors that are leading in monopile design: the pile diameter, the embedded length and the wall thickness over the length of the pile. By optimising these, a 1-2% steel reduction may be achieved. As the OWF is based on multiple foundations, this optimisation may result in a large cost reduction for the whole OWF. From these three factors, the embedded length and the wall thickness are OWT location specific. The pile diameter, though, is set the same for a large part of the OWF, because of fabrication, installation and transportation demands.

The pile diameter is of importance for the natural frequency of the total structure, due to the cyclic and dynamic nature of the OWT loads. Besides cyclic action from wind and wave loading, the rotation of the turbine blades excite a dynamic response on the structure [8]. The blade frequency is referred to as 1P and 3P, the rotational frequency of the turbine

and blade-passing frequency, respectively [2]. Figure 2.1 shows the power spectral density for a monopile-based 10MW+ OWT, that includes the 1P, 3P and environmental loading frequencies. To ensure that the optimum tip speed ratio (λ) is reached for the increased rotor diameter of these turbines, the rotational speed of the rotor is reduced. This affects the 1P and 3P frequency range and thus also the magnitude of the first eigenfrequency (f_0), that is expected to go below 0.2 Hz.

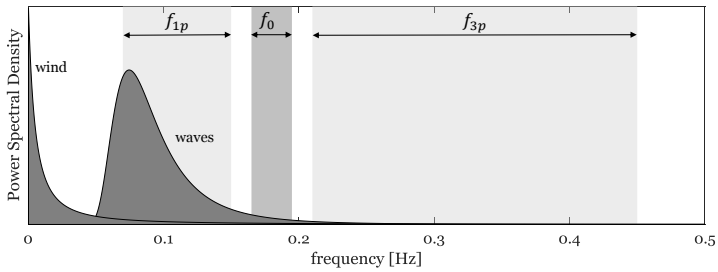

Figure 2.1: Turbine and environmental excitation frequencies for a 10MW+ monopile-based offshore wind turbine (updated after Kallehave et al. [2])

The natural frequency of the structure is commonly placed between the 1P and 3P frequency for monopiles. A foundation where the natural frequency falls in between the 1P and 3P frequency is called soft-stiff. This the result of an economic driver, since a fatigue-wise preferred stiff-stiff support structure (with $f_0 > 3P$), results in monopiles with larger dimensions and higher weight [44].

For increasing water depth and turbine size, the support structure becomes taller and thus, for a constant diameter, its stiffness decreases. To obtain a stiffer support structure, the diameter of the monopile foundation is increased. So, the exact diameter of the monopile is determined by a natural frequency assessment [2]. It is demonstrated, amongst others by Versteijlen et al. [29], that the shallow depth soil stiffness is of a greater importance than the deeper soil layers for natural frequency determination. In current monopile design methods this soil stiffness is not accurately accounted for, which results in an underestimation of the natural frequency and thus an incorrect monopile design, as the fatigue estimation is unreliable [2, 27].

The embedded length of the monopile is determined by assessing the lateral soil capacity to resist the overturning design load [1, 2]. Currently, the lateral soil reaction is evaluated for a pile foundation exposed to ULS load cases. It is then checked if the pile head displacement and rotation are between the limits as specified by DNV-GL [1]. In order to determine if

the chosen pile length is sufficient, a relation between the pile head displacement and pile length may be used to examine the effect of a small change in pile length on the pile head displacement. This relation should show little variation for the chosen embedded depth. In addition, recent developments show that for the next generation monopiles, other soil reactions, like base shear (H_{base}), base moment (M_{base}) and distributed moment (m) should be included [26]. It is expected that these additional soil reactions have an influence on the pile head deflections and thus on the embedded length of the pile. Further, the monopile length should be sufficient to withstand the axial loads. Considering that the axial loads are much smaller than the lateral loads, the pile length is typically decided by the capacity to withstand lateral loads [1]. Moreover, in lateral analyses, the vertical soil mobilisation is not included and vice versa, as the consensus is that the lateral and axial loads activate different parts of the soil.

The third design consideration is the wall thickness of the monopile. The wall thickness is set by results from FLS and buckling analyses, taking into account installation and/or extreme events [2]. In addition, to decrease the risk for buckling, the wall thickness at the pile tip is generally larger, when compared with the remainder of the monopile. The same holds for locations with welded add-ons or exclusions [2].

Foundation Behaviour

The foundation behaviour influences the dynamic response of the OWT [45]. Hence, an accurate description of the SSI is fundamental in performing dynamic analyses. In turn, the foundation response is dependent on the loads that are excited by offshore environment. Subjected to cyclic loading, the soil response will describe a hysteresis loop, Figure 2.2 depicts. Within this loop the stiffness is described by the tangent along the load-displacement curve and is thus changing continuously. This stiffness is denoted as the tangent stiffness. From here on, the tangent stiffness is referred to as 'stiffness'.

The evolution of the stiffness during one load cycle may be deduced from Figure 2.2. First, the soil responds non-linear to the load, during monotonic loading (path *0-1*). During monotonic loading, the stiffness decreases as the load increases. While unloading, the load changes direction, the soil stiffness increases and becomes linear elastic, from *1-2*. If the unloading continues, the displacement path becomes non-linear, resulting in a decrease of stiffness. This path can be observed from *2-3*. At location *3*, the load is reversed and the stiffness from *3-4* is equal to the small-strain elastic stiffness once more. Path *4-1* describes the same load-displacement relation as path *2-3*, although, the load is in opposite direction [46].

For small load levels the foundation behaviour as depicted in Figure 2.2 adheres to the

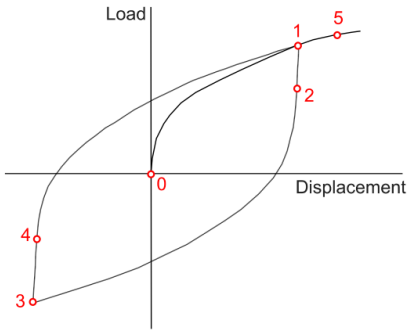

Figure 2.2: Load-displacement curve describing the soil response to cyclic loading on the monopile [46]

(extended) Masing rules [47, 48]. The extended Masing rules consist of four rules defining the hysteretic behaviour that are summarised by, e.g. Abadie et al. [49]. The first two rules state 1) the stiffness upon unloading or reloading matches the initial stiffness of the backbone curve and 2) the shape of the unloading and reloading curve matches the shape of the backbone curve, but is scales by a factor of 2 [47]. The last two rules are formulated by Pyke [48] and can be summarised as 3) when the maximum load is exceeded, the unloading or reloading curve follows again the backbone curve and 4) when an unloading or reloading curve intersects a previous curve, this curve will be followed. For small load levels, the hysteretic loop as defined by the (extended) Masing rules, gives an accurate prediction of the soil-monopile behaviour [49, 50].

The loop that is completed from *1-2-3-4-1* is a full hysteresis loop, where the area under the curve equals the material damping. However, this only holds for low to moderate deformation levels: at large deformations, the damping may be overestimated, since the hysteresis loop under these loads is smaller than the loop described with the Masing rules [50]. Further, Kaynia and Andersen [50] note that soil damping for structures exposed to low frequency loads is mostly material (hysteretic) damping. As OWTs are operating in a low-frequency regime, reference is made to Figure 2.1, it is concluded that an accurate prediction of the hysteretic damping is desirable.

The soil foundation stiffness is not solely described by the above hysteresis loop, since under continuous cyclic loading, displacement accumulation and gapping may occur [42]. Gapping changes the shape of the hysteresis loop to a butterfly or S-shape shape, as is depicted in Figure 2.3. Note that, for the load-displacement curve displayed in Figure 2.3, the tangent

stiffness increases at peak load, while for the remainder of the loop the tangent stiffness is reduced. The stiffness reduction is experienced upon load reversal. While the foundation is exposed to monotonic loading, the stiffness may be obtained from the tangent to the non-linear monotonic load-displacement curve. For high load-levels a gap may open at the rear of the pile. So, when unloading, the foundation is not in contact with the soil, which results in softer behaviour. After a gap formation, the stiffness in the soil is not recovered [31]. Pranjoto and Pender [51] point out that as a rule of thumb, there is a 50% reduction of pile head stiffness after a number of cycles. Further, comparing the hysteresis loops in Figure 2.2 and 2.3, it can be concluded that the hysteretic damping decreases when gapping occurs, since the area under the curve is smaller.

Additionally, Heidari et al. [52] identify that the main cause of cyclic degradation in cohesive soil is a reduction of soil stiffness under cyclic loading (as opposed to strength reduction). Cyclic stiffness degradation may also be observed from Figure 2.3, as the load-displacement curve does not follow the same path for each cycle. The elongation of the hysteresis loop, causes a reduction in tangent stiffness as the amount of cycles increases.

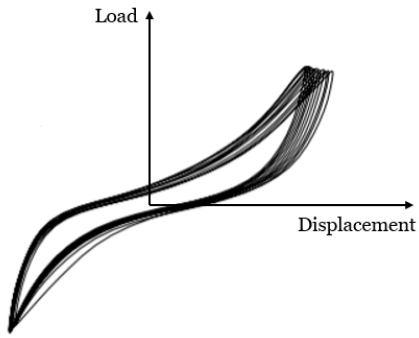

Figure 2.3: Load-displacement curve describing gapping due to cyclic loading on the monopile (adapted from Beuckelaers [31])

DNV-ST-0126 [1] describes that, besides an ULS check, an SLS check is required in foundation design. In the SLS, the accumulated deformations, also known as ratcheting, at the pile head over the lifetime are evaluated. Ratcheting is a result of predominant wind- and wave directions, under low-level long-term cyclic loading [53]. For a monopile exposed to lateral loading a prediction of the accumulated rotations at the pile head is required [1]. In Figure 2.4 the hysteresis loops under long-term cyclic loading are depicted. Two properties of ratcheting of a monopile in low density sand can be deducted from Figure 2.4. First, for

each cycle the area under the hysteresis loop decreases, while the secant stiffness increases. The secant stiffness is defined as the ratio of strength to the maximum displacement and is thus a linear stiffness. Since the area of the hysteresis loop denotes the material damping, this damping decreases under increase rotation accumulation. Secondly, for an increase in load cycles, the rate of accumulation of deformation decreases [53].

Schafhirt et al. [54] investigate the effect of soil properties on the fatigue life and state that accumulated rotation at the pile head has a negligible effect on the accumulated fatigue damage. However, Schafhirt et al. [54] find that changes in stiffness due to cyclic loading, do affect the fatigue damage. This is confirmed by Aassen et al. [36] that indicate that stiffness and especially damping, are considered to have a large influence on the fatigue lifetime.

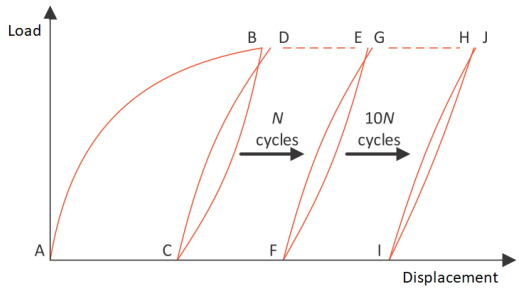

Figure 2.4: Load-displacement curve describing ratcheting as a result of cyclic loading on the monopile in sand (adapted from Houlsby et al. [53])

In earthquake engineering, a field that discusses the dynamic SSI, it is recognised that the frequency content of excitation forces affects the soil response. For monopiles supporting OWTs this interaction can be neglected, since the excitation frequency is generally below 1 Hz, see Figure 2.1 [55, 32, 45]. However, for newly announced OWFs in seismic active areas, like Taiwan, the frequency dependency of the soil response should be considered, since the frequency content from earthquake loading might affect the soil and pile response.

In the project thesis [41], some of the current state-of-the-art foundation models are discussed. However, here only an extraction of the analysis on macro-element models is presented. Further reference is made to Page et al. [42] that give a more elaborate summary of the (limitations of the) existing foundation models.

2.3 Macro-Element Foundation Models

A macro-element model provides the load-deformation relations of an entire foundation at one point, usually at the pile/foundation head, instead of distributing it along the embedded length of the structure. The macro-element model describes the SSI at a single point, and therefore may capture more complicated features as well, by accounting for load-dependent non-linear stiffness and coupling between the different DoF as opposed to Winkler models [45, 56]. Further, Li et al. [56] state that for macroscopic approaches the macro-element model has proven to be relevant for the design of shallow foundations, due to low computational efforts, simple formulations and straightforward numerical implementation.

The advantage of Winkler models over macro-element models is that the forces along the embedded depth of the foundation is given. Especially, since the stress distribution along the embedded depth of the foundation also affects the SSI this can be deemed significant. This limitation of the macro-element model restricts the application of the foundation model. Therefore, it is stressed that macro-element models, and in particular the REDWIN models, may be used in the final stages of the design. For these cases, Skau [45] notes, if the model is sufficiently complex, the SSI can be modelled by a macro-element model with a similar accuracy as a Winkler model.

This section discusses two of the REDWIN model, as well as the impact of the hysteretic behaviour captured by the macro-element model on the foundation design. For the project thesis, other macro-element models where assessed. Appendix A includes a summary of the discussed models.

Macro-Element Models for Integrated Analysis

The macro-element models of Page [32] and Skau [45] are state-of-the-art foundation models for integrated analyses of OWTs exposed to cyclic loading. Page [32] and Skau [45] focus on an improved prediction of non-linear foundation stiffness, hysteretic damping and coupling effects when compared to conventional SSI models, like API [22] $p-y$ curves. Both models do not account for ratcheting, as the accumulated displacements for a 10-minute time series and for fatigue loads are deemed negligible. Please note, the validity of the assumptions of limited cyclic degradation and consequent ratcheting are arguable and require investigation beyond small-scale laboratory tests (e.g. [49, 57]). Although the macro-element models of Page [32] and Skau [45] are both considered suitable for integrated dynamic analyses of OWTs, they differ in in application.

First, the application of the models differs, as the macro-element models are developed for specific foundation types. The former model [32] describes the SSI for monopiles, while the

latter model [45] is developed for shallow skirted foundation. This is reflected in the degrees-of-freedom that the models account for: for monopile foundations it is widely recognised that the axial and lateral loads mobilise a distinct part of the soil along the length of the pile. Hence, the axial and lateral responses are uncoupled. In addition, the axial displacement is modelled to be elastic only. For shallow foundations, on the other hand, the axial and lateral loads are taken by the same soil mass, thus the axial response is coupled with the lateral response in the macro-element model.

Compared to the macro-element models discussed in Appendix A, the input for these models is simple [32, 45]. For shallow skirted foundations, the load reference point, where the horizontal displacements and rotations are decoupled is needed [45]. However, the depth of this point changes with the load level and it is shown that, at least for monopile foundations, keeping the decoupling point constant influences the agreement of the macro-element model and FEA largely [46]. The monotonic soil-monopile behaviour that the foundation models use as an input, may be obtained from 3D FEA or model tests. A more detailed explanation of this is given in Chapter 3.

Lastly, multi-directionality is included in the macro-element model for monopiles and bucket foundations [58]. The effect of multi-directionality in comparison with planar modelling is investigated by Page et al. [39]. Page et al. [39] show that coupling of loading directions has an effect on the load displacement response that is obtained with the macro-element model, as a reduction of stiffness is observed. Thus, the applicability of macro-element models developed for planar loads is questioned. Especially, since a correct representation of stiffness is essential for optimisation of OWT foundation design.

Both models are verified with FEA as well as validated with field data [40, 33]. The monopile macro-element model is verified with overall response and the unload-reload loop that is performed in the PISA field test on Cowden clay. The results of one of these validations is included in Figure 2.5. It can be seen that the general behaviour is well captured by the macro-element model. Also, the hysteretic behaviour of the unload-reload loop is modelled accurately, with the area under the hysteresis loop being approximately equal. However, the stiffness upon reloading is slightly overestimated [40]. As the initial unloading and reloading stiffness should have the same value, it is considered that this discrepancy may be due to problems in the field test.

The multi-directional macro-element model as Page et al. [39] present, is thus far not validated with field tests, as the required data is not available. Instead, the model is verified against 3D FEA, which makes use of a newly developed constitutive model that is verified using a cyclic triaxial test. As both the macro-element model and the constitutive model are based on multi-surface plasticity it is consistent that a comparison gives a good agreement.

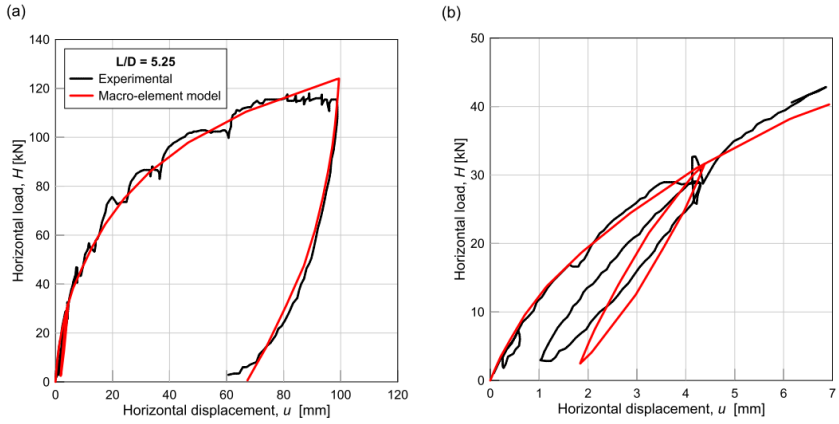

Figure 2.5: Macro-element model response compared to the PISA field test in Cowden clay with pile L/D = 5.25 [40]

Further, even though both macro-element models are formulated as a total stress model and are hence developed for cohesive soils, Skau [45] states that the macro-element model may also be applied in integrated analysis for sand-dominated soils. Also, the analogous model of Page [32] is partially verified for applications in non-cohesive soils. However, it is suggested that an effective stress based model may be required, when the generalised effective stress level changes significantly with the load level [45]. In effective stress analyses, the stiffness of the sand is largely defined by the vertical effective stress, so a change in σ'_v may alter the soil-structure interaction. For OWTs with a monopile foundation, the vertical load is can be assumed to be constant. Hence, for practical purposes the macro-element model may be applied in non-cohesive soils.

Impact of Macro-Element Models on Foundation Design

The effect of the macro-element model on the fatigue life damage for a monopile-based OWT exposed to cyclic loading is studied by Aassen et al. [36] and Page et al. [37]. In order to evaluate the fatigue damage along the embedded length of the pile, Næss [59] and Page [32] present a post-processing tool. This tool uses the loads at seabed found with the macro-element model to determine the bending moment along the monopile. The bending moment distribution is determined with a 1D model that applies the p-y principle. Even though the p-y formulation is deemed conservative, it is concluded that the fatigue damage

found with the macro-element model + post-processing tool is significantly less than found with a *p-y* analysis only [32]. The effect of capturing the non-linear stiffness and damping is found to decrease the fatigue damage by 11-22% when compared to alternative foundation models as used in the industry. Moreover, these studies place the emphasis on idling cases, where aerodynamic damping is absent and thus results in a high contribution to the fatigue damage. This effect is amplified due to the high probability of occurrence for these load cases [36]. In idling cases, the main source of damping is soil damping, which is captured by the macro-element model, so a careful prediction of the damping is required.

For fatigue load calculations, the load levels are small, and thus the effect of accounting for the unloading-reloading stiffness is smaller than for high-load cases, like the ULS. In ULS conditions, however, the macro-element model model formulation might give an overestimation of the damping, due to Masing behaviour.

The next section elaborates on the formulation of the macro-element model that is presented by Page et al. [39]. In the project thesis [41] a comprehensive overview is given of the formulation frameworks and the effects of the modelling decisions on the macro-element model response. As the model of Page et al. [39] is based on multi-surface plasticity theory within the elasto-plasticity framework, only this theories are outlined here.

2.4 Macro-Element Model Formulations

The formulation of macro-element models developed by the geotechnical engineering community, is based on similar formulations as soil constitutive models. Constitutive models describe the stress-strain relation of, for instance, soil, instead of the load-displacement relation, as is done in macro-element models. Since the development of thee first macro-element model [34], a variety of macro-element models is developed. For some of these models, their properties, limitations and formulation framework are compared and included in Appendix A.

This section discusses the elasto-plastic formulations as included in the REDWIN models, with special focus on the contributions of the elastic and plastic displacements that are obtained in the macro-element model.

Principle of Elasto-Plasticity

Figure 2.6 shows the rheological scheme for an elastic-perfectly plastic model. Here, H denotes the force, K the stiffness of the elastic spring, H^* the slipping force of the slider and α is the memory of the slider. In case the spring is loaded with $H < H^*$, the slider is

not activated. Thus, all displacements are elastic, which implies that they are recoverable. For loads $H > H^*$, besides the spring the slider is also activated. This results in additional displacements, when compared to the $H < H^*$ case. The displacements generated by the slider are plastic and thus irrecoverable.

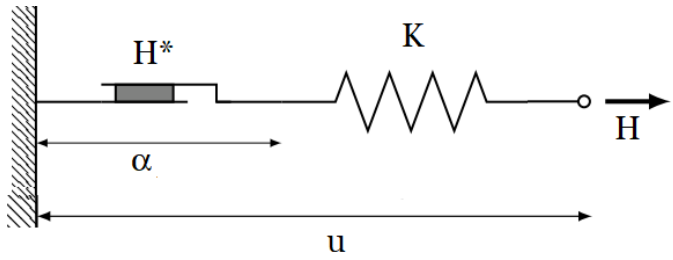

Figure 2.6: Rheological scheme of elastic-perfectly plastic model (adapted from Beuckelaers [31])

From the spring-slider analogy, it is easily seen that the total displacement is the sum of the elastic and plastic displacements, as shown in Equation 2.1. This decomposition of strains is the basis for the theory of elasto-plasticity.

$$v_i = v_i^e + v_i^p \tag{2.1}$$

With v the displacement vector, consisting of translational (u) and rotational (θ) displacements. To obtain the total displacement, the distinction between elastic and plastic behaviour is made. This section first evaluates the elasticity formulations as included in the macro-element model for monopile foundations [39]. Next, the framework that this model uses for determining the incremental plasticity is outlined. The section on multi-surface plasticity discusses the yield criterion, flow rule, hardening rule and consistency condition that are used in the macro-element model. For more information regarding the numerical implementation of multi-surface elasto-plastic models, reference is made to Grimstad and Benz [60], Page et al. [40, 39] and Skau et al. [33].

In two circumstances, the soil responds elastically to a load, 1) for very low load levels and 2) for the first part of unloading and reloading. Equation 2.2 yields the elastic (generalised) displacement, from the elastic stiffness, K^e and the (generalised) load, t. In a N degree-of-freedom (NDoF) system, the elastic stiffness is a matrix, while the displacement and load are first-order tensors.

$$t = \boldsymbol{K}^e \, v^e \tag{2.2}$$

Either the load, t, or the elastic displacement, v^e, vector is known, so the elastic stiffness, $\boldsymbol{K}^e$, is required. In macro-element modelling the stiffness coefficients are generally obtained from FEA [32, 45].

Multi-Surface Plasticity

Besides an elastic formulation, a plastic formulation is required. Both Byrne and Houlsby [8] and Houlsby et al. [61] stress the potential of multi-surface plasticity in macro-element models for cyclic behaviour of foundations. Mostly, because multi-surface plasticity allows for a change in stiffness upon load reversal. Multi-surface plasticity is compatible with the incremental plasticity theory as is outlined in, for instance, Nordal [62]. The main difference is that instead of one yield surface, multiple yield surfaces are used to describe the soil behaviour. The origin of multi-surface plasticity lies in Iwan [63] and Mróz [64], that describe multiple yield surfaces to account for kinematic and a combination of kinematic and isotropic hardening, respectively. As both the models of Page [32] and Skau [45] are based on 'pure kinematic hardening multi-surface plasticity', this is, hereafter, indicated as a 'multi-surface plasticity' model.

Figure 2.7 shows an example of multi-surface plasticity. The soil responds elastic for loads within the first yield surface. If the yield function for the first surface is larger than zero (i.e. the criterion of the first yield surface is violated), plastic deformations develop, which cause the first yield surface to move in load space. This process is continued and while loading, more yield surfaces are violated. As a result, the response becomes less stiff, which may be observed from the load path A-B. Upon load-reversal, first elastic behaviour is observed, until the yield surface is violated on the other side, load path B-C, for instance. As stated by, e.g. Byrne and Houlsby [8], multi-surface plasticity correctly simulates Masing behaviour for low to moderate strains, by taking into account elastic response under load reversal and including memory of the stress state.

First, this section outlines the rheological schemes that are developed to describe multi-surface plasticity. Next, the section elaborates on the modelling ingredients for multi-surface plasticity: the yield criterion, flow rule, hardening rule and consistency condition.

Rheological Scheme

Iwan [63] represents multi-surface plasticity as coupled spring and slider elements, to obtain a multi-linear relation between stress and strain (load and displacement). The springs and sliders may be modelled in a parallel-series formation, as in Figure 2.8, or a series-parallel formation, as in Figure 2.9. To prevent any ambiguity, the parallel-series and the series-

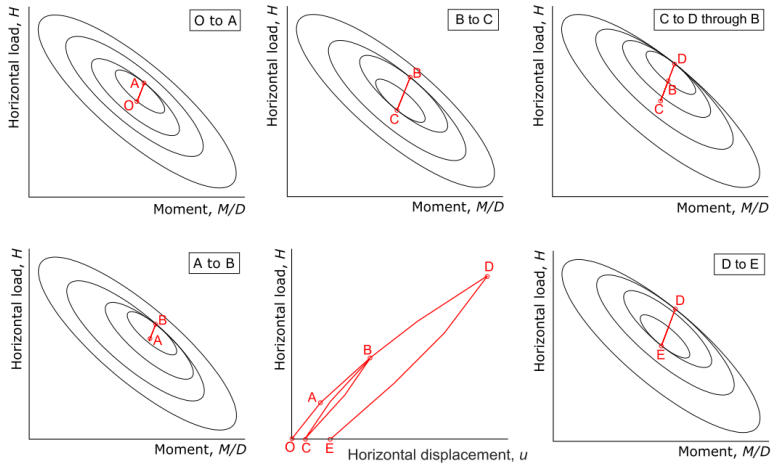

Figure 2.7: Example of multi-surface plasticity [40]

parallel model will from now on be denoted as the parallel-coupled and the series-coupled model, respectively.

As can be seen in Figures 2.8 and 2.9, the models consist of springs and sliders. The springs have stiffness K and the sliders slip when the force, H, is equal to the slipping force, H^*. The sliders have a memory, α, that remembers the developed plastic displacement. In the parallel-coupled model, the displacement, u, is equal for each spring-slider combination, which results in a summation of elastic (spring) and plastic (slider) contributions to the force. In the series-coupled model, on the other hand, the sum of the displacement of each spring-slider combination gives the total displacement. If the yield stress of a slider is reached, the 'plastic' spring, e.g. H_1 in Figure 2.9, is activated and plastic displacements develop [63].

Iwan [63] states that the latter model is more applicable within the theory of elasto-plasticity as both the theory and the model are based on the decomposition of elastic and plastic strains. However, this does not imply that the parallel-coupled model cannot be used within elasto-plastic models. First, Grimstad et al. [65] use both models to couple multiple NGI-ADP constitutive models and conclude that the behaviour of both coupling models is very similar, albeit the series-coupled model behaves somewhat stiffer. As the series-coupled model is computationally slower than the parallel-coupled model, Grimstad et al. [65] favour the latter model, if no other benefits are obtained from using the series-coupled model. Furthermore, it is considered that the implementation of the parallel-coupled model is more

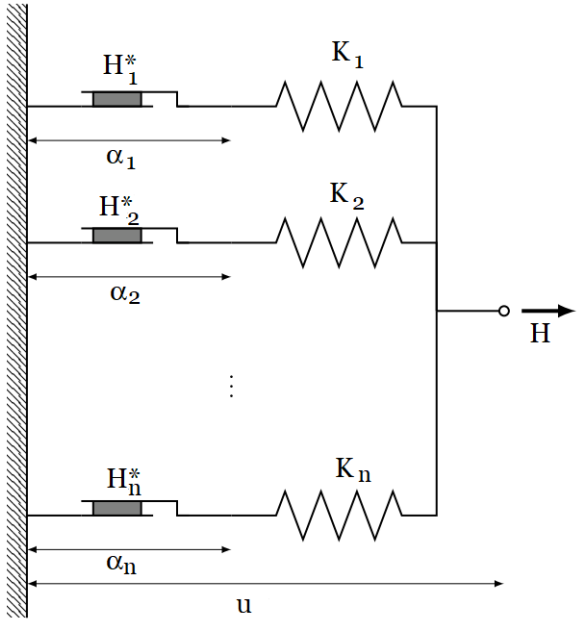

Figure 2.8: Rheological scheme of the parallel-coupled model to describe multi-surface plasticity (adapted from Beuckelaers [31])

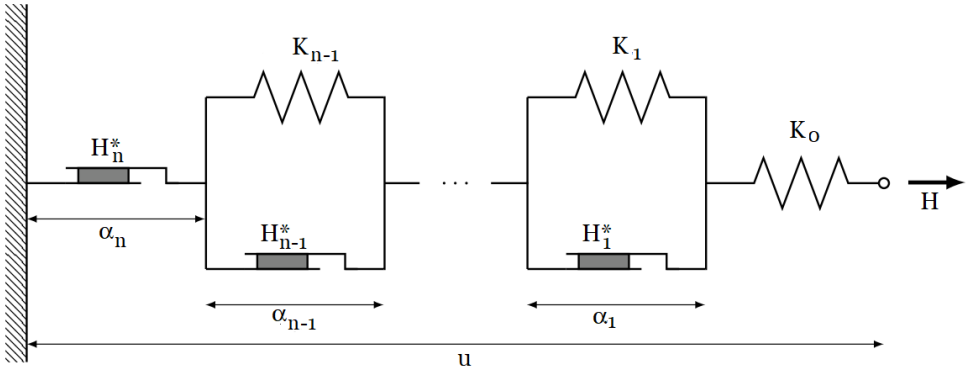

Figure 2.9: Rheological scheme of the series-coupled model to describe multi-surface plasticity (adapted from Beuckelaers [31])

straightforward.

However, Skau [45] finds that the macro-element model based on the parallel-coupled model is not suitable for dynamic integrated analyses of OWTs. The results, when a macro-element model is exposed to radial load paths in the H, M plane, show a fair agreement with FEA. Though, for more general load histories, that include cyclic loading and a random ratio between H and M, the loads in the submodels of the parallel-coupled model are irregular. As the plastic deformation of each submodel depends on the experienced load state, the inconsistent distribution of the load is unfavourable. Hence, the use of the series-coupled model is advised and implemented in the multi-directional macro-element model [39].

Yield Criterion

Iwan [63] develops the multi-surface plasticity model in all three dimensions with a Von Mises yield criterion, to model the stress-strain behaviour of materials. A more extended yield criterion, that is applied in macro-element modelling, originates from Mróz [64]. Here, surfaces with equal work hardening moduli are defined as the yield and loading surfaces. However, from Mróz [64] it is inconclusive what is meant by work hardening moduli. Therefore, Page [32] and Skau [45] interpret the work hardening moduli as contours of plastic work. So, the yield surfaces result from a least-squares fit on plastic work ellipses that are obtained from FEA. In the developed macro-element model for monopiles the yield surfaces are homothetic to each other, so there is no change in shape, only in size [40, 39]. Please note, the homothetic yield surfaces are an approximation of the retrieved contours of plastic work and thus impose a limitation to the application range of the model.

In order to present a robust model, Page et al. [40, 39] transform the yield surfaces from ellipses to circles and spheres, respectively. Hence, a single load invariant defines the shape of the yield surface. Note, though, this transformation is solely possible, when the yield surfaces are homothetic [40]. So, in the macro-element model of Skau et al. [33], no transformation is included, as the yield surfaces are not defined to be homothetic.

Flow Rule

Page [32] and Skau [45] show that the direction of the plastic work vectors, that describe the direction of the development of the plastic work, is perpendicular to contours of plastic work. Thus, an associated flow rule is considered appropriate.

Hardening Rule

As the macro-element model is a purely kinematic hardening model, the hardening rule describes the direction in which the yield surfaces are translated, which depends on the translation rule. The translation rule defines the direction of the centres of the active yield surfaces. The backstress, α_i, is the centre of the yield surface, so after a displacement increment is applied, the centre of all surfaces is updated [32]. The next paragraphs discuss frequently used translation rules for kinematic hardening soil models.

Page [32] applies the Prager [66] and Ziegler [67] kinematic hardening translation rule, as the kinematic hardening rules coincide. The kinematic hardening rule that is proposed by Mróz [64] is disregarded, since this translation rule results in numerical ratcheting in multiaxial conditions [68, 45]. Further, Montáns and Caminero [68] show that the Mróz translation rule depends on the number of load surfaces, while the Prager criterion does not [68]. It is considered that this dependency is a limitation of the former kinematic hardening rule.

The difference between the Prager and Ziegler criterion is that the direction of translation of the yield surface for the Prager criterion is in the direction normal to the yield surface and proportional to the plastic displacement (for associated flow) [66]. The Ziegler translation rule states that the yield surface translates in the direction of a vector $\boldsymbol{t} - \alpha$. Ziegler [67] mentions that the Prager and Ziegler criterion may coincide, depending on the shape of the yield surface. In the macro-element models of Page [32] and Skau [45] the kinematic hardening rule of Grimstad et al. [65] is used, that obeys to the Ziegler transformation rule.

For both the Prager and Ziegler transformation rule, other surfaces are not accounted for in the formulation. Therefore, it is possible for the surfaces to intersect. The non-intersection condition is first introduced by Mróz [64], however later Puzrin and Houlsby [69] suggest that the non-intersection condition is not a requirement.

Consistency Condition

In multi-surface plasticity the consistency condition defines the magnitude of the scalar $d\lambda_i$ for each yield surface [33]. Skau et al. [33] show how the multi-linear relation for $d\lambda_i$ is determined from single-surface plasticity formulations and thus comply with the proclamation of Puzrin and Houlsby [70].

In multi-surface plasticity, the movement of multiple surfaces in the load space may yield to plastic displacements. The Koiter rule [71] as included by Page [40] and Skau [33] states that the total plastic displacement is the sum of the plastic displacement generated by the active

yield surfaces. This is analogous to to the series-coupled model, where plastic displacements are generated by activated sliders only.

2.5 Summary

In this chapter, the literature review of the project thesis is summarised. Three aspects are highlighted: 1) design of monopile foundations and 2) the effect of macro-element models in design and 3) the formulations as included in the REDWIN models.

For monopile foundations, the impact of cyclic loading is not yet accounted for correctly in design, as the current design practice is based on nonlinear elastic semi-empirical curves. In reality, Masing behaviour is observed, especially for low-load levels. For ULS analyses, gapping, ratcheting and cyclic stiffness degradation may become critical in 10-minute time domain analyses.

Multi-directional macro-element models for monopile-based OWTs may be used in integrated analyses. Even though the response along the embedded depth is not captured, it is shown that implementing the macro-element model in integrated analyses, gives a more accurate fatigue damage prediction. Moreover, the natural frequency may be estimated with a higher accuracy.

The REDWIN macro-element models are formulated within the framework of elasto-plasticity. Here, a distinction is made between elastic, reversible, and plastic, irreversible, displacements. The plastic displacements are obtained from multi-surface pure kinematic hardening plasticity theory. It is demonstrated that including these formulations in the macro-element model, results in Masing behaviour and hysteretic damping.

Chapter 3

Numerical Analyses

3.1 Introduction

The multi-directional macro-element foundation model of Page et al. [39] is thus far predominantly verified for application in the fatigue limit state. As the objective of this research is the application of the macro-element model in the ultimate limit state, the use of the model requires additional verification. The verification strategy follows Page et al. [39], that compare the predictions of the response from the macro-element model to results from three-dimensional finite element analyses.

The chapter firstly discusses the finite element model set-up, including the choice for the constitutive models and soil parameters. In addition, the chapter outlines the calibration of the constitutive model and the macro-element model against FEA. Lastly, the results for the response of the macro-element model to load levels for an OWT or exposed to extreme load levels are given and compared to the response of a 3D finite element model. The verification analyses use a variety of geotechnical and loading scenarios to identify potential model limitations in ultimate limit state conditions.

3.2 Model Set-Up

The basis of the verification analysis of the macro-element model response for high load levels is by finite element analyses. The commercial software *PLAXIS 3D* [72] is used in the three-dimensional analyses. The calibration of the macro-element model is also based on

FEA. Figure 3.1 gives an overview of the executed analyses. For the comparative part of the study, the MATLAB environment is used, Appendix B outlines the macro-element model (as a *.dll*) implementation strategy.

The comparative FEA use the user-defined soil constitutive model *VonMisesSeriesCoupled*, that Page et al. [39] developed. To calibrate the user-defined soil model *VonMisesSeriesCoupled* (UDSM), a commercially available constitutive model (*Hardening Soil Small Strain*) is used that accounts for non-linear elasto-plastic soil behaviour. This section outlines the choice of this constitutive model as well as it discusses the soil parameter selection for the calibration procedure, the 3D finite element model set-up and finally the calibration of the UDSM and the macro-element model.

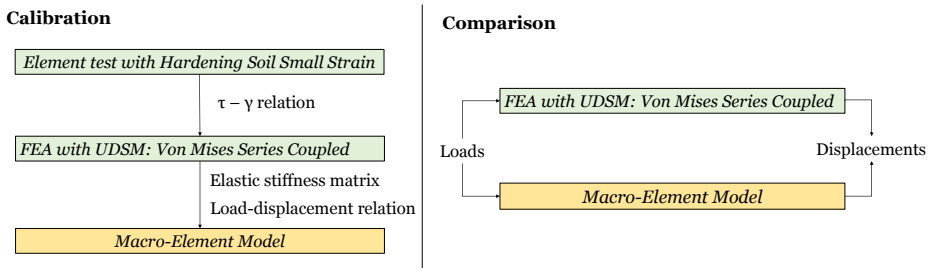

Figure 3.1: Overview of the (constitutive) models used in the comparative analysis. Green models are constitutive models used in PLAXIS [72] and yellow represents the model used in MATLAB [73].

3D Finite Element Model

In *Plaxis 3D*, two models are created: 1) a reduced finite element model, which includes only half of the FE model and relies on symmetry conditions and 2) a full FE model. The reduced model is employed for calibrating the macro-element model, since the applied loading and geometry is symmetric. For the comparative study, the loading is not symmetric and thus requires the use of the full FE model. As the model set-up is similar for the reduced and the full model, there is merely elaborated on the model set-up of the reduced model.

In accordance with Page et al. [40], the soil continuum in the boundary value problem is $24D$ wide and $10D$ deep, as Figure 3.2 shows. These dimensions are chosen such that the boundaries of the model do not influence the response of the monopile to the load. The soil is modelled as fully saturated, with the hydraulic head kept at 1m above the soil. Further, the model includes the monopile as a volume pile, of which the stiffness and strength properties

are set in a linear elastic non-porous soil constitutive model. Please note, the pile geometry is determined from a design analyses that use API p-y curves for modelling of the SSI. Thus, giving relatively stiff soil-monopile behaviour.

By accounting for the same bending stiffness, EI, the equivalent stiffness of the volume pile is determined with Equation 3.1.

$$E_{mp}\, I_{mp} = E_{vp}\, I_{vp} \tag{3.1}$$

With the subscripts mp and vp denoting 'monopile' and 'volume pile', respectively. To apply forces and moments to the monopile, the top of the monopile is closed and modelled as a rigid body, that is located at the centre of the pile head, this allows for a more even distribution of the stresses in the pile [74]. As the rigid body is solely located at the top of the volume pile, the rest of the volume pile shows more flexible behaviour. In addition, the expected behaviour of the monopile is checked with Equations from Higgins et al. [75]. It is found that the equivalent pile stiffness, E_{vp}, is below the rigid threshold and hence, the behaviour of the monopile is not pure rigid, nor purely flexible.

The monopile is *wished-in-place*, so the model does not account for installation effects. In the phase following the activation of the pile, the displacements are set to zero. In addition, the soil-structure interaction is modelled with an outer interface around the monopile. This interface is slightly extended beyond the length of the monopile, to prevent numerical issues [72]. Further, an interface is included at the base of the monopile. All interfaces have the same stiffness parameters as the adjacent soil. In addition, for all but the extended interface, the strength is reduced to $2/3$ of the soil strength next to the pile.

For verification purposes, two 'sanity checks' are executed that assess if the finite element model is set-up correctly. The first compares the displacement at seabed from Plaxis with the results of the Timoshenko shear beam equations. The shear coefficient, κ, results from Equations of Hutchinson [76] for a tubular beam. Plaxis models the soil below L_{mp} as very stiff (E $\approx 10^{15}$ kPa), while the soil above L_{mp} is very soft (E $\approx 10^{-3}$ kPa). To imitate the pile being clamped, the volume pile extends into the very stiff soil. The response u_x to a unit load at the pile head from Plaxis compares very well to the estimate from the Timoshenko clamped beam equation ($\epsilon < 1.5$ %). In addition, the pile deflection at seabed of Plaxis are compared with estimates of Higgins et al. [75] for rigid and flexible piles. As expected the displacements from the finite element model are in between the predicted displacement at seabed for a rigid (lower) and flexible pile (higher), when exposed to the same load.

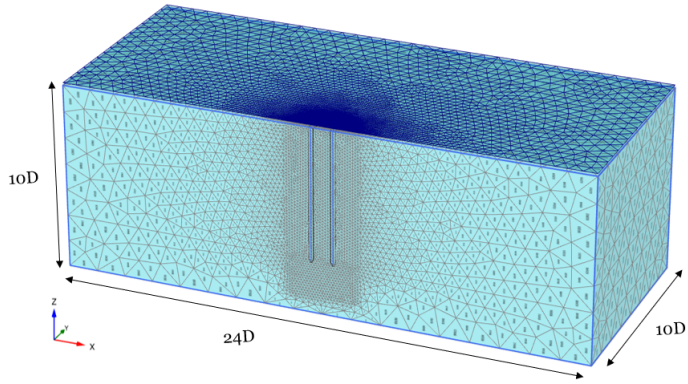

Figure 3.2: Reduced 3D finite element model and mesh distribution

Constitutive Model Selection

In order to assess the effect of going from a 3D soil-pile continuum to a force-displacement relation, the constitutive relations in the 3D continuum and the analyses employed to calibrate the macro-element model should be equivalent. Figure 3.1 highlights the application of two constitutive models in the comparative analyses. First, the *Hardening Soil Small Strain* (HSsmall) model is able to describe non-linear elasto-plastic soil behaviour. This model gives the input to calibrate the macro-element model and the constitutive model of Page et al. [39], that are used in the comparative analyses. The HSsmall model is preferred as the model allows for a more accurate prediction of displacements than the *Hardening Soil* constitutive model. Further, as there is not much soil data available for the selected site, it is required that the input parameters may be derived from cone penetration tests (CPTs) only. Two of the properties of the HSsmall model are important to highlight: 1) the stiffness parameters (E_{oed}, E_{50}, E_{ur}) are dependent on the effective stress and 2) the additional HSsmall parameters (G_0^{ref} and $\gamma_{0.7}$) account for very small strain stiffness decay [72]. Due to the different constitutive relations in the HSsmall model and the macro-element model, the HSsmall may not directly be used for the comparative study.

Instead, the comparative analyses use the UDSM *Von Mises Series Coupled* as constitutive model [39]. Unlike the HSsmall model, the model formulation is based on multi-surface plasticity with kinematic hardening, similar to the macro-element model. This allows for a comparison of the response that solely assesses the effect of going from a three-dimensional soil continuum analysis to a macro-element formulation.

Please note, the HSsmall model is an effective stress model, while the UDSM is a total stress model. In an effective stress model, the size of the yield surface increases with effective mean stress (e.g. Drucker-Prager), whereas the yield surface of a total stress model keeps the same size (e.g. Von Mises). Moreover, the HSsmall model accounts for (effective) stress-dependent stiffness, while the UDSM uses the same stiffness, regardless of vertical stress level. These discrepancies between the models are accounted for in the following way: 1) the analyses are executed undrained and 2) the soil stiffness properties in the UDSM are dependent on s_u, which can be modified with depth. The FEA may be performed undrained, as only 1-2 cycles are compared [77]. So, during the FEA with HSsmall model the effective stresses do not change and the stiffness is merely depth (pressure) dependent. In the UDSM the stiffness parameters are normalised by s_u that increase linearly with depth, so the stiffness parameters increase correspondingly. However, for the HSsmall model the stiffness does not increase linearly with depth, but rather follows a polynomial of which the shape is determined by the factor m (= 0.5) [78]. This is taken into account in the calibration of the UDSM model (Section 3.2).

Soil Parameters

Tor simplicity and computational efficiency of the FEA, the first calculations are performed for a monopile in a single layer normally consolidated homogeneous soil. The soil properties are chosen to, on average, represent the strength and stiffness of the whole soil continuum of the selected OWF (Chapter 4). For the homogeneous soil layer, the strength is given by the undrained shear strength, s_u that varies linearly with depth (e.g. [79]). The soil stiffness follows a polynomial profile, as prescribed by the HSsmall model. The magnitude of the stiffness at reference pressure is deduced from CPT data. The dilatancy angle is set to zero, for numerical reasons.

User Defined Soil Model Calibration

The input for the UDSM *VonMisesSeriesCoupled* is described by Page et al. [39]. Besides numerical parameters, the model uses the plastic stiffness (G^p), Poisson's ratio (ν) and s_u per yield surface as an input. As there are no laboratory test results available for the soil data of the selected site, the required input parameters are obtained from stress-strain curves generated with the HSsmall constitutive model, which are derived from CPT correlations. This calibration is performed in the 'Soil Test' program of PLAXIS 3D. First, Direct Simple Shear (DSS) tests are executed on the HSsmall soil. The DSS determines the shear stress - shear strain (τ-γ) relation as well as s_u at five locations along the z-axis of the soil continuum. The difference in depth is accounted for by changing the vertical effective stress

(σ'_v). Accounting for normally consolidated soil, the vertical preconsolidation stress is set equally to the vertical effective stress.

From the τ - γ curves, the size of the yield surface and the stiffness of the soil upon activation of the yield surface are defined. In the UDSM the yield surfaces are series-coupled, which is in accordance with the formulation of the macro-element model. The first estimation of these properties is done using a MATLAB script from Page (private communication). In order to obtain an appropriate distribution of the yield surfaces, the distribution between the points is increased as the shear strain increases. Hence, more data points are used in the non-linear part of the curve, so the non-linear behaviour of the soil may be approximated better. To confirm that the established soil properties fit well, the 'Soil Test' function in PLAXIS is used again, but this time with the UDSM. In order to calibrate the *VonMisesSeriesCoupled* model correctly, the spring stiffness may be adjusted, so a good fit is obtained between the τ - γ curves resulting from HSsmall and UDSM model. Figure 3.3 shows the τ-γ response predicted by the HSsmall and UDSM VonMisesSeriesCoupled for one layer. It is seen that these are in good agreement. The points in the curve where the stiffness changes, is the location where a new yield surface is activated.

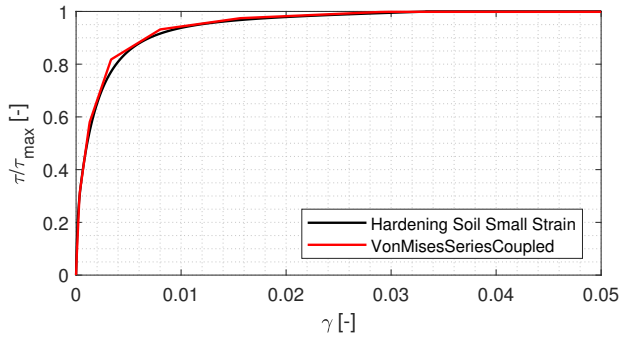

Figure 3.3: Comparison of normalised τ-γ response for HSsmall and UDSM calibrated to properties of Layer 2

In addition, Figure 3.4 shows the normalised properties of the UDSM. The left figure includes the shear stiffness decrease with increasing shear strain. The right figure presents the distribution of yield surfaces. The most inner surface is very small, as the small-strain stiffness may only be included for very small strains (e.g. strain $\leq 1\ 10^{-6}$)[78, 80].

The UDSM is calibrated for five τ - γ curves, that are extracted for increasing vertical effective stresses. The purpose is to simulate the stress-dependency of the stiffness in the UDSM. By fitting different properties to the τ - γ curves, a more accurate representation

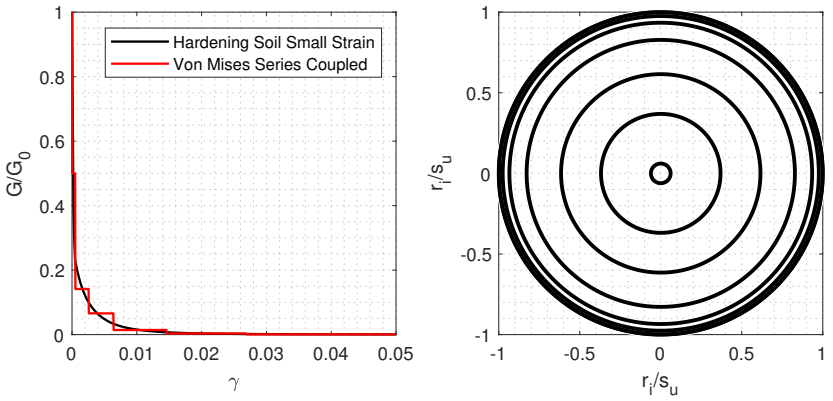

Figure 3.4: User-defined soil model input: normalised spring properties for Layer 2. Left: shear stiffness decay with increasing shear strain. Right: distribution of Von Mises yield surfaces

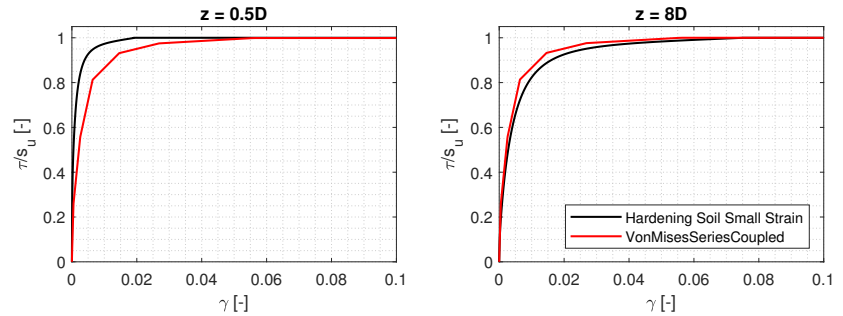

Figure 3.5: Comparison of Soil Test τ-γ results for varying vertical effective stress for HSsmall and UDSM that is calibrated to properties of Layer 2

of the soil stiffness may be obtained. Especially in the top layer of the soil, up to $3D$, a more specific distinction in soil stiffness is made (Table 3.1). The increased precision in discretisation is required, due to the larger influence of the top layer soil stiffness on the response at seabed [81]. Figure 3.5 highlights the importance of accounting for multiple soil layers in the calibration. This plot shows two curves: the first (black) is the τ-γ response according to the HSsmall model. The second (red) curve shows the τ-γ curve predicted by the UDSM that is calibrated to the properties of Layer 2. It is observed that the UDSM gives

a softer response than the HSsmall model, in the soil above Layer 2 (z = 0.5 D m). Further, the predicted reaction is too stiff for the soil below the calibration point.

Table 3.1: Layer discretisation and calibration points for UDSM *VonMisesSeriesCoupled*

	Layer 1	Layer 2	Layer 3	Layer 4	Layer 5
z_{range} [m]	0 - D	D - 2D	2D - 3D	3D - 6D	6D - 10D
$z_{calibration}$ [m]	0.5 D	1.5 D	2.5 D	4.5 D	8 D

Figure 3.6 predicts the resulting soil properties over depth. It may be observed that there is sufficient agreement with the stiffness profile of the HSsmall model. The stiffness fit may be improved by changing the undrained shear strength profile, as the stiffness at depth is calculated from G_{max}/s_u.

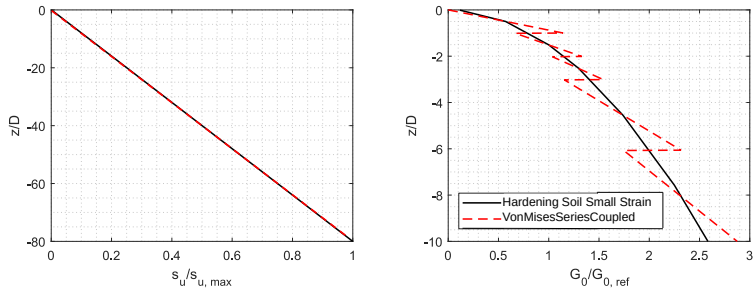

Figure 3.6: Input strength and parameters from the *Hardening Soil Small Strain* constitutive model as included in the user defined soil model *VonMisesSeriesCoupled*.

Macro-Element Model Calibration

The macro-element model requires two types of input, 1) the elastic stiffness properties (*Propsfile*) and 2) non-linear load-displacement curves at pile head (*Ldispfile*) [39, 58]. To obtain the input data, two pushover finite element analyses are performed, one where $H \neq 0$ and $M = 0$ and vice versa. For this case, the load range of the pushover analyses is from 0 kN to 30 10^3 kN and 0 kNm to 800 10^3 kNm, for H and M loading, respectively.

The pushover is done in a PLAXIS model with the *VonMisesSeriesCoupled* UDSM, that is calibrated to the HSsmall model, as outlined in Figure 3.1. For the comparative analysis, the macro-element model is calibrated to a full 3D model in PLAXIS. This is done as the primary purpose is capturing the 3D response with the macro-element model. For calibration of the macro-element model for design purposes, it suffices to use the reduced model. In addition to calibration with FEA, the macro-element model may be calibrated with results from field tests or centrifuge tests.

First, to obtain the elastic stiffness matrix, the initial stiffness is determined from the resulting non-linear load-displacement curves. The first data points of the non-linear load-displacement curves at seabed, where the soil behaves elastic yield the coefficients of the flexibility matrix. Inverting this flexibility matrix gives the elastic stiffness matrix. As expected, the coupling terms have (approximately) the same magnitude. To calibrate the macro-element model, the monopile is loaded to high load levels. Hence, in the 3D model, a gap may open in the pushover analysis. Please note, the geometrical consequences (e.g. stiffness decrease due to gapping) are included in the calibration curve.

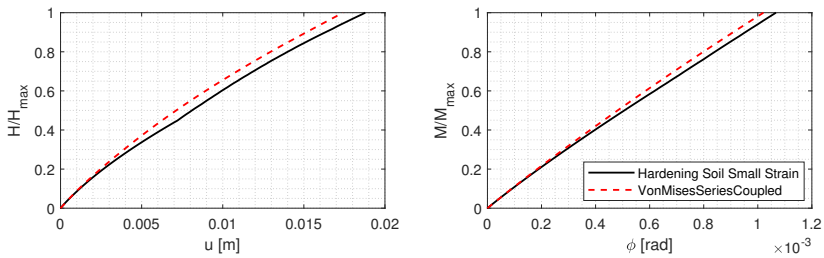

Figure 3.7: Comparison of normalised input curves from 3D finite element analyses with *Hardening Soil Small Strain* and *VonMisesSeriesCoupled* model. For brevity, the $H - \phi$ and $M - u$ curves are omitted.

Figure 3.7 shows the calibration curve obtained with the HSsmall constitutive model in a reduced 3D soil continuum, as well as the calibration curves obtained with the UDSM in a full soil continuum. The UDSM is able to capture the behaviour of the single layer HSsmall soil continuum with sufficient accuracy. Especially, as the comparative analyses is purely based on the UDSM results, an exact agreement is not required (Figure 3.1).

3.3 Macro-Element Model and FEA Response

This section compares the estimated displacements of the macro-element model to the results of the FEA. To identify possible limitations in the macro-element model, the study evaluates a variety of geotechnical and loading conditions. As the REDWIN macro-element model is a cyclic model, the FEA and macro-element model apply the loads without any time-dependence. The loads may be applied statically as the soil stiffness is not frequency dependent for the excitation frequencies of an offshore wind turbine [55].

Monotonic Finite Element Analyses

Besides cyclic FEA, of which the results are presented in the next section, a monotonic analysis is performed, using the HSsmall model for calibration. The purpose of the analyses is 1) to verify that the macro-element model captures the calibration curve correctly and 2) to investigate for which load levels the monotonic curve of the macro-element starts deviating from the calibration curve. Please note, this is dependent on the input soil parameters.

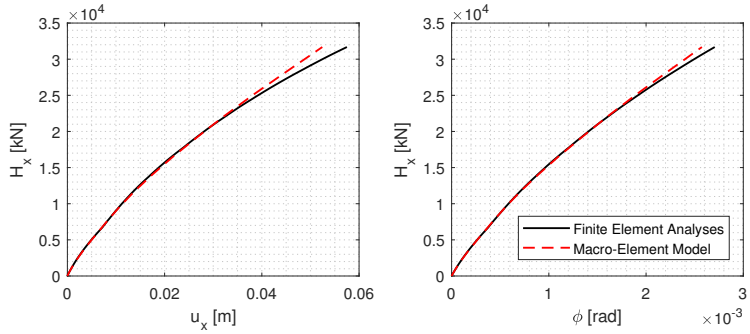

Figure 3.8: 3D FEA and macro-element model response to a monotonic load ($N = 25$ surfaces) in a HSsmall 3D reduced soil continuum

Figure 3.8 shows the calibration curve for 3D FEA with $H \neq 0$ and $M = 0$. Up to approximately 25 MN, there is a very good agreement with the predicted response of the macro-element model and 3D FEA. For larger loads, the predicted response from the macro-element model starts to deviate from the 3D FEA results. However, the ULS base shear at the selected site is much lower than the H for which the two curves start to differ. Hence, also cyclic finite element analyses are performed, to investigate the response in cyclic loading.

Cyclic Finite Element Analyses

The aim of the multi-directional macro-element model is application in integrated analyses, where the OWT is exposed to cyclic loading. Hence, the ability of the macro-element model to capture the force-displacement response upon cyclic loading is essential. Therefore, Page et al. [39] verify the multi-directional macro-element model with cyclic FEA for ULS load cases with loads up to $H = 12$ MN and $M = 300$ MNm. As the design loads at the selected site are larger than the loads included in Page et al. [39], an additional verification is required. The load time series as used in this thesis result from BHawC, the SGRE tool for load calculation (Armstrong, private communication). Due to confidentiality, all loads in this thesis are normalised to H_x and M_y. Note, Appendix C includes some additional results of the cyclic 3D FEA that are performed for this thesis.

Further note that due to limitations of the initial UDSM formulation, the solution strategy is updated in the last version of the UDSM. The new solution strategy uses a binary solution method, that includes a computational efficient algorithm that allows for non-successive yield surfaces to be active. This increases the robustness of the constitutive model. In case the first solution does not converge within the desired number of iterations, substepping is called. If the substepping does not provide a solution, the analysis is performed uncoupled. Because of the uncoupled analysis, the plastic multiplier, $d\lambda$, may be overestimated, which may cause some numerical ratcheting (Grimstad, private communication).

Planar Two-Way Symmetric Cyclic Loading

Initially, the performance of the macro-element model under ULS load levels is checked with two-way symmetric cyclic tests to planar loading conditions at mudline. This demonstrates the characteristic hysteretic behaviour. Figure 3.9 shows the normalised 3D FEA and macro-element model response at mudline in the load-displacement plane, for extreme H-M loads. The base shear and moment at mudline used for this analysis are roughly 1.5 as high as the extreme loads that Page et al. [39] apply for the verification analysis. The finite element model applies the loads without any time dependence at mudline, as the macro-element model is frequency independent. Further, the H/M-ratio remains constant during the analysis.

Generally, the response from 3D FEA and the macro-element model agrees well to the extreme load cycle, as Figure 3.9 depicts. For the predominant part the response of the macro-element model follows the backbone curve from 3D FEA very well. However, while approaching the maximum base shear and moment, the macro-element model predicts a too soft response, when compared to the 3D FEA results. Please note, this behaviour is more apparent in the left plot (base shear - translation). The slight overestimation of the predicted displacements from the macro-element model, results in a small overestimation of

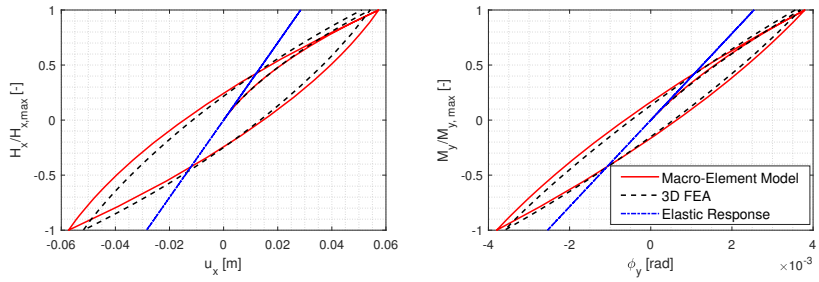

Figure 3.9: Normalised macro-element and 3D FEA response to extreme planar two-way symmetric cyclic load for constant H/M ratio. Elastic response illustrates development of plastic strains.

the enclosed area of the hysteresis loop. Page (private communication) postulates that this is caused by the homothetic yield surface formulation.

To verify the applicability of the Masing behaviour, the backbone curve of the 3D FEA results is extrapolated to a hysteretic loop, while adhering to the extended Masing rules. Figure 3.10 includes the 3D FEA and the theoretical Masing response. The area enclosed by the Masing hysteresis loop is approximately equal to the area of the 3D FEA hysteresis loop. Thus, the 'squeezing' of the hysteresis loop, as is remarked by e.g. Kaynia and Andersen [50] does not occur for this load and soil profile combination.

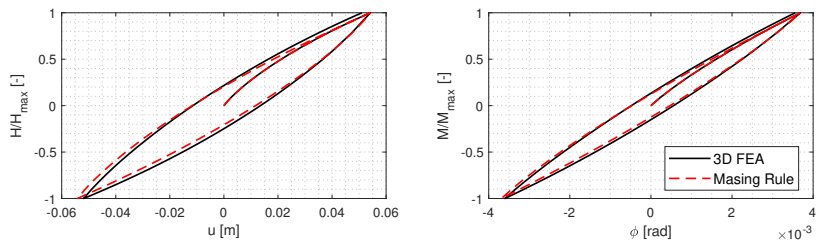

Figure 3.10: Results from 3D finite element analyses (——) of mudline response to extreme $H-M$ loads compared to theoretical response obtained with Masing rules (- - -).

Further, the behaviour upon reloading is slightly different for the Masing hysteresis loop, when compared to the 3D FEA results. It is postulated that the discrepancy is due to the checked *tension cut-off* in PLAXIS. This results in gap opening and thus an additional softening is included in the calibration curve and consequently gives different behaviour

upon loading in a different direction. This agrees with the behaviour of Figure 3.10, where the FEA predict a stiffer response upon unloading than the theoretical response derived from the backbone curve.

To conclude, the discrepancy between the macro-element model and the 3D FEA in Figure 3.9 is due to geometrical (gapping) effects, as well as the underestimation of the soil stiffness at the extreme load levels. Please note, a conservative estimate of the stiffness is admissible, as long as this does not cause a disproportionate overestimation of the foundation damping.

Planar Biased Cyclic Loading

Offshore environmental conditions rarely excite (two-way) symmetric cyclic loading on the offshore wind support structure. Therefore, one-way and two-way biased cyclic loading analyses are needed to verify the response of the macro-element excited to biased cyclic loading. In addition to the biased cyclic loads, multiple load cycles are applied in the finite element analyses.

Figure 3.11 depicts the loads at mudline in the H-M plane, as well of the number of cycles run over time. In total, the monopile is at seabed excited by 35 identical cycles with the same H/M ratio. The maximum base shear and moment are reduced, compared to the first analyses and are comparable with the verification loads that Page et al. [39] apply. The input loads are a result of fitting a normal distribution to an ULS time series of an OWT in production. The analyses cycle around the mean with two standard deviations, which cause the planar cyclic loading to be two-way (H) and one-way (M).

Figure 3.12 portrays the mudline response from the macro-element model and 3D FEA to the input loads of Figure 3.11. The agreement is very good, for both the one-way and two-way cyclic loading. As the maximum load is significantly lower than the maximum load in the planar two-way symmetric cyclic loading analysis, the stiffness from the 3D FEA and the macro-element model remains similar up to the highest load level. Further, Figure 3.12 implies that there is some ratcheting in the FEA results, that is not present in the macro-element model results. Please note, it is postulated that this ratcheting is pure numerical. Further, the FEA ratcheting in Figure 3.12 is much lower than the ratcheting that is predicted in Figure 3.9. This might be due to that the analyses in this section are run with the first version of the UDSM.

The formulation of the macro-element model is developed such that there is not accounted for ratcheting. Mainly, as any ratcheting in a 10-minute time series for FLS analyses is considered negligible. Further, accounting for ratcheting in a (constitutive) model is very challenging, as it usually results in additional numerical ratcheting. As numerical ratcheting is undesired, the response of the macro-element model to N = 1, 10, 100, 1000 load cycles is

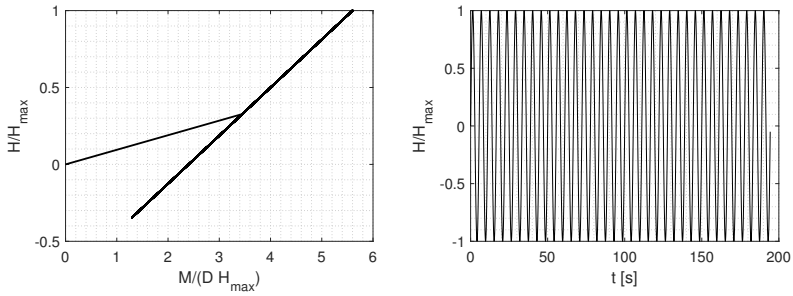

Figure 3.11: Normalised loads (H and M) at mudline that are used as input for the macro-element model and 3D FEA. N = 35 cycles. Bias of the cyclic loads: $H_{x,a}/H_{x,cyc}$ = 0.48 and $M_{y,a}/M_{y,cyc}$ = 1.60.

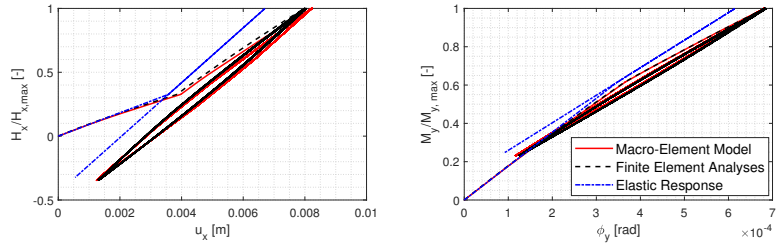

Figure 3.12: Normalised total and elastic displacements at mudline from the macro-element model and 3D finite element analyses to 35 identical planar two-way biased load cycles.Bias of the cyclic loads: $H_{x,a}/H_{x,cyc}$ = 0.48 and $M_{y,a}/M_{y,cyc}$ = 1.60.

checked. Figure 3.13 displays the macro-element model response to these load cycles. Due to the computational inefficiency of the finite element model, the study that assesses the number of cycles uses only the macro-element model. It is concluded that for the amount of cycles in a 10-minute time domain analysis ($N \ll 1000$) the macro-element model does not include any (significant) numerical ratcheting. Please note that soil-foundation behaviour when exposed to biased cyclic loading as observed in laboratory tests may experience ratcheting and, consequently, the soil response does no longer adhere to the Masing rules [49].

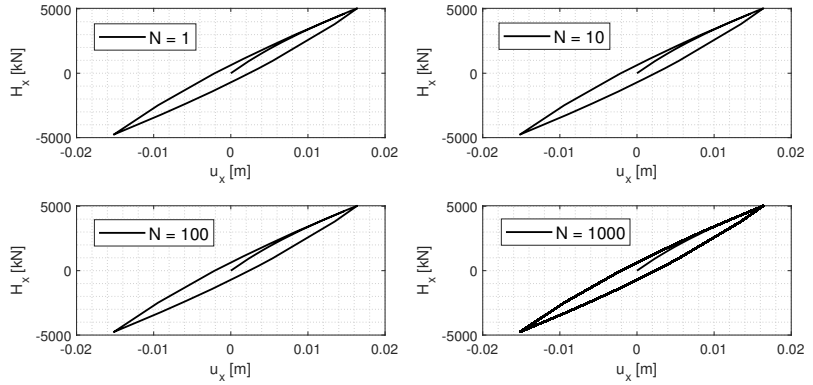

Figure 3.13: Response of macro-element model to N = 1, 10, 100, 1000 cycles for planar cyclic loading.

Multi-Directional Two-Way Biased Cyclic Loading

For an actual OWT the response is not purely planar, but multi-directional, due to wind-wave misalignment. Therefore, additional analyses that account for the multi-directionality aim to verify the response of the macro-element model with 3D FEA with UDSM *Von-MisesSeriesCoupled*. As an input, the finite element model and the macro-element model use the mudline response from ULS time series generated with BHawC. From the BHawC 10-minute time series, 10 seconds that contain the maximum moment are retrieved. Figure 3.14 presents the resulting normalised load time series at mudline. The input is normalised to H_x and M_y (S-S direction), as the actual loads are confidential. However, it should be noted that the maximum base shear and maximum moment are approximately 1.5 times larger than the extreme loads that Page et al. [39] apply. Please note, the maximum loads (H_y, M_x) applied in the multi-directional analyses are equal to the maximum load level in Figure 3.9. Further, it should be noted that Figure 3.14 and 3.15 present the mudline response as a function, however, note that the finite element and macro-element model analyses use static loads as an input.

Figure 3.15 shows the total and elastic displacements that correspond to the loads of Figure 3.14. The total displacements result from FEA and the macro-element model, while the elastic response may be found from Equation 2.2. The displacements of Figure 3.15 are compared to the response that is found with BHawC. The trend in the displacements compares well for the two models (BHawC and macro-element model/FEA), but the displacements

in BHawC, that use the non-linear elastic API *p-y* curves are significantly larger. This is attributed to the higher (initial) stiffness that is accounted for by the FEA.

Generally, the response from the macro-element model agrees satisfactorily with the FEA response. However, at the maximum load the macro-element model overestimates the displacements slightly in the *y*-direction (F-A), when compared to the 3D FEA results (right plots of Figure 3.15). This is coherent with the results from the planar symmetric extreme loading analyses, where the stiffness at the highest load level is underestimated. It is considered that the agreement is still sufficient.

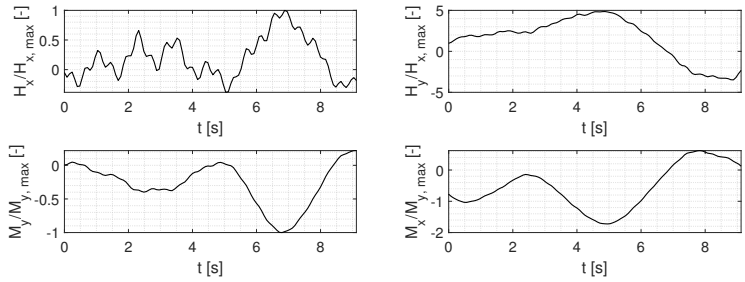

Figure 3.14: Input loads for the finite element and macro-element model analyses. The ULS loads result from BHawC and are larger than the extreme loads that Page et al. [39] apply.

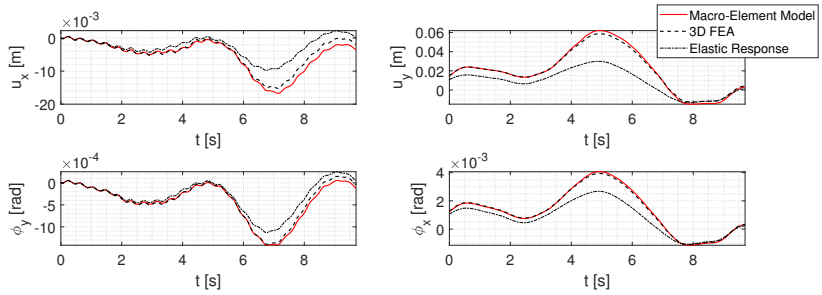

Figure 3.15: Displacements at mudline from finite element and analyses and the macro-element model. The displacements are a response to the ULS input loads from BHawC.

Additionally, there is a discrepancy between the macro-element model and the 3D FEA observed for the loading in *x*-direction (left plots of Figure 3.15). Here, the difference

between the macro-element model and 3D FEA holds over time. Therefore, it is postulated that the discrepancy is partially due to the tension cut-off that is accounted for in the FEA. Figure 3.9, that was discussed previously, depicts a different behaviour from the macro-element model and 3D FEA upon reloading, which is partially due to the underestimation of the stiffness upon high load levels. Additionally, Figure 3.10 evaluates to what extend the FEA follows the Masing rule. From this figure, it is concluded that the displacements upon reloading from the Masing rule are larger than from the FEA.

To conclude, the discrepancy in the top left plot of Figure 3.15 is due to 1) the underestimation of the stiffness at high load levels and 2) the tension cut-off that is accounted for in the FEA. The first argument influences the backbone curve, that is paramount in using the Masing behaviour, while the second argument shows that the FEA do not comply with the Masing rule.

Comparison of the Response from Integrated Analyses

The macro-element model shows that it captures the response well for a static applied load at mudline. Within integrated analyses, the macro-element model affects the dynamic response of the OWT. Consequently, the displacements at mudline are affected by the response of the support structure above the foundation model. Therefore, one comparison evaluates the response at mudline from the time domain simulation tool with the macro-element foundation model with the response from 3D finite element analyses.

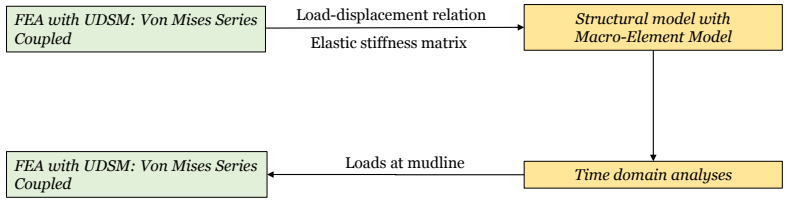

Figure 3.16: Comparative scheme for verifying the response from integrated analyses. Green: constitutive model used in PLAXIS. Yellow: support structure design tools used in MATLAB.

Figure 3.16 depicts the comparative scheme for verification of the response from integrated analyses. First, the macro-element model is calibrated against the response at mudline from the 3D FEA with the UDSM. Next, the OWT is excited by an arbitrary external load, that ensures a response at mudline with loads comparable to the ULS loads of the selected site.

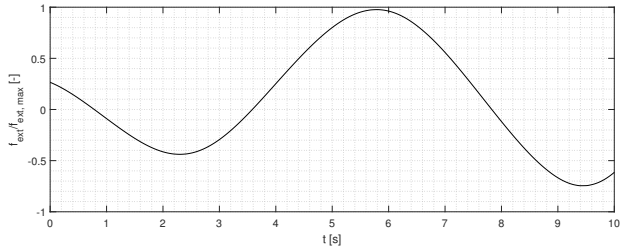

Figure 3.17: Normalised distributed external wave load in fore-aft direction at LAT. Input to time domain simulation tool.

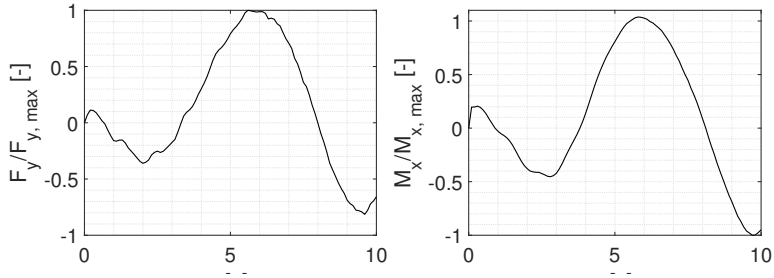

Figure 3.18: Normalised mudline response from the integrated foundation design tool of SGRE with macro-element foundation model. Input for load-controlled 3D finite element analyses.

To complete the cycle, the 3D FEA with the UDSM in PLAXIS uses the mudline response as input. The performance of the macro-element model in integrated analysis is verified by comparing the mudline internal forces from the time domain analysis and 3D FEA with the UDSM.

Figure 3.17 shows the first 10 seconds of the external force in F-A direction at lowest astronomical tide (LAT). In order to trigger plastic displacements in the first 10 seconds of the analyses, the external load of the test case (Appendix B) is multiplied with a factor 4. Note, the external force is distributed over the length of the support structure that is or comes into contact with water, during the wave load. The distributed wave load is proportionally distributed to the nodes from the structural elements that come into contact with water.

Figure 3.18 depicts the mudline response due to the wave loading. The magnitude of the response at mudline from the TD simulation tool compares well to the magnitude of

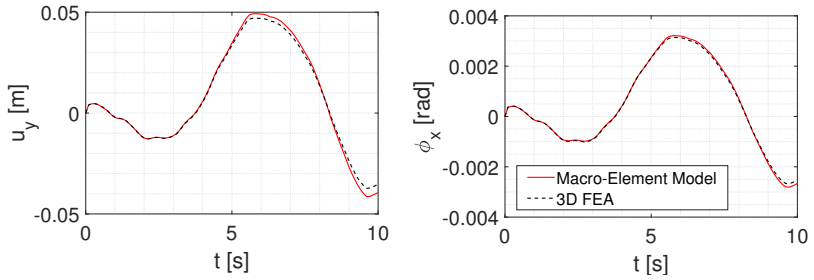

Figure 3.19: Mudline displacements from the integrated foundation design tool of SGRE with macro-element foundation model and in the finite element analyses.

the response that is used for the multi-directional two-way biased cyclic loading analyses (Figure 3.14). The displacements at mudline that correspond to this response are displayed by Figure 3.19. Overall, the agreement between the 3D FEA with the UDSM and the results of the time domain simulation with the macro-element model is satisfactorily. However, at the peak load, the macro-element model overpredicts the displacements. This may be due to the underestimation of the stiffness, as is also observed in Figure 3.9. It should be taken into account that the stiffness and hysteretic damping prediction are strongly dependent on each other. Therefore, any significant discrepancies may result in a too large hysteretic damping contribution, when compared to 3D FEA (i.e. no longer conservative behaviour). However, the predicted response of the macro-element model in Figure 3.19 seems conservative with respect to the 3D FEA with the UDSM.

Please note, a second analysis includes a verification with the SSI from API *p-y* curves calibrated with soil parameters of the selected site, giving a much softer load-displacement curve at mudline. The displacements at mudline caused by excitation with the load time series of Figure 3.18. Again, the agreement between the macro-element model and 3D FEA with the UDSM is satisfactory. The results are included in Appendix C.2.

Sensitivity Study

To assess the effect of different soil strength and stiffness parameters on the agreement of the macro-element model with 3D FEA, a sensitivity study is performed. Besides evaluating the performance of the macro-element model for additional sites, the reduction in strength may also be due to an extreme event at the site in question. Hence, determining the effect of soil stiffness reduction is a vital part in verification of the macro-element model. Since in the UDSM the strength parameters are dependent on the stiffness parameters, merely the

stiffness of the soil is reduced. Besides adjusting the input parameters in the UDSM, also the stiffness and strength properties of the interfaces are reduced. These changes will result in increased non-linear behaviour at mudline. Figure 3.20 depicts the input calibration curves for the macro-element model, for the 'full stiffness profile' (FSP) and 'reduced stiffness profile' (RSP) model. The stiffness of the reduced stiffness model is reduced by a factor of $1/3$ for all yield surfaces. The distribution of the yield surfaces is kept constant.

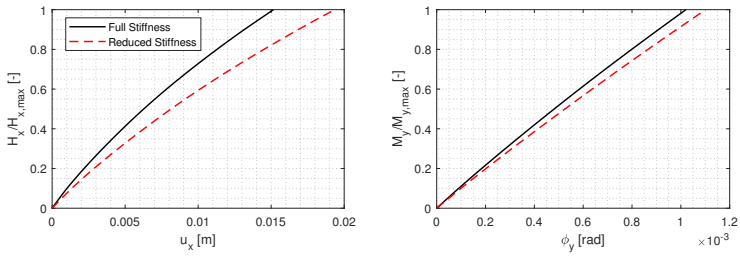

Figure 3.20: Input calibration curves of the macro-element model for full and reduced stiffness and strength. For brevity, the $H - \phi$ and $M - u$ curves are omitted.

Figure 3.20 demonstrates that the softer response of the reduced stiffness soil profile. The sensitivity study evaluates the performance of the macro-element model by executing multi-directional two-way biased cyclic loading analyses. The input loads are equal to the normalised loads that Figure 3.14 depicts. The corresponding displacements are included in Figure 3.21. Similarly as the FSP response (Figure 3.15), the agreement between the macro-element model and the FEA predicted displacements is sufficient.

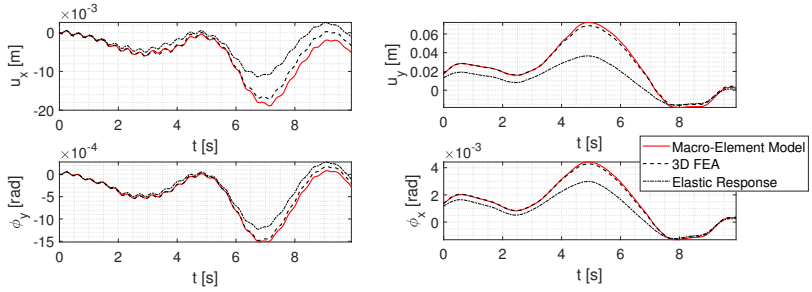

Figure 3.21: Displacements at mudline from finite element analyses and the macro-element model calibrated to the 'reduced stiffness profile'. The displacements depict the response to the ULS loads at mudline from BHawC.

The response of Figure 3.15 and 3.21 is very similar for the loads applied. The main differences are the larger elastic and total displacements for the RSP, when compared to the FSP response. The discrepancies in the response are similar for both models, and do not seem amplified for the response of the RSP.

3.4 Discussion

The response of the multi-directional macro-element model and the 3D FEA is found to be very comparable, also for higher load levels than used for verification by Page et al. [39]. As the finite element model and the macro-element model are based on the same constitutive relations, the difference in the response is due to the 'scaling' of the response from a 3D model to a macro-element model formulation. In the 3D model, there is accounted for 3D effects, as the response of the soil-pile continuum affects the response at mudline, while the response of the macro-element model is not governed by its surrounding soil. Instead, assumptions on the behaviour of the SSI at mudline (e.g. Masings rule) are made, to approximate the behaviour of the 3D model. Due to these 3D effects, it is not possible for the macro-element model to capture the response for all loading scenarios. Therefore, the following paragraphs discuss the limitations of the macro-element model and place these in perspective with respect to other studies that assess the limitations of the foundation model.

Foremost, it should be noted that the response of the multi-directional macro-element model is predominantly assessed using 3D FEA with the UDSM, where it is assumed that the 3D FEA, in particular the UDSM *VonMisesSeriesCoupled*, captures the actual SSI. Naturally, the 3D FEA with the *VonMisesSeriesCoupled* constitutive model cannot capture the actual soil response to cyclic loading, especially for non-cohesive soils. For instance, the stress-dependency of the stiffness is merely approximated (by accounting for multiple layers) and ratcheting, cyclic degradation, pore pressure accumulation/(partial) drainage are not included in the analyses. Therefore, it is crucial to note that the very good agreement between the macro-element model and 3D FEA with the UDSM is due to the fact that the models are based on the same constitutive relations. However, the macro-element model is expected to capture the cyclic soil behaviour adequately also when calibrated against FEA with other constitutive models, laboratory and/or field tests. As long as the soil-pile response at mudline adheres to the Masing rules.

With regards to capturing the 3D effects in a macro-element model, Page (private communication) performed a first analysis to assess the limitation of the macro-element model in ULS conditions. For stiff soils, i.e. limited non-linear behaviour, the response between the macro-model and the finite element analyses agree very well. Upon a reduction of the stiff-

ness and strength by respectively 40 and 70%, the non-linearity of the behaviour is increased and the predicted response from the macro-element model and 3D FEA with the UDSM *VonMisesSeriesCoupled* constitutive model start to deviate in the analyses of Page (private communication). The main cause of the discrepancy is due to the presence of gapping, while the macro-element model adheres to the Masing rules, while 3D FEA with the UDSM does not for these load levels. First, this causes an overestimation of the soil damping, with respect to FEA. Further, this results in an underestimation of stiffness during unloading and reloading. Slightly similar behaviour is observed in the response to the multi-directional and planar loading cases as performed for this thesis. For the cases considered, this does not have any significant influence on the material damping estimation. However, it should be noted that the results are to be interpreted with care.

It should be noted that the behaviour at mudline is very stiff, as the pile geometry is determined with API *p-y* curves for the SSI and 3D FEA with the UDSM/HSsmall model generally predicts a more stiff behaviour of the monopile at mudline. Therefore, additional analyses are performed that account for SSI that is comparable to the SSI defined by the API *p-y* curves (Appendix C). The macro-element model captures the response at mudline well, also for soil-foundation stiffness comparable to the the SSI as defined by the API $p - y$ curves.

From Page et al. [39] it is deduced that for loads that have an abrupt change in direction, the response at may not be accurately captured. This is due to the model formulation, that not accounts for non-consecutive yield surfaces to be active at the same time. This may result for an initial too stiff response to the load, followed by quick softening of the soil-foundation stiffness. For the application of the macro-element model in the time domain simulation tool of SGRE, this limitation may be disregarded, as the tool until now merely excites uni-directional loads on the OWT. However, in the load-calculation software BHawC there is accounted for multi-directionality of the environmental loads. Depending on the arrangement of the yield surfaces, the model algorithm may underestimate the response for cases where there is accounted for gusts and changing wind direction or fault cases. Therefore, it is recommended to include the binary solution algorithm, that was implemented by Grimstad (private communication) in the UDSM, in the macro-element model.

Further, for high load levels a gap may form around the monopile, as is observed in the finite element analyses, when the monopile is exposed to high load levels. Because a gap is formed in both the monotonic and the cyclic finite element analyses, the phenomenon is included in the calibration curves. However, the typical butterfly shape for the hysteresis loop cannot be approximated with the macro-element model or the 3D FEA with the UDSM *VonMisesSeriesCoupled*. Hence, this will cause an overestimation of the soil damping at these load levels, as well as give an inaccurate prediction of the soil stiffness (reference is made to Section 2.2). It should be noted, though, that for the predominant part, offshore wind turbines have

some form of scour protection installed. The scour protection results in additional layer of rocks, around the monopile. The scour protection provides additional lateral resistance to the monopile, which results in decreased probability of gap formation at mudline. Therefore, the likelihood of a gap formation is challenged and consequently, including the gapping phenomenon in the numerical models is considered to be optional.

3.5 Summary

This chapter focuses on numerical analyses, that are performed to analyse the response of the macro-element model when exposed to high load levels for the length of a 10-minute time series. First, the model set-up in the commercial software *PLAXIS 3D* and choice of the constitutive models used in the finite element analyses is explained. As the *Hardening Soil Small Strain* (HSsmall) model is not developed to be used to model the cyclic behaviour of soils, the user-defined constitutive model (UDSM) developed by Page et al. [39] is applied. The advantage of the latter model is, is that it is based on the same constitutive equations as the macro-element model. Hence, the comparative analysis purely focuses on how well the macro-element model captures the response of the 3D soil continuum. However, it should be acknowledged that the ability of the UDSM *VonMisesSeriesCoupled* constitutive model to capture the soil-foundation response is limited.

After calibration of the user-defined soil model and the macro-element model, the predicted response is compared for monotonic and cyclic loading. The macro-element model response to planar/multi-directional symmetric/biased cyclic 'ULS' loading to the 3D FEA compares adequately. When exposed to the maximum loads of the ULS case, the macro-element model slightly overestimates the predicted response from 3D FEA, in planar and multi-directional cases. In the performed analyses, it is concluded that this underestimation of the soil-foundation stiffness does not result in a significant overestimation of the hysteretic damping. To conclude, the macro-element model is considered to capture the SSI at mudline sufficiently for application in integrated analyses for OWTs exposed to extreme loads.

Chapter 4

Case Study

4.1 Introduction

Following the successful development of offshore wind energy in Western Europe, offshore wind energy is quickly gaining momentum in the Asia-Pacific (APAC) region. Even though the water depths in the APAC region are comparable to the water depths of the North Sea, not all environmental conditions are as suitable for offshore wind. Hence, new challenges are introduced in the development of offshore wind farms. One of the challenges as identified in the APAC region is the prevalence of typhoons, which causes the environmental loads to be significantly larger in storm conditions. This is coherent with results from SGRE, where it is found that for an OWF under development the extreme (wave) loads are governing the response at interface level. As initial research shows that an increased soil stiffness positively affects the magnitude of the dynamic response at interface, the objective of this chapter is to assess the influence of the hysteretic behaviour of the macro-element model on the response at interface level.

In this chapter, first the site and support structure characteristics are outlined. As the OWF is still being developed, all parameters are normalised. Next, the (calibration of the) foundation models in the comparative analyses are discussed. It is decided to perform the comparative analyses with a Winkler and macro-element model calibrated against the API *p-y* curves, to assess the effect of the hysteretic behaviour. In addition, the same analyses are performed with a macro-element model calibrated against 3D FEA with the HSsmall constitutive model.

4.2 Site and Support Structure Characteristics

The offshore wind farm is located in the Asia-Pacific (APAC) region. The region is known for its severe environmental conditions, as typhoons may occur. This causes a large increase of the ULS loads, when compared to ULS loads that are obtained for North Sea based OWFs. Here, a short description of the site characteristics are presented. As the OWF is under development, all data is normalised. Note, the data presented here is for one OWT location.

Soil Profile

As the OWF is currently under development, only soil data from CPTs is available. At the location, a layered soil with a mixture of sand and clay is found. The stiffness profile as depicted in Figure 4.1 shows the normalised stiffness parameters, that may be used for the HSsmall constitutive model. It is observed that the highest soil stiffness is found in the top layers, while the stiffness reduces in the lower layers. In Figure 4.1 an interpreted HSsmall stiffness profile from CPTs is shown, as well as a simplified soil profile. The simplified soil profile is used in the required finite element analyses with the HSsmall model, as this decreases the computational time. Please note, the profile for E_{oed} and E_{ur} are omitted as for this analyses it is assumed that $E_{oed} \approx E_{50}$ and $E_{ur} = 3E_{50}$.

The simplified soil profile is deduced using the following procedure: first, sand and clay layers are distinguished. So, within the simplified soil profile, the cohesive and non-cohesive soils are not merged, as they have different soil properties. Within the HSsmall model this is included in two ways: in the strength parameters and secondly in the exponent m that determines the stress dependent stiffness. Further, small layers ($z < 0.25D$ m) are merged with bigger layers of the same soil type. This is considered to be valid, as the area of the cone used for the CPT is much smaller than the monopile foundation. Due to variations in the soil layering in horizontal space, it is likely that the small soil layer is not present on all soil-monopile interfaces. Instead, a weighted average is included of the strength and stiffness parameters of the soil layers that are merged.

Next to the stiffness profile, the strength profile of the chosen location is shown in Figure 4.2. The visualised strength profile depicts the total and effective strength input parameters for the HSsmall constitutive model of the simplified soil profile only. In offshore conditions, non-cohesive soils may dissipate excess pore pressures, due to higher permeability, when compared to cohesive soils. However, during storm loading non-cohesive soils are also considered to behave undrained, following Kementzetzidis et al. [82]. Further, it is assumed that the strength parameters are constant for each layer and thus, the mid-point that is depicted in Figure 4.2 reflects the strength of the entire layer.

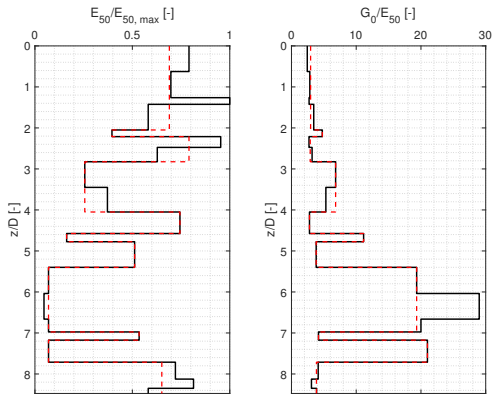

Figure 4.1: Normalised Hardening Soil Small Strain stiffness input parameters from cone penetration tests (——) and simplified profile for selected site (- - -). $E_{oed} \approx E_{50}$ and $E_{ur} = 3E_{50}$

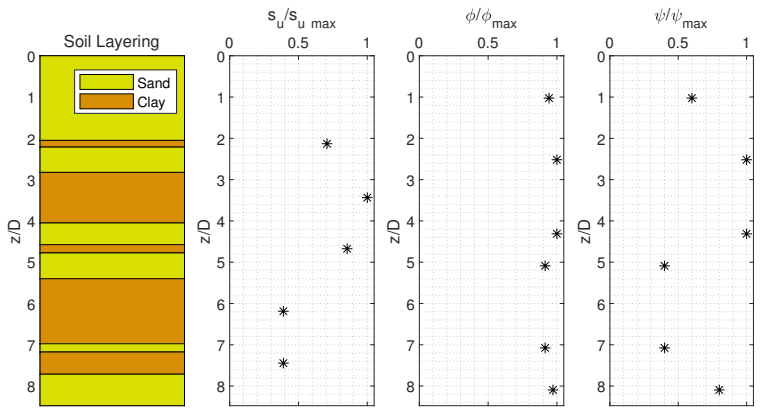

Figure 4.2: Normalised strength profile for the for the simplified profile of the selected site interpreted from cone penetration tests. Total and effective strength parameters are plotted for the middle of each layer

Modelling of the Support Structure

The modelling of the support structure is divided into two parts: 1) the fixed structural model that contains the mass, damping and stiffness matrices for the structural model and 2) the variable foundation model that determines the SSI. The properties of the foundation model ($\boldsymbol{M}, \boldsymbol{C}, \boldsymbol{K}$) are added to the structural model.

Structural Model

Within the structural model the support structure is modelled as Timoshenko beams with 6 DoF per node ($u_{x,y,z}, \phi_{x,y,z}$). The mass of the elements and add-ons, e.g. the boatlanding, are proportionally divided over the nodes. Structural and hydrodynamic damping is included as modal damping. The modal damping is defined as a percentage of critical damping and the magnitude is mode dependent. The first modes are slightly more damped than the second modes. Further, the RNA is modelled as an equivalent lumped mass and corresponding rotational inertia. The input to the structural model is based on the preliminary support structure design drawings that are provided by SGRE. The thickness and diameter of the support structure vary over the height. For calibration of the macro-element model, however, the bending stiffness EI is averaged over the embedded length of the monopile, for simplicity. Please note, the support structure geometry is determined from design analyses that use API p-y curves for modelling of the SSI.

Foundation Models

To assess the influence of the non-linear hysteretic soil-structure interaction on the dynamic response of the OWT support structure, two foundation models are used in integrated analyses. The first foundation model is the non-linear elastic API p-y curves that are distributed along the length of the monopile. Secondly, the non-linear hysteretic macro-element model is included, that models the foundation as force-displacement relations at mudline. In order to qualify the effect of the hysteretic behaviour of the response at interface level, the macro-element model is calibrated against the API pre-defined curves (MEM1). In addition, the macro-element model is calibrated against 3D FEA with the HSsmall constitutive model, as this gives a different description of the response of the monopile at mudline (MEM2).

API p-y Curves
The p-y springs of the Winkler model are calibrated against the API pre-defined curves [22]. As the foundation model is used in extreme load analyses, a cyclic degradation factor is included in the calibration of the lateral soil reaction curves.

Macro-Element Model

First, the macro-element model is calibrated against the API p-y curves, by obtaining an elastic stiffness matrix and load-displacement curves at mudline from 1D analyses. The verification analyses of the correct implementation of the macro-element model in the structural model show that for higher modes the difference in the natural frequency prediction increases. Even though only the first two modes contribute mostly to the response in the extreme load analyses, a frequency independent monopile mass is added to the node at mudline (see Appendix B). This results in a smaller difference in estimated eigenfrequency between the API p-y curves and MEM1 for the higher modes.

For the 3D FEA calibration with the HSsmall model, a soil-pile continuum is created in the commercial software PLAXIS 3D. The 3D continuum is based on the 3D finite element model as given by Figure 3.2 and thus accounts for symmetry conditions. The pile is modelled as a linear elastic volume pile with the same bending stiffness as the monopile. Interface elements are placed between the soil and the pile. The stiffness of the interface equals the soil stiffness and the interface has a strength reduction of 2/3. The elements (10-noded) within a $1.5D$ radius of the monopile are approximately four times smaller than the elements outside this radius, with a total of 109,235 elements.

Figure 4.3 shows two of the four load-displacement curves at mudline calibrated against the pre-defined API functions and 3D FEA. The curves underline the consensus that the API p-y curves predict a too soft initial soil-monopile response for low L/D piles.

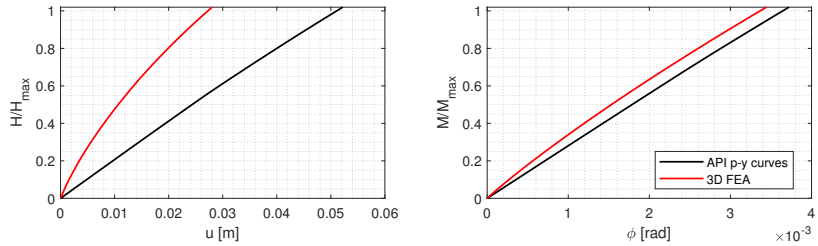

Figure 4.3: Normalised load-displacement curves at mudline obtained for soil-structure interaction modelled with API p-y curves (MEM1) and 3D finite element analyses with the HSsmall model (MEM2). For brevity, the H-ϕ and M-u curves are omitted.

As the mudline response of the API p-y curves is much softer than the response from 3D FEA, the validity of the verification analyses of Chapter 3 is questioned. The verification analyses of Chapter 3 include quite stiff soil, resulting in limited displacements at mudline. Page (private communication) shows that the comparison of the macro-element model and

3D FEA (UDSM *VonMisesSeriesCoupled*) becomes less well for softer soil. This results in a significant stiffness underestimation and damping overestimation by the macro-element model when compared to the response of 3D FEA. Therefore, the same multi-directional comparative study is performed as in Chapter 3 for a soil with similar initial stiffness as MEM1. The results, that are included in Appendix C.2, show that the macro-element model is able to capture the planar response sufficiently.

4.3 Results

To analyse the effect of the macro-element model in comparison with the current industry standard for foundation modelling on the response at interface level, time domain analyses are performed. Below, first the prediction of the natural frequency is compared, followed by the results of the support structure integrated analyses in the frequency domain. It should be noted that the analyses are performed with the RNA modelled as a point mass and hence the influence of the blade modes on the dynamic response is not included.

Natural Frequencies

With both the foundation models calibrated, the natural frequencies of the two models may be obtained. As the macro-element model is a non-linear model, the natural frequency calculation uses the elastic stiffness matrix as an input. In the PSD of the response for an OWT exposed to large environmental loads, the dominant response frequency may degrade due to the non-linear soil stiffness of the foundation models.

Considering that the time domain simulation tool merely allows for uni-directional loading conditions, the natural frequencies in the F-A direction are included in Table 4.1 for the first four modes. Additionally, Table 4.2 presents the relative differences of the estimated natural frequencies with respect to the predictions from a structural model supported by API *p-y* curves. MEM1 slightly underestimates the eigenfrequencies with respect to the API *p-y* curves. This is due to the frequency independent mass that is added to the node at mudline (see Appendix B). In case there is not accounted for this mass, MEM1 gives slightly larger estimates of the natural frequency. Note, the natural frequencies are obtained for a support structure with elastic (i.e. non-degraded) stiffness at mudline.

In addition, the mode shapes are illustrated in Figure 4.4. MEM1 follows the mode shape of the support structure supported by a Winkler model with API $p - y$ curves very well, while MEM2 exhibits stiffer response than the foundation models calibrated to the API pre-defined functions. This is expected, as the initial soil-foundation stiffness is much higher, as Figure 4.3 depicts. It is seen that the mode shape of the support structure with

Table 4.1: Comparison of the predicted natural frequency of the first four modes of the fore-aft, using API *p-y* curves and the macro-element model (MEM1 and MEM2) as foundation model for the selected offshore wind farm

	API *p-y* curves	**MEM1**	**MEM2**
f_0 [Hz]	0.2363	0.2361	0.2534
f_1 [Hz]	0.8087	0.7976	1.0107
f_2 [Hz]	1.7972	1.7778	1.9469
f_3 [Hz]	3.3119	3.2474	3.5339

Table 4.2: Relative difference from MEM1 and MEM2 foundation model with respect to the API *p-y* curves estimates of the natural frequencies

	f_{MEM1}/f_{API}	f_{MEM2}/f_{API}
1st mode	0.9991	1.0724
2nd mode	0.9863	1.2497
3rd mode	0.9892	1.0832
4th mode	0.9805	1.0670

MEM2 foundation model is not exactly similar to the mode shape of the support structure supported by MEM1/API $p-y$ curves. From evaluating the modal amplitudes as shown in Figure 4.4 it is concluded that the MEM2 foundation model for the higher order modes may give larger modal amplitudes than the models calibrated to the API standard. This effect is attributed to the different stiffness matrices at mudline. The translational stiffness (K_{11}) of the MEM2 foundation model is approximately ten times larger than for the MEM1 foundation model. The rotational stiffness (K_{22}), on the other hand, is more or less equal. The difference in the scaling of the elastic stiffness matrix may cause the different behaviour above mudline.

Initially, it was postulated that the difference in the mode shapes for the higher order modes is due to the calibration of the macro-element model, that accounts for quasi-static behaviour at mudline. However, it is concluded that this does not influence the modal amplitudes of the higher mores, as the mode shapes resulting from a support structure with a Winkler model supported by API *p-y* curves and the MEM1 foundation model agree well. Thus, the difference in the mode shapes may be fully attributed to the different soil-foundation stiffness at mudline.

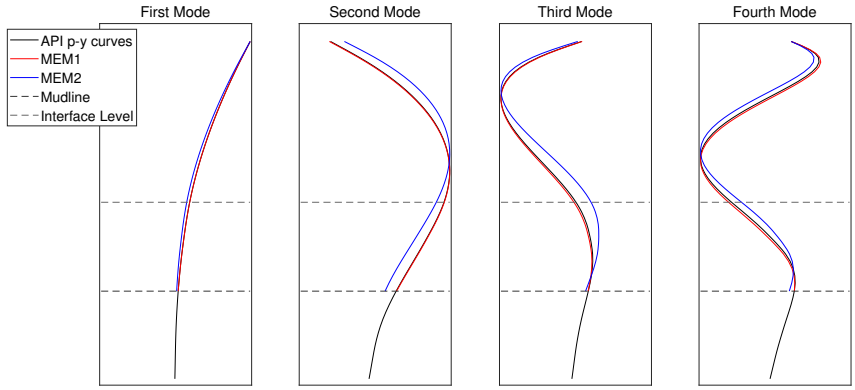

Figure 4.4: Mode shapes of the first four modes of the F-A direction for the three different foundation models: API *p-y* curves, MEM1 and MEM2

Time Domain Analyses

In order to assess the impact of the different foundation models on the dynamic response of the OWT exposed to extreme loads, time domain analyses with the governing design load case (DLC) are performed. To account for the stochastic nature of the environmental loads, the analysis uses nine different seeds. The DLC consists of wave-only loads, as the foundation design tool of SGRE merely models the RNA as a top mass. Thus, no aerodynamic damping nor effect of the pitch-control system on the loads are considered. Further, the direction of the external loads that may be applied in the time domain analyses tool is limited to a single, y, direction.

The wave loading in combination with the motion of OWT determine the response of the OWT to the wave. Therefore, the impact of the foundation modelling on the dynamic response cannot be compared in the time domain, as the foundation models influence the behaviour of the OWT in a different manner. Therefore, it is considered that comparing the PSD of the response for the different foundation models is more insightful.

This section focuses on the response of the offshore wind turbine at mudline and at interface level, for the different foundation models. The interface level is defined as the interface between the sub-structure and the tower [1]. The foundation models are 1) the current industry standard: a Winkler model on non-linear elastic API *p-y* curves [22] and 2) the non-linear elasto-plastic macro-element model calibrated against the API *p-y* curves (MEM1)

and 3) the macro-element model calibrated against load-displacement curves from 3D FEA (MEM2) [39]. From the models calibrated against the API standard, the effect of accounting for the load-dependent stiffness and damping on the response at interface for extreme load cases is determined. As the macro-element model determines the hysteretic damping, the soil damping is deduced from the total modal damping (includes structural, hydrodynamic and soil damping) in the structural model. Further, since the API p-y curves account for too soft initial stiffness, the effect of a more realistic soil-foundation stiffness is additionally evaluated with MEM2.

Figure 4.5 depicts the distributed unidirectional external wave load at LAT for simulation 1, 2 and 3. The waves correspond to an extreme sea state (ESS) where the significant wave height equals the 50-year wave. Further, due to the extreme wind speeds, the turbine is idling [83]. This case study assesses the dynamic response to the maximum wave loads, thus only the response to the ESS consisting of wave time series with the largest peak period and highest water level is given (THWH).

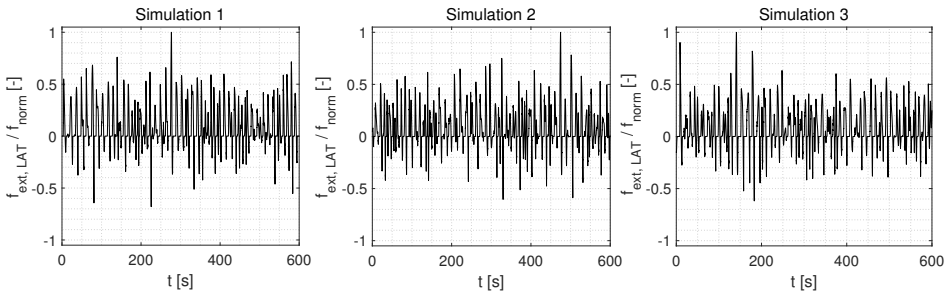

Figure 4.5: Distributed unidirectional external wave load at lowest astronomical tide for simulation 1, 2 and 3. Normalised to peak external force of simulation 1 (f_{norm}).

Response from API *p-y* curves and Macro-Element Foundation Model 1

Figure 4.6 and 4.7 depict the PSD of the dynamic response (M) at interface level and at mudline for a semi-logarithmic and linear scale. The first mode dominates the response of the OWT at mudline and at interface level. Further, the response at the peak of the wave energy spectrum ($f \approx 0.08$ Hz) is similar for the two models, highlighting the similar stiffness.

The predominant difference of the models is the magnitude of the peaks of the response at the resonant frequencies (note, as the system is non-linear, the resonant frequency is dependent on the load level). From Figure 4.7 it is clear that for the first mode the magnitude of the

response of the OWT with the macro-element foundation model is lower than the system that includes a Winkler model supported by API *p-y* curves. Similar results are observed for the response at the second mode, that may be activated in extreme load analyses. These differences may be attributed to the hysteretic behaviour of the macro-element model.

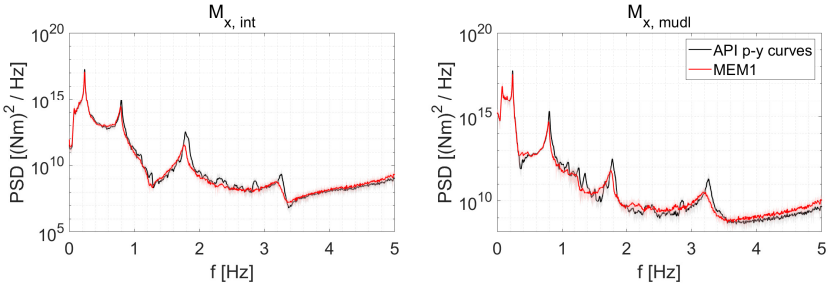

Figure 4.6: The power spectrum density of the response (M) at interface level (left) and mudline (right) for a structural model with two foundation models: API *p-y* curves and MEM1 (semi-logarithmic scale). Shaded area denotes the range of the response for simulations with different seeds.

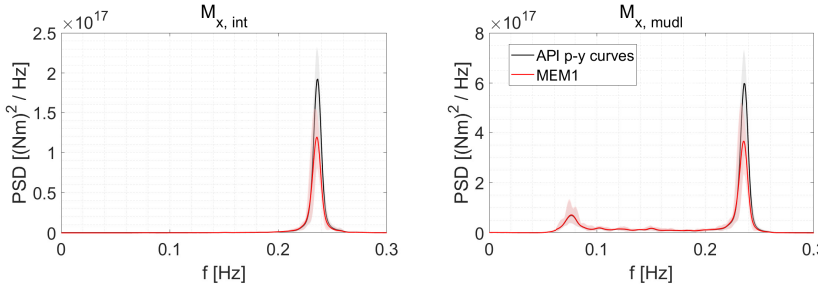

Figure 4.7: The power spectrum density of the response (M) at interface level (left) and mudline (right) for a structural model with two foundation models: API *p-y* curves and MEM1 (linear scale). Shaded area denotes the range of the response for simulations with different seeds.

Further, Figure 4.7 shows that at interface level the energy in the response spectrum is mostly present around the first mode, while for the PSD at mudline, also energy is focused around the environmental loading frequency. As the interface level is designed not to come into contact with water, it is coherent that there is no peak observed in the PSD at the environmental

loading frequency.

Response from Macro-Element Foundation Model 1 and 2

It has generally been accepted that the API pre-defined curves do not accurately describe the SSI for low L/D piles, as other soil reactions become increasingly important (e.g. [25, 46, 84]). One of the inaccuracies of the API p-y curves is in significant underestimation of the initial stiffness. Hence, to evaluate the dynamic response other than qualitatively, the response of MEM1 is compared with the response obtained with the MEM2 foundation model. The latter model is calibrated against 3D FEA, in contrast with MEM1 that is calibrated against the API p-y curves.

Figure 4.8 depicts the PSD of the response at interface level (left) and mudline (right) on a semi-logarithmic scale. The response of the MEM2 model is, as expected, stiffer than the response of the MEM1 model. This is clear from the resonant frequencies that are shifted more to the right side of the spectrum, indicating stiffer behaviour. Furthermore, the peaks at the resonant frequencies are generally much lower for the MEM2 foundation model than for the MEM1 foundation model. The response in the third mode at interface level, however, does not follow this trend. This may be explained from the mode shapes of the support structure that are included in Figure 4.4. In the third mode, the amplitude of the mode shape at interface level for the MEM2 foundation is larger than the the amplitude for the MEM1 foundation model. It is postulated that this is due to the larger curvature at mudline of the MEM2 model, when compared to the MEM1 model.

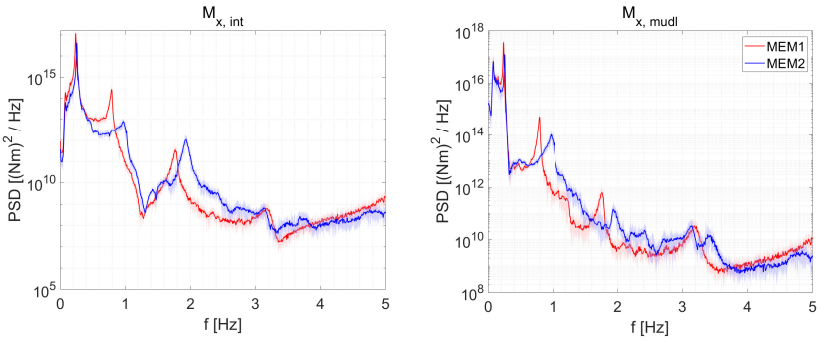

Figure 4.8: The power spectrum density of the response (M) at interface level (left) and mudline (right) for a structural model with two foundation models: MEM1 and MEM2 semi-logarithmic scale. Shaded area denotes the range of the response for simulations with different seeds.

Figure 4.9 presents the same response as Figure **??**, but then on a linear scale. The response at the peak excitation frequency of the environmental loads ($f \approx 0.08$ Hz), is very similar, however, the MEM2 model shows somewhat stiffer behaviour. In this case, the OWT is parked and thus the response in the first mode is dominant, as there is no aerodynamic damping included. The dominant response in the first mode is significantly lower for the MEM2 foundation model, calibrated against 3D FEA. The differences between the response in both resonance frequency and the magnitude of the response at this frequency predominantly highlights the inapplicability of API *p-y* curves to determine the SSI for piles with increased rigidity.

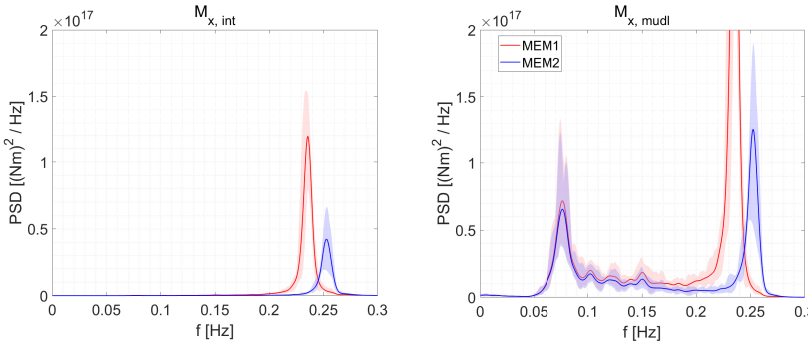

Figure 4.9: The power spectrum density of the response (M) at interface level (left) and mudline (right) for a structural model with two foundation models: MEM1 and MEM2 (linear scale). Shaded area denotes the range of the response for simulations with different seeds.

4.4 Discussion

From the results in the frequency domain, the effect of including hysteretic behaviour of soil on the dynamic response of OWTs exposed to extreme loads is apparent. Katsikogiannis et al. [38] indicate that the effect on the response in the first mode is best observed for idling cases, as the impact of aerodynamic damping, that is present in operating cases, on the response is larger. The effect of the foundation model in operating cases influences the response in the range of the excitation frequencies of the environmental loads. This effect, as may be observed in Figure 4.7 and 4.9 that depict the PSD in the linear scale. From these figures, it is deduced that the response in this frequency range is largely driven by the (initial) stiffness of the soil. The response with the API *p-y* curves and MEM1 foundation model is essentially the same. Comparing the response of the MEM1 and MEM2 foundation model,

the effect of accounting for different soil-foundation stiffness is observed.

For the assessed idling case, soil damping is the main source of damping for the support structure. As the MEM1 and MEM2 model both exhibit hysteretic behaviour, the difference in the response as Figure 4.8 and 4.9 is currently attributed to the difference in the calibration curves (Figure 4.3). Due to the different input curves, the hysteretic behaviour, and more specifically the hysteretic damping contribution, is different. To determine the effect of the hysteretic damping contribution from different calibration curves, it is suggested to determine the non-linear damping contribution from the macro-element model to the system damping. There is elaborated on damping estimation strategies for non-linear systems in Chapter 5.

Further, the fact that both foundation models do not account for cyclic degradation phenomena should be taken into account while interpreting the results. As opposed to FLS analyses, these effects (e.g. strength and stiffness reduction, pore pressure accumulation, ratcheting) may become important in 10-minute time domain ULS analyses. It is the generally accepted that cyclic degradation due to extreme loads may result in a reduction in soil stiffness and strength (e.g. [52, 1]), however, Abadie et al. [49] observe in laboratory tests stiffening behaviour for the first few (i.e. 50) load cycles. However, the extend to which the initial stiffening occurs is dependent on the load amplitude. Therefore, Abadie et al. [49] question the recommendation of DNV [1] to use a stiffness degradation factor on soil exposed to cyclic loading. Although, it should be noted that this stiffening behaviour is thus far only observed in laboratory tests for low-density sands. Considering that the predominant part of the soil layers of the evaluated site are classified as loose sand, it is postulated that neglecting cyclic effects does, in this case, not result in an overestimation (e.g. too stiff behaviour) of the SSI at mudline.

An additional limitation of the analyses as shown here is on the reliability of the soil data. The HSsmall parameters are obtained from CPT tests using empirical relations. The behaviour of the monopile at mudline will differ if the soil input data from laboratory tests is used. Considering that the macro-element model is intended for application in the final design stages, the required data is usually available.

4.5 Summary

For an OWT in the APAC region, an ULS design load case governs the dynamic response at interface level. The impact of foundation modelling on the dynamic response is evaluated by including three foundation models in time domain analyses: 1) the current industry standard based on non-linear elastic API *p-y* curves [22] and 2) the non-linear elasto-plastic macro-element model calibrated against the API *p-y* curves (MEM1) and also load-displacement

curves from 3D FEA (MEM2).

The results from the comparison of the API *p-y* curves versus MEM1 show the impact of the hysteretic behaviour on the dynamic response. For all modes, the MEM1 model reduces the maxima of the peak loads at the resonant frequencies. This difference may be fully attributed to the hysteretic behaviour of the macro-element model. There is no reduction of the response observed in the frequency range of the environmental loads, suggesting that the effect of the hysteretic behaviour is negligible in this frequency range.

The second analyses focuses on the impact of calibration curves from 3D FEA, when compared to SSI from API *p-y* curves. The calibration curves from 3D FEA with the HSsmall moodel (MEM2) have a much higher (initial) stiffness of which the effect is seen in the power spectral densities. First, an increase of the resonant frequencies is seen, as well as an reduction of the resonant peaks for the first two modes, that dominate the response of the support structure. It is suggested to evaluate the hysteretic damping contribution of these different macro-element models as to determine the effect of using the macro-element model for different calibration curves.

Chapter 5

Implication of Non-Linearity on System Damping Estimation

5.1 Introduction

In the ultimate limit state, it is suggested to evaluate the non-linear hysteretic damping produced by the macro-element model. In linear analyses, both free decay tests (time domain) and the Q-factor method (frequency domain) are suitable to evaluate the damping contribution on the dynamic response. In a non-linear system, however, these methods are not always adequate for estimating the load-dependent damping contribution.

Therefore, this chapter first elaborates on two preferred methods for damping estimation in linear dynamics. Next, the consequences of a non-linear system on the applicability of these methods is qualitatively explained. By performing single and multi-frequency steady state forced vibrations, the validity of the linear damping estimation techniques is quantified. The results are placed in perspective with previous studies, that use the linear methods to estimate the damping of offshore wind turbines.

5.2 Linear Damping Estimation for Non-Linear Systems

By including a hysteretic model to the otherwise linear system, the total system responds non-linear to the environmental loads, as both the damping and the stiffness estimation become non-linear. This section evaluates two typical damping estimation methods. These

methods are valid for linear systems, however, in non-linear systems these methods may give an inaccurate damping estimation. The first part elaborates on the two damping estimation methods and the second part discusses the effect of the non-linearity on the application of these methods.

System Damping Estimation Methods for Linear Systems

In a linear system, the damping can be estimated using the quality (Q) factor method (frequency domain) or the logarithmic decrement method (time domain). Fundamentally, these methods are merely valid for linear systems, however, some authors use the Q factor method or logarithmic decrement method to estimate the damping of a (partial) non-linear system (e.g. [38, 82, 85]).

The Q factor method uses the power spectrum density (PSD) of the response to estimate the damping. In a linear system, the response of the OWT in a PSD is centred around the (first) natural frequency. The Q factor is consequently determined from the frequencies where the amplitude of the response is reduced to half of its maximum (at $f = f_n$). The ratio of critical damping, ξ, may be obtained from Q.

Besides using frequency domain results, the damping may also be found from time domain free vibration analyses using the logarithmic decrement (log. dec.) method. In a free decay test, the response will damp out over time and to the maxima of the free vibration, a logarithmic decrement may be fitted, as mathematically shown by Equation 5.1.

$$u(t) = A\, e^{-\xi\omega t} \tag{5.1}$$

With u the displacement, but this may be any variable of the vibrating response (e.g. $\dot{u}$, M, H). A is the amplitude of the first cycle, ω the radial frequency and t the time. The damping ratio determines how quickly the system damps out and can be numerically obtained from the logarithmic decrement, δ. With δ and the relation between δ and ξ as determined by Equation 5.2. The approximation is only valid for low values of critical damping.

$$\delta = \ln\left(\frac{A_i}{A_{i+1}}\right) = 2\pi\frac{\xi}{\sqrt{1-\xi^2}} \approx 2\pi\xi \tag{5.2}$$

For additional information regarding the damping estimation methods for OWTs, reference is made to e.g. Versteijlen et al. [85].

Consequences of Non-Linearity

To estimate the damping in a non-linear system, however, both the log. dec. and Q-factor method are unfit to evaluate the damping. In a non-linear system, like the OWT structural model with a non-linear foundation model, the frequency of the response is dependent on the load-dependent stiffness and damping. Thus, the division of energy in the power density spectrum is spread around the initial (i.e. non-degraded) resonant frequency of the OWT. The PSD depicts how the energy is on average divided in the frequency domain and so does not represents the dependence on excitation amplitude [86]. As in a non-linear system the fundamental frequency of the response is not limited to one frequency, due to softening or hardening the instantaneous natural frequency is dependent on the amplitude of the load level. Therefore, it is recommended not to use the frequency domain to obtain system properties (i.e. natural frequency, damping).

As the stiffness of the response is dependent on the load level, the amplitude of the response also behaves non-linear, this may be observed in TD analyses. Thus, it is not possible to fit a log. dec. (Equation 5.1) to the time series, like in a linear system. Katsikogiannis et al. [38] attempt to account for the amplitude dependency of the response in the application of the log. dec. method. However Katsikogiannis et al. [38] do not acknowledge that the phase of the response also changes in a non-linear system, due to a shift of the free vibration frequency. This poses another limitation to the log. dec. method.

The above is shortly illustrated, based on multi-frequency steady state forced vibrations in a non-linear system. Equation 5.3 depicts the particular solution for a system that is excited by a harmonic force of similar nature (e.g. $F_{ext,1,2} = F_{1,2}\sin(\omega_{1,2}t)$ and $F_{ext,3} = F_1\sin(\omega_1 t) + F_2\sin(\omega_2 t)$).

$$\begin{aligned} u_1(t) &= U_1\sin(\omega_1 t) \\ u_2(t) &= U_2\sin(\omega_2 t) \\ u_3(t) &= u_1(t) + u_2(t) \qquad \text{with } \omega_1 \neq \omega_2 \end{aligned} \tag{5.3}$$

Equation 5.4 depicts how the internal reaction force is obtained for a non-linear system and is part of the EoM. Note, considering this is merely an example, the non-linearity of the system is chosen randomly and may be any type of non-linearity (also in the damping term).

$$F_{int} = k\,u^3 \tag{5.4}$$

Inserting Equation 5.3 in 5.4 gives Equation 5.5:

$$
\begin{aligned}
F_{int,1} &= kU_1^3 \sin^3(\omega_1 t) \\
F_{int,2} &= kU_2^3 \sin^3(\omega_2 t) \\
F_{int,3} &= kU_1^3 \sin^3(\omega_1 t) + 3kU_1^2 U_2 \sin^2(\omega_1 t)\sin(\omega_2 t) \\
&\quad + 3kU_1 U_2^2 \sin(\omega_1 t)\sin^2(\omega_2 t) + kU_2^3 \sin^3(\omega_2 t)
\end{aligned}
\tag{5.5}
$$

From Equation 5.5, the effect of non-linearity on the response of the system is very clear. Besides the two cubic terms, two additional terms appear in the formulation of the internal reaction force, $F_{int,3}$. These terms are known as the 'interference' terms and their magnitude is dependent on the amplitude and frequency spacing of the multi-frequency forced steady-state excitations.

Depending on the type of non-linearity, the interference terms may influence the response of the non-linear system. This, in turn, determines the applicability of linear damping estimation techniques in the time domain for non-linear systems. For a system with a high degree of non-linearity, i.e. a significant difference in instantaneous natural frequency, the interference term is expected to give a considerable contribution in the response. This results in a notable effect on the amplitude and phase of the response when compared to the response from a linear system, resulting in the inapplicability of the logarithmic decrement method to estimate the damping. The next section evaluates the contribution of the interference term in an OWT model using multi-frequency excitation forced steady state vibration analyses.

5.3 Multi-Frequency Excitation Vibration Analyses

To assess the magnitude of this so-called 'interference' term, multiple multi-frequency excitation forced steady-state vibration analyses are performed. The objective is to quantify the interference term, by comparing the total response at mudline of two single-frequency excitation forced vibrations in the steady state with the response of the multi-frequency excitation steady state vibrations of the same system.

First, to visualise the degree of non-linearity of the system, the phase portrait of the response at mudline to a forced vibration in the natural frequency of the non-linear system is depicted for three different amplitudes of the excitation force. The phase portrait is a way to qualitatively show the solution to a second order differential equation. For a linear system, the phase portrait resembles an ellipse and the shape changes, dependent on the degree of non-linearity of the stiffness and/or damping [87]. Figure 5.1 portrays the phase portraits at mudline of the structural model with the MEM1 foundation model, excited by a single-frequency steady state harmonic force ($F_{exct} = F_{ampl}\sin(\omega_0 t)$) in the first resonance frequency (Table 4.1).

Naturally, the resonance frequency shifts, due to non-linear behaviour of the total system and therefore the system is excited in a frequency very close to f_0. Thus, from Figure 5.1 it may be deduced that for low amplitudes of the harmonic loading, the system behaves almost linearly, while the non-linearity increases with F_{ampl}.

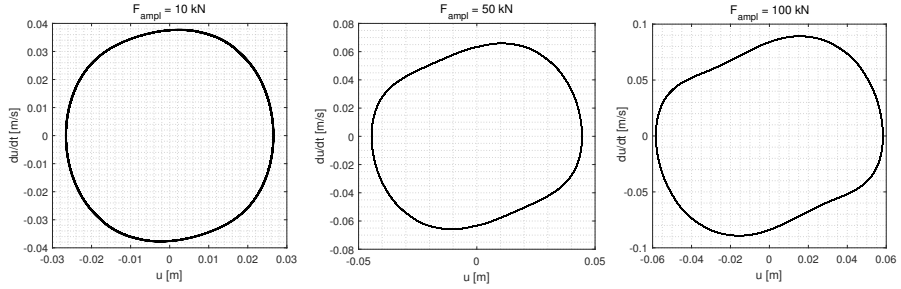

Figure 5.1: Phase portrait of the response at mudline for a structural model with macro-element foundation model (MEM1), for excitation amplitudes F_{ampl} = 10 kN, 50kN and 100 kN in the first natural frequency (f_0 = 0.2361 Hz).

Method

To perform multi-frequency excitation analyses, a harmonic force is applied at the tower top, for the full length of the time series. The combination of amplitude and frequency for the single and multi-frequency excitations are given by Table 5.1. The legend is included for interpretation of the results in Figure 5.3. Note, the results only show the steady-state response, so the transient part is cut.

Table 5.1: Overview of multi-frequency excitation steady state forced vibrations analyses. The legend is in correspondence with the legend of Figure 5.3.

Foundation Model	F_{ampl} [N]	$f_{a,b}$	Legend	$f_{a,b}$	Legend
MEM1	1e4	0.95 f_0 / f_0	◆	0.975 f_0 / f_0	◆
	5e4		●		●
	1e5		■		■
MEM2	1e4		◆		◆
	5e4		●		●
	1e5		■		■

Time Domain Response

Figure 5.2 depicts the steady state response of the deflection at mudline for an excitation with f_0 and $0.95f_0$, accounting for softening of the soil-foundation stiffness. The difference between Figure 5.2a and 5.2b is in the amplitude of the excitation. The difference in the response for the summation of the single frequency excitations and the multi-frequency excitations is negligible for Figure 5.2a. However, in Figure 5.2b a phase shift and change of magnitude of the response is observed. The differences in the response are due to the non-linearity of the system, that causes a reduction of the free vibration frequency of the support structure. As Figure 5.2a responds similar to the single frequency excitation system, the instantaneous natural frequency is (almost) equal to f_0. Hence, this motion dominates the response as the amplitude of the response is much larger than for the excitation with $0.95f_0$. For Figure 5.2b, on the other hand, the instantaneous natural frequency lies more in between 0.95 f_0 and f_0 and thus the response is dependent on both excitation frequencies. Note, the moment at mudline corresponding to these displacements is approximately 450 MNm, which is comparable to the maximum loads at the selected site. Thus the effect of the interference term is assessed for cases where F_{ampl} = 1e5 N.

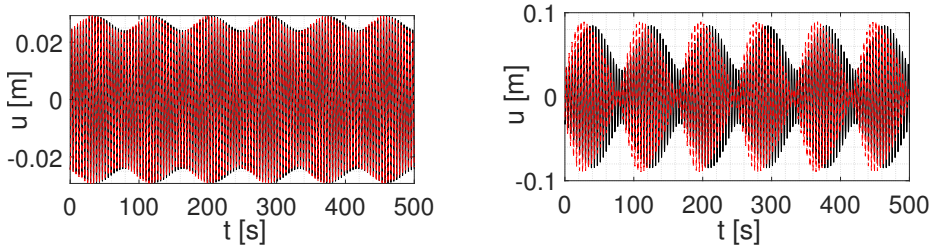

(a) F_{ampl} = 1e4 N; $f_a = 0.95f_0$; $f_b = f_0$ **(b)** F_{ampl} = 1e5 N; $f_a = 0.95f_0$; $f_b = f_0$

Figure 5.2: Steady state response at mudline to forced vibration for summation of single frequency excitations (——) and multi-frequency excitation (- - -) for different amplitudes of the excitation force, $F_{exct,1} = F_{ampl}\sin(2\pi f_a t)$. Harmonic force excited at the tower top of a linear support structure with MEM1 foundation model.

Considering that the phase shift is essential in determining to what extend the log. dec. damping estimation method is applicable for the (weakly) non-linear system, the phase lead of the non-linear system is evaluated for the analyses as presented in Table 5.1. Further, as the soil layering determines the degree of non-linearity of the foundation model, the steady state vibrations are run with MEM1 and MEM2 (non-linear stiffness and damping) and for one API p-y curve case (non-linear stiffness).

Phase Difference of the Response at Mudline

To visualise the consequences of a non-linear system at mudline, the phase of the multi-frequency excitation forced vibration with respect to the summation of the single frequency excitations is plotted versus the maximum moment at mudline of the forced vibration. The phase difference is defined as the difference between the maxima of the two vibrations. Figure 5.3 depicts the phase difference versus the maximum moment at mudline for steady state forced vibrations with varying amplitude and frequency for MEM1 and MEM2. The amplitude difference is not included here, as from Figure 5.2 suggests that the phase difference caused by the interference term is more significant than the amplitude difference. For an overview of the run analyses, reference is made to Table 5.1. In addition, note that all time domain results are included in Appendix D.

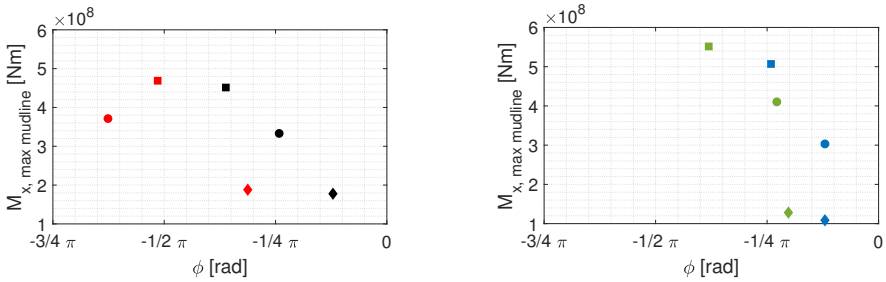

(a) Foundation model MEM1 **(b)** Foundation model MEM2

Figure 5.3: Phase difference for multi-frequency excitation versus the summation of two single frequency excitation vibrations. The symbols correspond to the analyses as included in Table 5.1.

Macro-Element Model Calibrated against API *p-y* Curves

Figure 5.3a confirms the expectations, on the effect of non-linearity on the influence of the interference terms. Generally, the theory holds that the higher the degree of non-linearity (i.e. larger F_{ampl}), the larger the phase difference. For the MEM1 foundation model one data point does not follow the expected behaviour (F_{ampl} = 100 kN and $f_{a,b}$ = 0.975 f_0, f_0), as the phase difference decreases with respect to the previous point (F_{ampl} = 50 kN). It is found that the phase difference, that is defined as the difference between the summation of the single-frequency excitation vibrations and the multi-frequency excitation vibrations, is lower as the response of the smaller frequency becomes dominant. The shift in maximum of

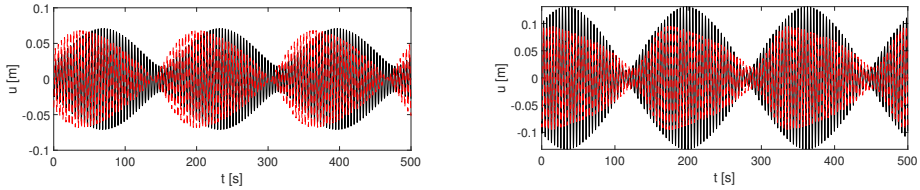

(a) F_{ampl} = 5e4 N; f_a = 0.975f_0; f_b = f_0 **(b)** F_{ampl} = 1e5 N; f_a = 0.975f_0; f_b = f_0

Figure 5.4: Steady state response at mudline to forced vibration for summation of single frequency excitations (——) and multi-frequency excitation (- - -) for different amplitudes of the excitation force, $F_{exct,1} = F_{ampl}\sin(2\pi f_a t)$. Harmonic force excited at the tower top of a linear support structure with MEM1 foundation model.

the summation of single-frequency excitations that is the cause of this, may also be observed by comparing Figure 5.4a and 5.4b.

From Figure 5.4a and 5.4b it may also be deduced that in this case, the contribution of the interference term on the amplitude of the response becomes more significant than in the other cases (e.g. 5.2). The multi-frequency excitation vibration is more distorted, while the summation of single frequency excitation remains harmonic. This may be explained in the following way: the non-linear stiffness (and damping) result in a decrease of the free vibration frequency, with respect to the natural frequency using a linear elastic stiffness matrix. This results in a larger contribution to the response of nearby frequencies (like 0.975 f_0). Even for the cases where the softened response is governing, like in Figure 5.4b, the summation of single frequency excitations is sinusoidal. The response of the multi-frequency excitation is more distorted, as even in the steady state the free vibration frequency changes continuously with load level. For a small amplitude of the excitation force (forces are out of phase), the response at the lower frequency is almost negligible in comparison to the response of at f_0. So, after a through in the excitation the response at f_0 dominates. While the excitation force is increasing, the free vibration frequency changes, resulting in a larger contribution of 0.975 f_0 to the total response.

Besides assessing the effect of the interference term on the closely spaced frequencies, the effect is additionally verified for the response at f_0 and f_1 using the MEM1 foundation model. Figure 5.5 depicts the phase portrait to the single frequency excitation in the second mode (left) as well as the mudline response for the summation of single frequency excitations and the multi-frequency excitation (right). For the maximum excitation amplitude as analysed in this thesis, the second mode responds linear to the excitation, while the first mode responds non-linear (right plot of Figure 5.1). The interference term predominantly affects

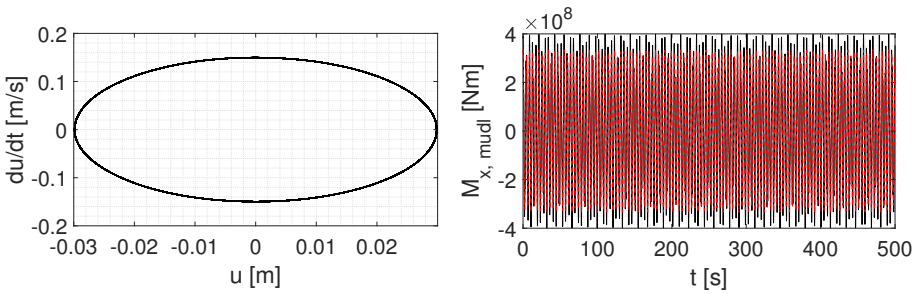

Figure 5.5: Left: phase portrait of the response at mudline for a structural model with MEM1 foundation model. F_{ampl} = 100 kN and $f = f_1$ = 0.7976 Hz. Right: steady state response at mudline to forced vibration for the summation of the single frequency excitations (——) and multi-frequency excitation (- - -) for F_{ampl} = 100 kN and f_a = 0.2361 Hz and $f_b = f_0$ = 0.7976 Hz.

the amplitude of the response and does not seem to cause a phase difference between the single frequency and multi-frequency excitations.

Macro-Element Model Calibrated against 3D FEA with HSsmall Model

The phase difference for the support structure with the MEM2 foundation model is, for the same load amplitude, lower when compared to response of the MEM1 model. Further, when comparing Figure 5.3a and 5.3b, it is interesting to note that the phase difference seems to follow the same trend for each foundation model. This only holds for simulations where the response of the undamped first eigenfrequency is dominant. Further, it is noteworthy that the development of the phase difference (trend) is different for the two hysteretic models. In addition, from the time domain analyses, it is observed that the effect of the interference term on the amplitude becomes more significant. Please note, this difference in amplitude of the response becomes negligible when the moment at mudline is compared.

API *p-y* curves

The macro-element model accounts for both nonlinear stiffness and damping, while the API pre-defined functions only account for non-linear stiffness. To evaluate the effect of non-linear stiffness, one analyses is run with the API *p-y* curves as the foundation model. The results at mudline are compared with the results at mudline as obtained with the macro-element models. The left plot of figure 5.6 shows the phase portrait of this model to a single

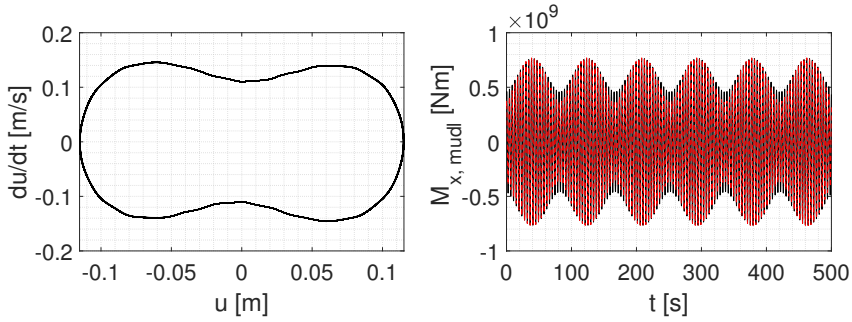

Figure 5.6: Left: phase portrait of the response at mudline for a structural model with API *p-y* curves as foundation model. F_{ampl} = 100 kN and $f = f_0$ = 0.2361 Hz. Right: steady state response at mudline to forced vibration for the summation of single frequency excitations (——) and multi-frequency excitation (- - -) for F_{ampl} = 100 kN and f_a = 0.2243 Hz and $f_b = f_0$ = 0.2361 Hz.

frequency excitation in the first natural frequency (f_0). The offshore wind turbine is excited by an external harmonic force with an amplitude of 100 kN. The phase portrait is no longer ellipse-shaped, and thus displays non-linear behaviour of the OWT at mudline. Compared to the phase portraits of Figure 5.1 the shape differs significantly. The phase plane of the API *p-y* curves shows the effect of non-linear stiffness (Duffing oscillator), while the phase portraits obtained with the MEM1 model resemble more the phase portrait of the Van der Pol oscillator (i.e. non-linear damping).

The right plot of Figure 5.6 depicts the response at mudline for the summation of single frequency excitations and the multi-frequency excited non-linear response (M_x). The moment at mudline (M_x) is shown, so the response may be compared with the results of Figure 5.3. No discrepancy is observed with respect to the phase of the two vibrations. Additionally, for the predominant part of the time domain simulation, the amplitude of the response agrees well. At the 'troughs' of the vibrations, the response from the summation of the single frequency excitations is slightly larger. This is due to the larger degree of non-linearity (i.e. hardening of the soil) in the multi-frequency steady state vibration, which causes a larger decay of the natural frequency. Therefore, the response of the 0.95 f_0 excitation has a larger influence on the response.

Impact on the Response at Tower Top

Besides the response at mudline, also the response at interface level and tower top is evaluated, as the system damping and the soil damping contribution is usually evaluated from tower top (e.g. [85, 82]). From the time series of the deflection, it is observed that the interference term does not change along the height of the support structure. So, the phase difference as seen at mudline (Figure 5.3) does not change for the response at interface level or at tower top. This is coherent, when taking into account that the macro-element model is the boundary condition of the support structure. As all the elements above the macro-element model behave linear, the support structure follows the displacements of the boundary condition and thus the impact of the interference term remains unchanged.

However, when evaluating the phase portrait of the response at tower top, the response resembles a linear system (i.e. depict an ellipse shaped phase portrait). This is illustrated by Figure 5.7 that presents the deflection and velocity, normalised to the maximum, at three different heights along the support structure. The deflection, for MEM1, results in sinusoidal behaviour at the three locations. The velocity, on the other hand, shows an increased sinusoidal response at tower top, when compared to the mudline velocities.

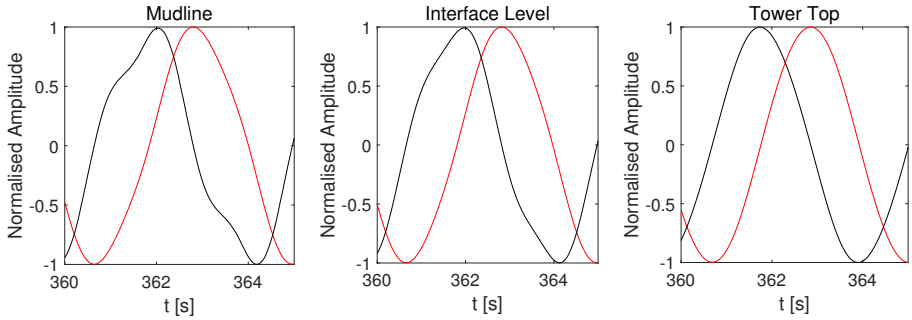

Figure 5.7: Normalised deflection (——) and velocity (——) at mudline, interface level and tower top for multi-frequency excitation with f_a = 0.975 f_0, f_b = f_0 and F_{ampl} = 5e4 N using the MEM1 foundation model.

To explain the differences in the response, the response at the three locations is compared in the frequency domain. Here, it is observed that the amplitude at the second resonant frequency with respect to the amplitude at the first resonant frequency decreases over the height of the support structure. Therefore, it is postulated that the difference in the phase portraits (time series of $\dot{u}$ and u) is due to the presence of response in the second mode. To check this, response of an OWT with a macro-element model foundation is compared

with the response of an OWT supported by a linear elastic foundation model, when they are excited by the same multi-frequency vibration. The results of the linear analysis are consistent with the results of the non-linear analysis, regarding the ratio between the peaks at f_0 and f_1 along the height of the support structure. This indicates that this effect is caused by the differences in modal amplitudes at mudline, interface level and tower top. However, the response in the second mode for the system with a linear elastic stiffness matrix at mudline is almost negligible, while the response is significant for the OWT supported by the non-linear hysteretic macro-element model. Therefore, it is proposed that the effect of the mode shapes on the response ($\dot{u}$) is amplified by the non-linearity of the system.

5.4 Discussion

The current study assesses the response of the OWT at mudline to a multi-frequency excitation forced vibration and compares it to the response of two single frequency excitations. It is determined that the interference term results in a phase difference in the steady-state response, when compared to the summation of the two single frequency excitations. The results indicate that the effect of non-linear damping accounted for by the macro-element model is the main cause of the phase difference caused by the interference term. However, before any conclusions can be made with regards to the applicability of the log. dec. method in the non-linear system (being the OWT with non-linear SSI) the limitations on the current study need to be discussed.

The main limitation of the research is due to the minimal number, i.e. two, of combined excitation frequencies. The effect on the results is that response at the non-degraded eigenfrequency is dominant. Therefore, the effect of a shift of the eigenfrequency is more dominant in the response of the multi-frequency excitation. Thus, the phase difference is more apparent in a comparison. For a situation where the degraded eigenfrequency is the dominant response in the single-frequency analyses, the phase difference becomes smaller, indicating that the response of the summation of the single frequency and the multi-frequency excitation agree to a higher degree (smaller interference term). Therefore, before any conclusions may be made on the validity of the log. dec. method to determine the system damping estimation, the same analysis should be performed for a spectrum of frequencies.

Besides a limitation of the analyses of solely including two excitation frequencies, the analysis is simplified with respect to loading direction. All steady state forced vibrations are excited in the F-A direction. In reality, part of the response is in the S-S direction and hence the effect of non-linearity (i.e. interference term), should be assessed for multi-directional loading. This is particularly interesting as the eigenfrequencies of the S-S motion of the OWT are very close to the eigenfrequencies of the F-A motion.

Other interesting results concern the phase differences of the multi-frequency excitation with respect to the summation of the single frequency excitation for the two macro-element models (MEM1 and MEM2). As the sole variation in the model set-up are the calibration curves for the macro-element model, the differences in the response may be attributed to the distinct curves. Figure 4.3 depicts the calibration curves for the MEM1 and MEM2 model. The response of the MEM1 model is softer, but seems more linear, when compared to the MEM2 model. Thus, it is postulated that the difference in the interference term from the analyses with the MEM1 and MEM2 model may be attributed to the effect of the non-linear stiffness and consequent hysteretic damping on the response. To verify this, it is recommended to perform more analyses with a non-linear elastic foundation model, like the Winkler model supported by *p-y* curves.

5.5 Summary

In a linear system the damping may be estimated from the frequency or time domain, with the Q factor or log. dec. method, respectively. In non-linear systems these strategies may not provide accurate estimations of the system damping anymore, as the resonant frequency is load-dependent. Still, linear damping estimation techniques, like the log. dec. method are applied for system damping estimation of OWTs. By doing this, the phase and amplitude difference caused by the non-linear soil reaction are not accounted for, which may result in inaccurate damping estimates.

The impact of the interference term, that causes the phase and amplitude difference in the non-linear system is evaluated with multi-frequency excitation steady state forced vibrations. By comparing the response at mudline to this excitation with the response of a summation of single frequency excitations, the interference term may be quantified. The non-linear hysteretic macro-element model calibrated to the API pre-defined functions and 3D FEA shows that the effect of the phase difference is larger for a larger excitation amplitude. For a foundation model that solely accounts for non-linear stiffness (API *p-y* curves), the amplitude of the deflection at mudline is affected. This amplitude change is no longer observed if the moment at mudline is compared for the summation of single frequency excitation and the multi-frequency excitation.

Chapter 6

Conclusion and Recommendations

6.1 Conclusion

The objective of this master thesis is to *qualify the impact of accounting for the non-linear hysteretic behaviour of soil in integrated analyses on the support structure design of monopile-based offshore wind turbines in ultimate limit state conditions*. To meet this objective, the scope of work is divided into three parts: 1) to compare the macro-element and 3D finite element model response for ultimate limit state conditions and 2) to evaluate the effect of foundation modelling on the dynamic response of the OWT when exposed to extreme loads and 3) to investigate the validity of linear damping estimation strategies for a non-linear system. First, the main conclusion on using the macro-element model in integrated analyses is outlined. Next, more in-depth recapitulations of the conclusions drawn from each part of the work are given.

Main Conclusion The macro-element model has proven to be a computational efficient foundation model for application in integrated analyses of offshore wind turbines. The hysteretic behaviour that is accounted for by the macro-element model positively affects the magnitude of the response along the height of the support structure, specifically in idling conditions as in this case the aerodynamic damping is negligible. The macro-element model is especially suitable to be included in load-calculation software that typically makes use of super-elements. Until recently, the macro-element model has predominantly been promoted

for application in fatigue limit state analyses. However, the results of this thesis show that the macro-element model is able to sufficiently capture the soil-structure interaction when exposed to extreme loading (ultimate limit state).

Comparison of the Macro-Element Model with 3D FEA

Chapter 3 contains the result of the comparative study of which the objective was to identify potential model limitations. Generally, the response of the 3D FEA with the UDSM *VonMisesSeriesCoupled* is adequately captured by the macro-element model, for varying geotechnical and extreme loading conditions. Some limitations of the macro-element model have been observed in the comparative analyses. In planar and multi-directional conditions the macro-element model may underestimate the soil-foundation stiffness when exposed to extreme load levels. Typically, an underestimation of the stiffness is acceptable, as this results in a conservative approach in design analyses. As the estimation of the load-dependent stiffness and damping is coupled in the macro-element model, a significant underestimation of the soil-foundation stiffness may cause an overestimation of the hysteretic damping contribution. This, in turn, results in an incorrect modelling of the SSI. It should be noted though, that part of the discrepancy between the macro-element model and the 3D finite element-UDSM case may be attributed to the gap opening that is included in the FEA.

Case Study

Following, *Chapter 4* presents the results of the case study, where an OWT for the selected site is exposed to the governing DLC. The impact of foundation modelling on the dynamic response is evaluated by including three foundation models in time domain analyses: 1) the current industry standard based on non-linear elastic API *p-y* curves [22] and 2) the non-linear elasto-plastic macro-element model calibrated against the API *p-y* curves (MEM1) and also load-displacement curves from 3D FEA with the HSsmall model (MEM2). From the foundation models calibrated to the API *p-y* curves it is observed that the hysteretic behaviour of the macro-element model mainly positively affects the magnitude of the response at the resonant frequencies. This is deduced from the power spectral densities of the response at mudline and interface level, where the resonant peaks are lower for the model that uses the macro-element foundation model (MEM1).

Besides evaluating the impact of the hysteretic behaviour, also the effect of calibration against 3D FEA instead of the API *p-y* curves is assessed. The stiffer (initial) behaviour that results from 3D FEA affects the prediction of the eigenfrequencies of the structure, something that is also deduced from the PSD of the response at mudline and interface level. Besides a different

estimate of the resonant frequencies, the maximum response of the support structure with the MEM2 foundation model is lower than for the same support structure with model MEM1. Moreover, the decrease of amplitude at the resonant frequencies is larger for the second comparison, where the effect of the calibration strategy is assessed. This emphasises the limitations of the API *p-y* curves in accurately describing the SSI of piles with increased rigidity.

It should be noted that the response of the foundation models is merely assessed in an idling case, where the aerodynamic damping is negligible. In an operating case, the effect of the hysteretic model on the response at the resonant frequencies will be lower, as the total response at the first (dominant) eigenmode is significantly damped by aerodynamic damping (e.g. [38]). For the foundation models calibrated against the API *p-y* curves no impact is observed of the foundation modelling in the range of the environmental excitation frequencies. Thus, the impact of the foundation model on the dynamic response in operating cases is reduced, when compared to idling cases. For the macro-element models calibrated against different backbone curves, there is an additional effect of the response in the frequency range below the first resonant frequency. Thus, the impact of a different calibration strategy is larger than accounting for hysteretic behaviour. This is acknowledged by DNV-GL, that recommends the use of FEA for foundation piles with $D > 1.0$ m [1]. Considering that calibrating the macro-element model against 3D FEA is more straightforward than extracting *p-y* formulations from FEA the application of the macro-element model might be favoured in load calculation or detailed design analyses.

Linear Damping Estimation Strategies for Non-Linear Systems

Chapter 5 focuses on the validity of the linear damping estimation strategy in the time domain for the non-linear system, being the OWT with non-linear SSI. Using multi-frequency steady state excitations, the interference term is obtained by comparing the response to that of a summation single frequency excitations. It is found that the impact of the interference term on the response (amplitude and phase) increases for an increase in load amplitude. This is conform expectations, as the increase in load amplitude results in more softening of the soil and consequently larger shift of the free vibration frequency.

The multi-frequency excitation vibrations are performed with three foundation models: 1) the macro-element model calibrated against API $p-y$ curves (MEM1) and 2) the macro-element model calibrated against 3D FEA with the HSsmall constitutive model (MEM2) and 3) a Winkler model supported by API $p-y$ curves. From the performed analyses, it is observed that the impact of the interference term on the response largely depends on the foundation model. The calibration curves for the MEM1 and MEM2 model differ, not only in the initial stiffness, but also in the degree of hardening of the soil-foundation stiffness (i.e.

non-linearity). The MEM2 model, even though it has a larger tangent stiffness for all points along the calibration curve (Figure 4.3), experiences more hardening behaviour. Thus, the differences in the interference term are attributed to the varying soil-foundation response. Additionally, from comparing the response from the models calibrated against the API *p-y* curves it is shown that the hysteretic behaviour also affects the interference term.

To conclude, from the results of the multi-frequency excitation vibrations, the applicability of the logarithmic decrement method for damping estimation is questioned, as the interference term does result in a phase and amplitude difference. The impact of the interference terms on the deflection amplitude is dominant, while the effect on the shear force and moment is almost negligible.

6.2 Recommendations

The recommendations for further work may be divided in two parts: 1) proposals regarding the further development of the macro-element model and 2) suggestions for numerical analyses of an offshore wind turbine supported by a macro-element foundation model. Note, the recommendations that correspond to category 1) are an addition to the recommendations that are proposed by Page [32].

- Currently, the macro-element formulations are based on a total stress model, which implies that no distinction is made in total and effective stresses. This predominantly influences the yield criterion formulation (contours of plastic work). In this work, the total stress model is used to model the load-displacement relation of a (partial) non-cohesive soil. To verify this assumption it is suggested to perform FEA in a non-cohesive soil, to verify that the contours of plastic work are also ellipse-shaped and may be assumed to be homothetic to each other. Page (private communication) performed some initial FEA that indicate that the distribution of yield surfaces is also homothetic for effective stress analyses. In addition, it is proposed to include a parameter that accounts for the pore pressure. This parameter may also be used to implement a drainage formulation.
- The macro-element model does not account for non-consecutive yield surfaces being active. For the performed analyses, it is assumed that this does not affect the response of the macro-element model to the severe environmental loads. However, for other cases (e.g. fault cases) this may result in too stiff initial soil-foundation behaviour. Therefore, it is suggested to include the binary solution method, that was proposed and implemented by Grimstad (private communication) in the the user-defined soil model *VonMisesSeriesCoupled*. This solution strategy allows for non-consecutive yield surfaces to be active and is more computational efficient than checking all yield

surface combinations (faculty). It is expected that including this solution strategy will also increase the robustness of the foundation model.

The recommendations for further research on the use of the macro-element model in numerical analyses are outlined in the next section.

- The study that evaluates the effect of the interference term on the dynamic response of the offshore wind turbine is very limited, as it accounts for only two frequencies. Therefore, it is recommended to perform additional analyses that account for an increased number of frequencies or a spectrum of frequencies. The response spectrum may be obtained from exposing the OWT to a 10-minute time domain ULS load case, that activates the soil non-linearity. As the effect of the interference term is determined from the differences in the particular solution to the inhomogeneous equation of motion from a single and multi-frequency excitation, the excited vibrations need to result in a steady state response of the OWT. It is expected that the phase difference, the way that is determined in Chapter 5, decreases when the response is compared to that of a spectrum. Instead, it is expected that the distortion of the signal (e.g. Figure 5.4b) becomes more important.
- To evaluate the system damping of the OWT supported by a macro-element model, it is suggested to determine the damping from an analysis that considers the balance of energy. The potential energy can be determined at mudline, provided that the elasto-plastic stiffness is known (see Appendix E). Further, the dissipated energy may be determined by taking the integral to a multiplication of F and $\dot{u}$ in the time domain. The damping factor may compared to equivalent linear damping obtained from a logarithmic decrement at tower top. In case the discrepancy between the two methods is negligible, it may be concluded that the linear damping estimation strategy is sufficient. Otherwise, the system damping could be estimated from a free decay test with a Hilbert transformation (e.g. [88]).
- The initial analyses as performed in Chapter 5 indicate there is a dependency on the degree of non-linearity on the interference term. Additionally, the foundation model, being the macro-element model or Winkler model supported by p-y curves, also seems to determine the impact of the interference term on the response. Therefore, it is suggested to perform the above two analyses with varying foundation models to determine the contribution of non-linear stiffness, damping and effect of degree of non-linearity.
- The macro-element model was initially developed for application in FLS analyses. Generally, the soil-structure interaction in the fatigue limit state is assumed to be linear elastic, thus not accounting for hysteretic behaviour of soil. As the macro-element model may capture accurately the mudline response, it is suggested to evaluate the

assumption of linear elastic soil-foundation behaviour in the fatigue limit state. This might be especially interesting for monopiles with varying L/D.

- For implementation of the macro-element model in load-calculation software, it is advised to perform a study regarding the computational efficiency of the iterative algorithm. Currently, a modified Newton-Raphson algorithm is used, that uses the initial stiffness for the iterations. For FLS analyses, where displacements are generally low and closer to the initial displacements, this verification scheme is expected to be more computational efficient. However, for extreme load analyses, it may be more computational efficient to use a regular Newton-Raphson scheme. In this case, the macro-element model requires an update, so it also gives the elasto-plastic stiffness matrix as an output. The formulation of the elasto-plastic stiffness matrix is included in Appendix E.
- This thesis did not focus on using the macro-element model in foundation design, as in this case also the response along the embedded part of the monopile is required. For foundation design Page et al. [37] propose to use a post-processing tool, that consists of a 1D monopile model supported by API/FEA *p-y* curves. To evaluate the applicability of the macro-element model combined with the post-processing tool in design analyses, it is recommended to compare the moment distribution resulting from this analyses with the response obtained with 3D FEA for varying geotechnical and loading cases.

Appendix A

Overview of Macro-Element Models

As part of the literature review, a variety of macro-element models is examined, that are developed for different purposes and within different frameworks. Table A.1 to A.12 include an overview of the macro-element models that are discussed in the project thesis [41]. Please note, Table A.1 to A.12 mainly present a summary of the read papers and include limited comments of the author.

Table A.1: Overview of *Settlements of foundation in sand* by Nova and Montrasio [34] that present a 3DoF (planar) macro-element model within the elasto-plasticity (linearised strain hardening theory) framework.

Assumptions	**Input to model**	**Model Calibration**
1) Soil is homogeneous over depth and there is no shallow bedrock present. The latter merely influences the vertical displacements and not the lateral displacements, which are the main concern for OWTs. 2) Only rigid body predictions are made	1) Yield criterion derived from experimental data 2) Non-associative flow rule, with plastic potential that is based on the expression of the yield criterion 3) Strain hardening loading function, hardening for plastic strains in V, H and M direction.	The macro-element model is calibrated with 9 constants, that can be obtained from laboratory tests.
Loads	**Validation**	**Conclusion**
A combination of varying V & H loading and V, H & M loading are studied, monotonically and two tests where the load is reversed.	The response of the macro-element model is compared with a plane strain test on uniform sand.	The model correctly captures non-linearity, irreversibility upon unloading and coupling of the displacements and rotation.
Limitations	**Application range**	**Suggestions further research**
1) Under unloading-reloading elastic behaviour is not accounted for, only irreversibility of strains upon unloading.	Settlement of shallow strip foundations on sand. Non-linearity is accounted for in the model, but only occurs for large strains. Hence, a linearized model is proposed that can be applied for small load levels. This linearized model captures the coupling between displacement and rotation.	The authors consider their model as not ideal, since there are 9 parameters that need to be found to calibrate the model (more if unloading & reloading is considered).

Table A.2: Overview of *Formulas and charts for impedances of surface and embedded foundations* by Gazetas [35] that presents the use of a 6DoF impedance matrix.

Assumptions	**Input to model**	**Model Calibration**
1) Impedances derived from steady state vibrations 2) Only valid for homogeneous half-spaces	1) Static stiffness matrix 2) Dynamic stiffness coefficient 3) Radiation damping coefficient, that also may account for a hysteretic damping contribution	The impedance matrix is calibrated with information of foundation geometry and soil properties, like Poissons ratio and the shear wave velocity
Loads	**Validation**	**Conclusion**
Harmonic forces in x, y or z direction. A coupling between the forces is allowed.	The response from the impedance matrices is compared with numerical dynamic boundary element solutions	The formulas and charts may be used for foundations with a solid basemat in a homogeneous (elastic) soil. In a multi-layered non-linear analyses, the impedance matrices may be used for interpretation of the results as they may provide adequate estimates of the average deflections.
Limitations	**Application range**	**Suggestions further research**
1) Only for frequency-dependent linear elastic behaviour of soil-foundation interaction 2) For a non-symmetric foundation, external forces may result in activation of cross-coupling modes, that are not accounted for by the derived impedance matrix, as a symmetric foundation is assumed	The formulas and charts may be used for foundations with constant embedment depth and a solid basemat with arbitrary shape.	As the paper is based on encouraging engineeers to use the suggested impedance matrices, no suggestion for further research are defined.

Table A.3: Overview of *A plasticity model for the behaviour of footings on sand under combined loading* by Houlsby and Cassidy [89] that present a 3 DoF (planar) macro-element model within the elasto-plasticity (strain hardening theory) framework

Assumptions	**Input to model**	**Model Calibration**
1) As the model is developed for sand, it should incorporate partially drained behaviour, however, as the loading rate has little effect on the load-deformation response the 'current' model is not adjusted.	1) Empirically defined yield criterion (Martin 1994) 2) Flow rule: associated in M, H plane and non-associated in V, M and V, H plane. Plastic potential is similar to the expression of the yield criterion 4) strain hardening rule, that states hardening occurs only for increase in V	The model is calibrated with experimental tests. The elastic behaviour is determined using stiffness factors from 3D FEA.
Loads	**Validation**	**Conclusion**
Planar monotonic V, M and H loading	The model is validated with the same experimental tests that are used for the calibration.	As the model is calibrated and validated with the same tests, the results are expected to have a good fit. The purpose of the paper is to 1) demonstrate the feasibility of numerical implementation of the model and 2) to assess to what extent the model captures salient features of the original data.
Limitations	**Application range**	**Suggestions further research**
1) The expansion of the yield surface is solely a function of the plastic component of vertical deformation. 2) Unload-reload loops prepeak are modelled well, although the model does not reflect hysteresis that occurs in the experimental results.	The model is developed for shallow foundations, with a focus on vertical loading and has successfully been applied in jack-up analyses in the North Sea. Note, the macro-element is sensitive to vertical loads close to the peak load capacity.	In case a more advanced model is required: the effect of loading rate, degree of drainage, load path reversal and cyclic behaviour may be added.

Table A.4: Overview of *A generalised Winkler model for the behaviour of shallow foundations* by Houlsby et al. [61] that present a 6 DoF macro-element model within the hyperplasticity framework

Assumptions	**Input to model**	**Model Calibration**
1) Under tension the foundation and the soil are separated (contact breaking)	1) Energy function 2) Dissipation function Implicitly, these functions describe the elastic behaviour, yielding and the collection of plastic strains.	The elastic and plastic parameters are calibrated separately, based on analytical solutions and typical values. As the analytical solution may not give an adequate solution, parameters may be function of position under footing, like is done for the elastic stiffness.
Loads	**Validation**	**Conclusion**
Combined cyclic V,M and H loading.	The model is not validated to any experimental tests. However, one vertical load-deflection cycle is validated with an analytical solution.	The model may describe the soil behaviour under cyclic loading, although the model is not validated with any experimental or field data.
Limitations	**Application range**	**Suggestions further research**
1) No coupling effects between H and M taken into account 2) As the model is based on a Winkler foundation, there is no coupling between the elements, so upon integration, there is an inevitable loss of stiffness in rotational and torsional direction.	As the loads are input and the displacements output, the model is not ready to implement in FEA. However, in this case foundation behaviour under high loads, like gapping, can be included. The model is a total stress model and thus for clay dominated soils.	Weakness of the model is that for unloading after large displacements an unrealistic response, large uplift of the foundation, is observed.

Table A.5: Overview of *Investigating 6 DoF loading for shallow foundations on sand* by Bienen et al. [90] that present a 6 DoF macro-element model within the elasto-plasticity (work hardening theory) framework

Assumptions	**Input to model**	**Model Calibration**
1) The shape of the yield surface for different modes of loading is assumed to be the same 2) The normalised load capacity, in H, M and Q plane, does not change with footing penetration	The model is a 6DoF model that is an extension of models as shown by e.g. Houlsby & Cassidy (2002). Hence: 1) Empirically defined yield criterion, using swipe tests 2) Flow rule: associated in M, H planes and non-associated in V, M and V, H planes. Plastic potential is similar to the expression of the yield criterion 3) Work hardening rule, incorporating both radial as vertical plastic movements	The model is calibrated using a series of experimental tests performed by Bienen et al. 2006. The elastic stiffness in all but vertical direction is retrieved via expression of Doherty & Deeks (2003)
Loads	**Validation**	**Conclusion**
Monotonic loading, however loads where the direction changed to out of plane loads, mid-way, are also applied.	The response of the macro-element is compared with experimental data and a good fit is observed.	The model gives a good fit when compared to the experimental data. Although, the model shows too much softening.
Limitations	**Application range**	**Suggestions further research**
1) No cross-coupling between the horizontal and moment planes accounted for 2) The rig that is used in the experimental set-up is not infinitely stiff, so upon changing loading direction the numerical model predictions of load reduction are quicker than observed in the tests.	Offshore application range, where the behaviour is elasto-plastic. As the current model only accounts for monotonic loading, an extension is required for dynamic analyses of OWTs	As the model shows too much softening, more than is observed in the experimental tests, further research is needed on how the radial parameters and the flow rule parameters are calibrated, especially in torsional direction.

Table A.6: Overview of *A hypo-plastic macro-element mode for shallow foundations on sand* by Salciarini and Tamagnini [91] that present a 3 DoF (planar) macro-element model within the hypoplasticity framework

Assumptions	**Input to model**	**Model Calibration**
1) The structure main constitutive equation is assumed. In general, the structure of the 'supporting' constitutive equations is assumed 2) In elasticity, no coupling between the different DoFs	As the model is based on a varying tangent stiffness in a rate equation. The tangent stiffness is defined by 2 constitutive functions, that are dependent on the 1) Generalised load vector 2) Variables accounting for previous loading history 3) Direction of generalised velocity Equations are derived and assumed to find the above.	In order to calibrate the model, 17 material constants need to be known: describing elastic behaviour, failure locus, degree of nonlinearity and plastic flow direction, internal variables. However, calibration with 2D or 3D FEA is also possible.
Loads	**Validation**	**Conclusion**
Monotonic planar loading conditions and cyclic loads on a small scale model.	Validated with experimental model tests.	The model contains similar features as the elasto-plastic model of Nova and Montrasio. The agreement for the monotonic test is good, although a slight overestimation of the foundation rotation at the end of the first stage is found, as well as an overestimation of the final vertical displacement. Ratcheting characteristics are not observed in model response.
Limitations	**Application range**	**Suggestions further research**
1) unable to capture the stabilisation of the load-displacement cycles into an almost reversible behaviour 2) Number of load reversals that can be modelled with the macro-element is limited	Shallow foundations on sand that are exposed to (planar or multi-directional) monotonic and cyclic loading, with a limited (n = 50) number of cycles.	In order to capture the stabilisation of displacement accumulation with a larger amount of cycles, it is proposed to extend the size of the 'elastic nucleus', as the accumulated displacement increases.

Table A.7: Overview of *Modelling the drained response of bucket foundations for OWTs under monotonic and cyclic loading* by Foglia et al. [57] that present a 3 DoF (planar) macro-element model within the elasto-plasticity (bounding surface plasticity) framework

Assumptions	**Input to model**	**Model Calibration**
1) Boundary surface coincides with the yield surface	Model is based on the macro-element of Nova & Montrasio (1991) 1) yield surface from experimental tests 2) plastic potential, non-associated flow rule (from Montrasio), 3) Hardening is modelled using a mapping rule, this also defines magnitude of plastic multiplier	The model is calibrated using a series of experimental tests performed by Foglia et al. 2015
Loads	**Validation**	**Conclusion**
Harmonic moment and horizontal load, while vertical load is kept constant	Model tests, 13 in total, some to calibrate some to validate.	The model can accurately predict displacement paths up to failure of the system and take into account the rate decrease, displacement accumulation with cycles and shrinking of hysteresis loops with cycles.
Limitations	**Application range**	**Suggestions further research**
1) Model does not account for increase of stiffness as n increases 3) Hysteresis loops do not overlap	Bucket foundations for OWTs under general loading, the element can (more accurately) predict the response of the bucket foundation under working loads for OWT applications.	Implement an updating rule for the elastic stiffness, so increase in tangent stiffness with n may be accounted for.

Table A.8: Overview of *A hypoplastic macro-element for single vertical piles in sand subject to three-dimensional loading conditions* by Li et al. [56] that present a 3 DoF (planar) macro-element model within the hypoplasticity framework

Assumptions	**Input to model**	**Model Calibration**
1) Loading surface is homothetic to the failure surface. 2) Associated flow is used to define the macro-element velocity	The model is based on a varying tangent stiffness in a rate equation. This stiffness is defined by 2 constitutive functions that define the incremental linear and non-linear part of the tangent stiffness. These functions are dependent on the 1) Generalised load vector 2) Variables accounting for loading history 3) Dir. of gen. velocity	Two strategies considered: based on 3D FE simulations (optimal) and calibration based on empirical correlations (approximate)
Loads	**Validation**	**Conclusion**
Two cyclic horizontal load tests (one way cyclic loading and two way symmetric cyclic loading).	For monotonic loading conditions coupling was very well for u_x and θ (3D FE calibration). Also good agreement for cyclic loading (N = 20). For the empirical calibration, the results where fair, however, due to an underestimation of the coupling stiffness, u_x and θ at mudline where overestimated.	The macro-element gives good results for a single pile in sand exposed to one way and two way cyclic loading. Especially the coupling between translation and rotational response is captured in monotonic loading conditions.
Limitations	**Application range**	**Suggestions further research**
1) The model is rate independent 2) Using analytical expressions to determine the elastic stiffness matrix, the coupling stiffness K_{hm} is not incorporated accurately. This results in an overestimation of the pile head rotations.	The macro-element is formulated for a single pile embedded in a homogeneous layer. However, for a pile where the active length is embedded in homogeneous soil and the loads are excited at the pile head, the model may also be applied in layered soils.	Expose the model to higher number of cyclic loads, now only the response to N = 40 is found, which is a low number amount of cycles for OWTs. Also, for the empirical calibration method an improved method is required to obtain the elastic coupling stiffness.

Table A.9: Overview of *A New Foundation Model for integrated analyses of MP based OWTs* by Page et al. [46] that present a 3 DoF (planar) macro-element model within the elasto-plasticity framework

Assumptions	**Input to model**	**Model Calibration**
1) Vertical loads and displacements are independent of lateral soil reaction 2) Fixed decoupling point where horizontal rotations are purely elastic. Here, the plastic deformations are merely due to moment loading. 3) The vertical DoF is modelled as uncoupled elastic	1) Decoupling point, at fixed position 2) Elastic stiffness matrix 3) 1D IWAN model describing the elasto-plastic behaviour due to moment loading	1) Coefficients of the elastic stiffness matrix 2) Load-displacement curve at mudline for H=0
Loads	**Validation**	**Conclusion**
Two monotonic tests and two tests that include cyclic M,H loading	Validated with FEA, using the NGI-ADP constitutive model	The macro-element captures the result from FEA quite accurately for load levels corresponding to the fixed decoupling point. For larger load levels, the agreement weakens.
Limitations	**Application range**	**Suggestions further research**
1) In reality, there is no constant decoupling point, as it will increase for high load levels	Approximately constant load levels. For a significant variation in load level the agreement between macro-element and FEA is not very accurate anymore, because decoupling point is fixed.	1) More analyses are required for specific foundation dimensions and soil types at relevant load levels, to evaluate the impact of the fixed decoupling point

Table A.10: Overview of *A macro-element foundation model for monopile based offshore wind turbines* by Page et al. [40] that present a 3 DoF (planar) macro-element model within the elasto-plasticity framework

Assumptions	**Input to model**	**Model Calibration**
1) Yield surfaces are homothetic to each other, which might not be true for all load and soil combinations 2) Soil strength and stiffness are independent of frequency 3) The vertical DoF is modelled as uncoupled elastic	1) Yield criterion from plastic work contours. Transformation matrix is applied to scale the yield surfaces to a single load invariant. 2) Assoc. flow rule (from plastic work vectors). 3) Pure kinematic hardening based on Ziegler's translation rule. Koiter rule is applied to add the plastic deformations of each surface	1) Coefficients of the elastic stiffness matrix 2) Load-displacement curves from non-linear analyses
Loads	**Validation**	**Conclusion**
Monotonic and irregular cyclic loads in H and M	The model is validated with FEA and field tests from the PISA project (the latter focuses on monotonic loading, although one unload-reload loop is included)	The macro-element model captures the NL hysteretic response for pile foundations with a varying L/D. Agreement between FEA and macro-element model is very good. From field tests, generally a good agreement is found, especially in the loading-unloading stiffness
Limitations	**Application range**	**Suggestions further research**
1) H,M coupling only in planar conditions 2) Effect of vertical load on lateral response not explicitly accounted for 3) Kinematic hardening adhering to Masing behaviour 4) Rate and frequency independent model	The application is for piles with varying L/D, exposed to low load levels. For higher load levels (not presented here) the assumption of homothetic yield surfaces may influence the results. The application of the macro-element is predominantly for FLS analyses, for piles where length and diameter are set.	1) Include non-homothetic yield surfaces in the macro-element formulation and assess the effects on the response. 2) A multi-directional macro-element that accounts for coupling in the two planes. 3) If required, a coupling with the vertical load may be included.

Table A.11: Overview of *A macro-element for integrated time domain analyses representing bucket foundations for OWTs* by Skau et al. [33] that present a 3 DoF (planar) macro-element model within the elasto-plasticity framework

Assumptions	**Input to model**	**Model Calibration**
1) The potential surfaces are formulated as elliptic surfaces, as is an approximation to the plastic work contours as generated with FEA 2) The model is based on a decoupling point, which varies with load level. However, it is chosen to fix the distance to the decoupling point.	1) Yield criterion from plastic work contours 2) Associated flow rule, because of plastic work vectors 3) Pure kinematic hardening based on Ziegler translation rule Koiter rule is applied to add the plastic deformations of each surface	The model calibrates internally if the following input is given: 1) Depth of load reference point 2) Uniaxial input response curves, preferably based on cyclic loading 3) Number of surfaces
Loads	**Validation**	**Conclusion**
Monotonic and irregular cyclic loads in (V), M and H	The model is validated with a field test of a bucket foundation in clay exposed to cyclic loading	Good agreement, especially for the stiffness. However, the damping is slightly underestimated by the macro-element.
Limitations	**Application range**	**Suggestions further research**
1) Macro-element does not consider displacement accumulation, cyclic degradation of stiffness, pore pressure changes or mean stress changes.	The application of the macro-element is for bucket foundations exposed to cyclic loading for low to moderate load levels. The model is developed for integrated analyses, therefore, long-term effects are not incorporated.	1) Extend the model from 3DoF to 5DoF. A strategy is given, however, it is noted that there are limitations to the proposed strategy. 2) Verify the applicability of the macro-element in sand-dominated soils.

Table A.12: Overview of *A macro-element model for multi-directional cyclic lateral loading of monopiles in clay* by Page et al. [39] that present a 6 DoF macro-element model within the elasto-plasticity framework

Assumptions	**Input to model**	**Model Calibration**
1) If one yield surface is active, all the surfaces enclosed by that surface are also active. All surfaces outside the first inactive yield surface are inactive. 2) Series-coupled homothetic yield surfaces 3) The vertical DoF are modelled uncoupled elastic	1) Yield criterion from plastic work contours. Transformation matrix is applied to scale the yield surfaces to a single load invariant. 2) Associated flow rule, because of plastic work vectors 3) Koiter rule is applied to add the plastic deformations of each surface.	1) Coefficients of the elastic stiffness matrix 2) Load-displacement curves from non-linear analyses, it is proposed to use these from a static pushover FEA. However, backbone curve as suggested by Kaynia & Andersen (2015) also possible.
Loads	**Validation**	**Conclusion**
Multi-directional cyclic loading, with ULS load history.	The macro-element is verified with 3D FEA that is based on a similar constitutive approach as the macro-element (multi-surface plasticity)	Coupling between the two planes is observed from relatively small load levels to the load levels corresponding to a ULS storm. Author questions whether planar models are adequate for foundation analyses.
Limitations	**Application range**	**Suggestions further research**
1) This model is extension of Page 2018, hence the same limitations apply. The formulation of the in and out of plane loads is based on symmetry conditions. 2) The good agreement between the macro-element and the FEA might be a consequence of the constitutive soil model that is employed in the FEA: both models use same formulation	The model is validated for a short loading range, max. 30 s. Also for the peak of the used ULS storm the macro-element gives a good agreement. So, application range of the model is from small load level to the maximum load level as validated with in this paper. The application of the macro-element is mostly for FLS analyses, for piles where length and diameter are set.	1) Validate the macro-element model with experimental data representative for an OWT.

Appendix B

Implementation in SGRE Design Tools

The content of this appendix is omitted in public versions, for confidentiality reasons.

Appendix C

Additional Results Comparative Study

Within this Appendix, some additional results of the comparative study are included. These results are considered to be merely supplementary to the results given in Chapter 3. First, the comparison of the response for the FLS is plotted. Further, this Appendix includes the results of the PLAXIS analyses for verification of the MEM1 model.

C.1 Fatigue Limit State

It is shown by Page et.al. [39] that the macro-element successfully captures the 3D multi-directional response from FEA. In order to verify that any discrepancies in the obtained response are due to the load level, one FLS load cycle is run. The loads are site-specific FLS loads generated in BHawC, complying to design load case (DLC) 7.2 (Armstrong, private communication). Here, the loads are presented normalised, as the OWF is still in development.

Figure C.1 depicts the normalised FLS loads that are input for the FEA and the macro-element model. Figure C.2 present the resulting displacements to the input loads. It is seen that the agreement from the FEA and the macro-element model is very good. Moreover, it is observed that plastic displacements are generated, as the elastic displacements are also included in Figure C.2. It is noticed that plastic displacements initially do not develop. It is postulated that the increase in plastic displacements is due to the distribution of the yield

surfaces in load space. Originally, the yield surfaces are situated at the origin of the π-plane and hence the distance to the first yield surface might be larger than on the consequent loading paths, depending on the load direction.

Finally, Figure C.3 presents the normalised response in the load displacement plane. It should be noted that the model is coupled in x- and y-direction and thus there are effects from y-plane on the x-plane response included. It is especially worth noting, that the moment load approximates one load cycle (Figure C.1). In the right plot of Figure C.3, a small hysteresis loop is observed, of which the area denotes the soil damping.

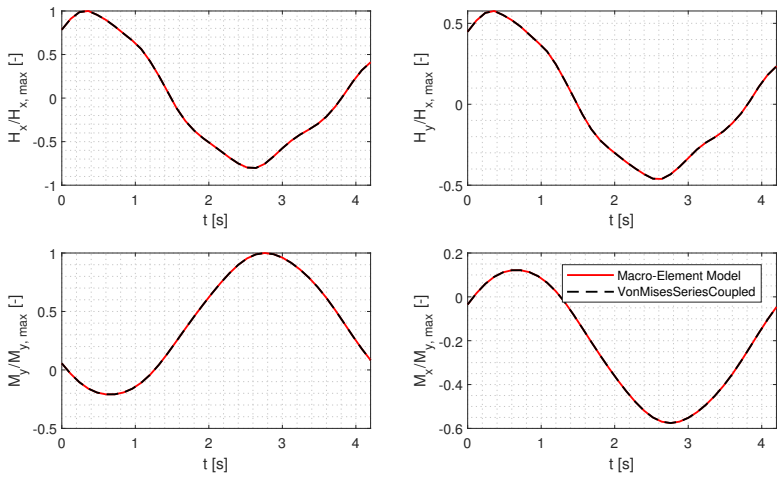

Figure C.1: Normalised input loads for the macro-element model and 3D finite element analyses in the fatigue limit state

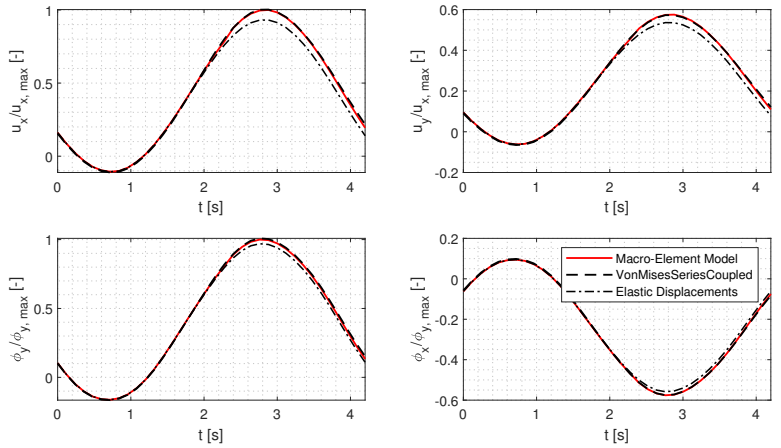

Figure C.2: Normalised resulting displacements for the macro-element model and 3D finite element analyses, including the elastic response, in the fatigue limit state.

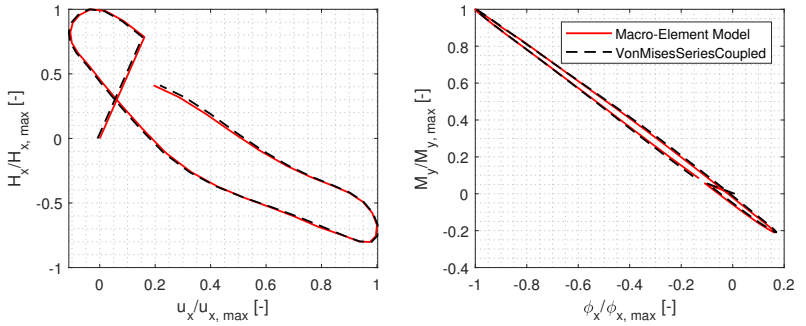

Figure C.3: Normalised response in load-displacement plane for the fatigue limit state.

C.2 Soft Soil Response in the Ultimate Limit State

The response at mudline with API p-y springs is much softer than the mudline response from 3D FEA (Figure 4.3). Therefore a short verification analyses is performed, that assesses the mudline response to extreme loads. The loads are equivalent to the loads that are portrayed by Figure 3.14.

Figure C.4 depicts the input calibration curves for the macro-element model for a model calibrated against the pre-defined API formulations and calibrated against soft soil. The former soil profile is calibrated from input data of the selected site, while the latter soil profile has similar properties as the FSP and RSP. However, the stiffness of the soil is reduced to 20% of the stiffness of the RSP profile. As the soft soil profile gives an even softer response than the soil profile calibrated to the lateral API springs, the response of the soft soil is governing in the comparative study.

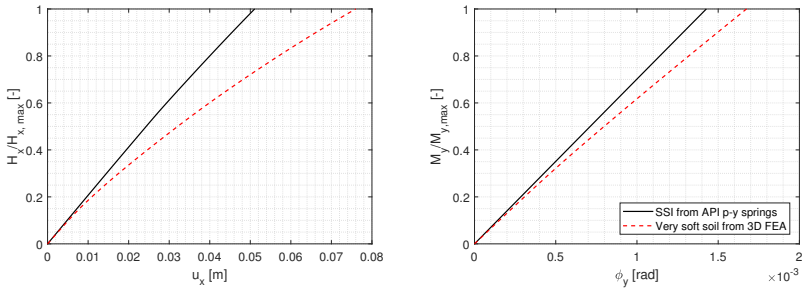

Figure C.4: Input calibration curves of the macro-element model. The soil-structure interaction is from API p-y springs and very soft soil in 3D the finite element model. For brevity, the H-ϕ and M-u curves are omitted.

As the analyses in Chapter 4 consist of planar load cases, the response at mudline for very soft soil condition is evaluated in a planar load case. The response at mudline (M, F) is obtained for an OWT exposed to wave loading, as shown in Figure 3.17. The corresponding response at mudline is included in Figure C.5. The maximum loads are lower than the maximum loads that the multi-directional cyclic loads use, but still higher than the loads of Page et al. [39]. The FEA uses this response at mudline this as an input. The displacements are depicted in Figure C.6. The agreement is very good, also at the peak loads.

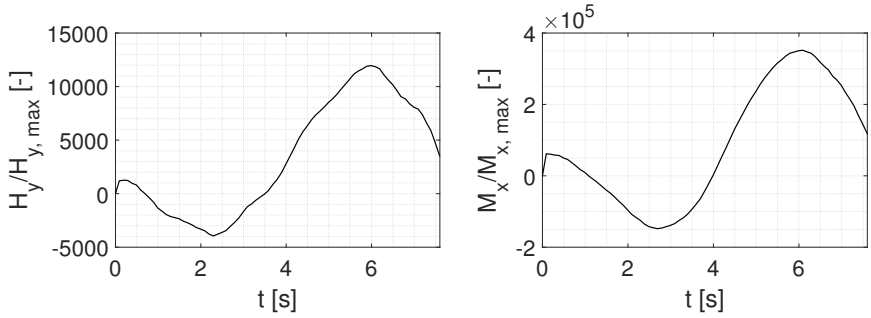

Figure C.5: Normalised mudline response from the integrated foundation design tool of SGRE with the macro-element foundation model. Input for load-controlled 3D finite element analyses

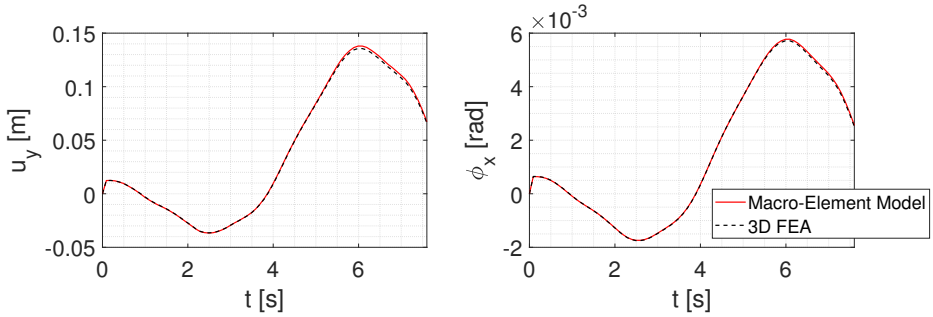

Figure C.6: Macro-element model and FEA planar response at mudline to ULS time series for very soft soil of which the load-displacement curves compares with the load-displacement curves at mudline obtained with soil-structure interaction from API *p-y* curves.

Appendix D

Time Domain Results for Interference Study

The interference term, as defined in Chapter 5, is for all multi-frequency excitation forced vibration analyses depicted as the phase difference with respect to a summation of two single-frequency excitation forced vibrations. This phase difference is defined as the phase difference between the maxima of the forced vibrations. As the phase difference is actually periodic, the response at mudline to these excitations is given in this Appendix. Moreover, from the time domain results the part of the interference term that affects the amplitude of the response may also be observed. This Appendix gives the time domain results for multi-frequency excitation vibrations with the MEM1 and MEM2 foundation model, calibrated against the API *p-y* curves and 3D FEA, respectively. For any interpretation of the results, reference is made to Chapter 5.

D.1 Macro-Element Model 1

Macro-element model 1 (MEM1) is calibrated to the API pre-defined functions and hence the estimated behaviour is not accurate for low L/D piles, as used in this thesis (e.g. [23, 25, 46]). This should be taken into account while interpreting the results. Figure D.1 to D.3 show the response to these excitations for $f_a = 0.95\ f_0$ and $f_b = f_0$. Figure D.4 to D.6 depict the response for frequencies that are more closely spaced with $f_a = 0.975\ f_0$ and $f_b = f_0$.

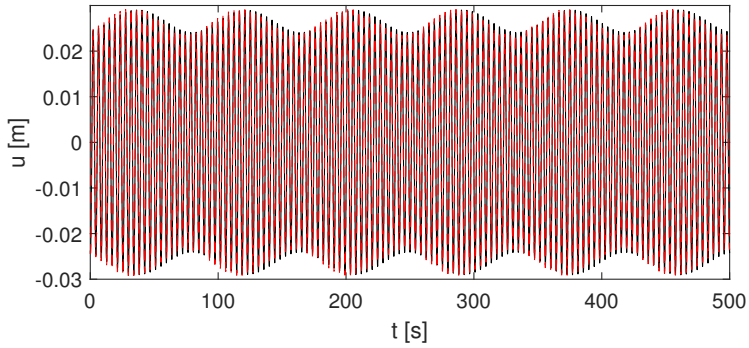

Figure D.1: Summation of single frequency excitation response (——) and the multi-frequency excitation response (- - -) at mudline for F_{ampl} = 10 kN, f_a = 0.95 f_0 and f_b = f_0.

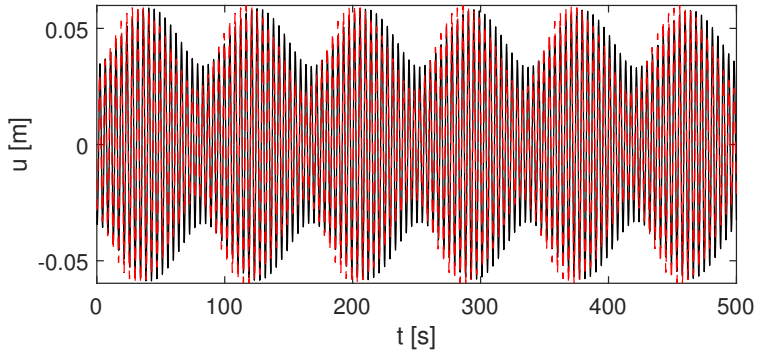

Figure D.2: Summation of single frequency excitation response (——) and the multi-frequency excitation response (- - -) at mudline for F_{ampl} = 50 kN, f_a = 0.95 f_0 and f_b = f_0.

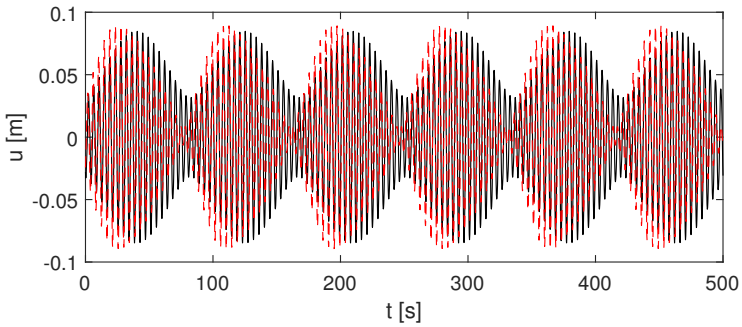

Figure D.3: Summation of single frequency excitation response (——) and the multi-frequency excitation response (- - -) at mudline for F_{ampl} = 100 kN, f_a = 0.95 f_0 and f_b = f_0.

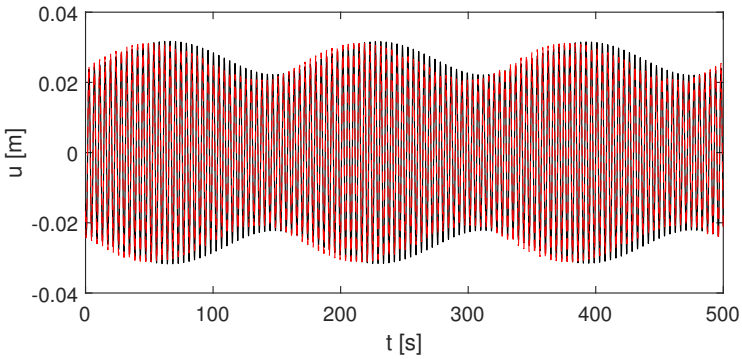

Figure D.4: Summation of single frequency excitation response (——) and the multi-frequency excitation response (- - -) at mudline for F_{ampl} = 10 kN, f_a = 0.975 f_0 and f_b = f_0.

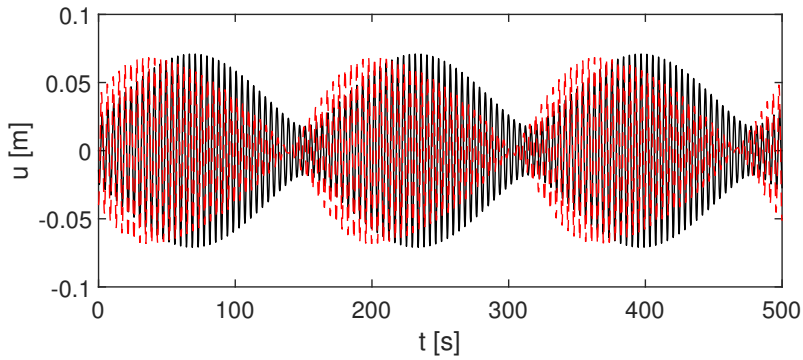

Figure D.5: Summation of single frequency excitation response (——) and the multi-frequency excitation response (- - -) at mudline for F_{ampl} = 50 kN, f_a = 0.975 f_0 and f_b = f_0.

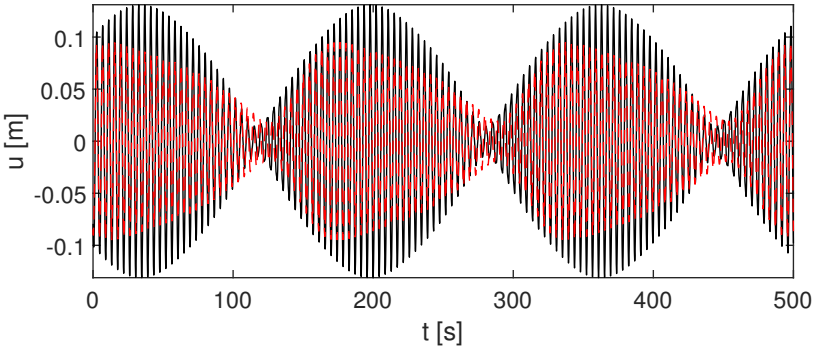

Figure D.6: Summation of single frequency excitation response (——) and the multi-frequency excitation response (- - -) at mudline for F_{ampl} = 100 kN, f_a = 0.975 f_0 and f_b = f_0.

D.2 Macro-Element Model 2

The MEM2 foundation model is calibrated against 3D finite element analyses, resulting in (initial) stiffer behaviour of the monopile at mudline. The same multi-frequency forced

vibration analyses are performed as with the MEM1 model. Figure D.7 to **??** give the response to forced vibration with excitation frequencies f_a = 0.95 f_0 and f_b = f_0, with varying amplitude. Figure D.10 to D.12 give the response for the same excitation amplitudes but more closely spaced frequencies, f_a = 0.975 f_0 and f_b = f_0.

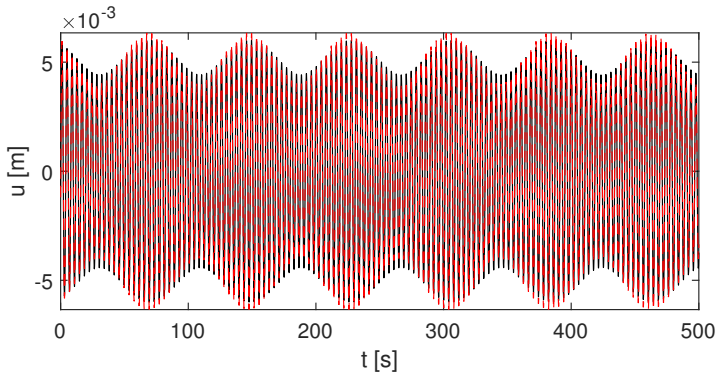

Figure D.7: Summation of single frequency excitation response (——) and the multi-frequency excitation response (- - -) at mudline for F_{ampl} = 10 kN, f_a = 0.95 f_0 and f_b = f_0.

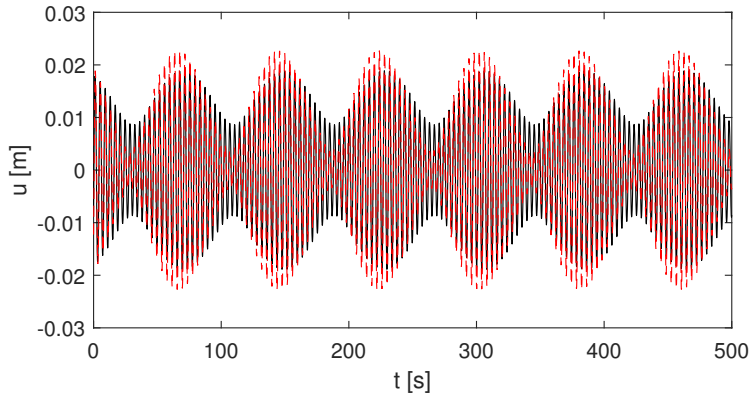

Figure D.8: Summation of single frequency excitation response (——) and the multi-frequency excitation response (- - -) at mudline for F_{ampl} = 50 kN, f_a = 0.95 f_0 and f_b = f_0.

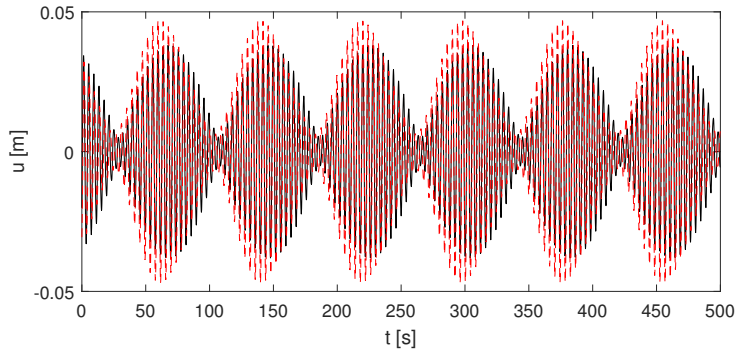

Figure D.9: Summation of single frequency excitation response (——) and the multi-frequency excitation response (- - -) at mudline for F_{ampl} = 100 kN, f_a = 0.95 f_0 and f_b = f_0.

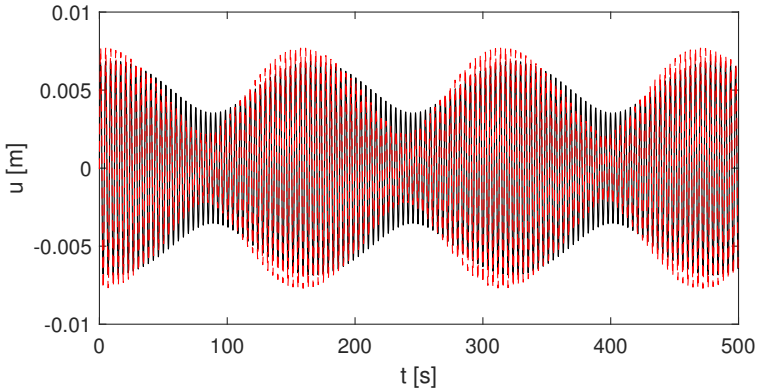

Figure D.10: Summation of single frequency excitation response (——) and the multi-frequency excitation response (- - -) at mudline for F_{ampl} = 10 kN, f_a = 0.975 f_0 and f_b = f_0.

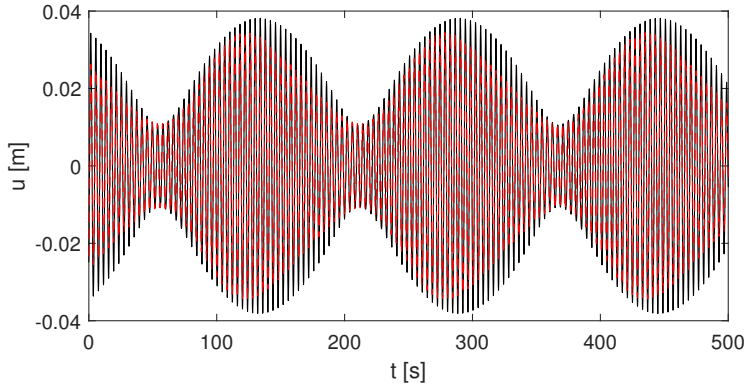

Figure D.11: Summation of single frequency excitation response (——) and the multi-frequency excitation response (- - -) at mudline for F_{ampl} = 50 kN, f_a = 0.975 f_0 and f_b = f_0.

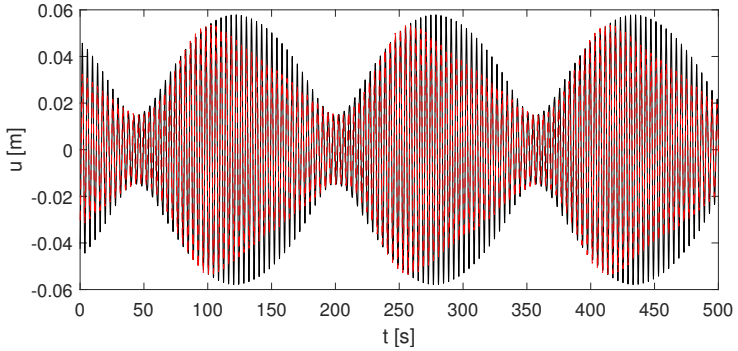

Figure D.12: Summation of single frequency excitation response (——) and the multi-frequency excitation response (- - -) at mudline for F_{ampl} = 100 kN, f_a = 0.975 f_0 and f_b = f_0.

Appendix E

The Elasto-Plastic Stiffness Matrix

To improve the convergence of the Newton-Raphson solver, the non-linear stiffness matrix at mudline may be updated for every displacement increment. Currently, the implementation is based on a MN-R scheme, that relies on the initial soil stiffness. In case large non-linearities are observed, the macro-element model may be expanded to include an update of the soil stiffness matrix. However, as the model accounts for multi-directional (un)loading behaviour, the implementation of the elasto-plastic stiffness matrix, $\boldsymbol{K}^{ep}$, should be done with care. This is mostly due to the behaviour in the Newton-Raphson iterative scheme, since if the predicted stiffness is too soft (e.g. first unloading), the N-R solver will not converge. Below the derivation of $\boldsymbol{K}^{ep}$ and the results of the implementation in the 2DoF macro-element model of the project thesis are given [41].

E.1 Derivation of the Stiffness Matrix

As the macro-element model is based on elasto-plasticity formulations, Equation 2.1. With the elastic and plastic component defined as in Equation E.1 and E.2, respectively. It should be noted that Equation E.2 gives the total plastic displacement as may be obtained from the multi-surface plasticity macro-element model (Koiter rule [71]).

$$\underline{v}^{e} = \boldsymbol{K}^{e-1}\,\underline{t} \tag{E.1}$$

$$\underline{v}^p = \sum_{i=1}^{j} d\lambda_i \frac{\partial g_i}{\partial \underline{t}} = \sum_{i=1}^{j} d\lambda_i \frac{\partial f_i}{\partial \underline{t}} \tag{E.2}$$

Due to associativity of the flow rule, the plastic potential (g) equals the yield criterion (f). And i and j are the total and active number of yield surfaces, respectively. Now, for the force increment, $d\boldsymbol{t}$, Equation E.3 may be derived.

$$d\underline{t} = \boldsymbol{K^e} \left(d\underline{v} - d\lambda_1 \frac{\partial f_1}{\partial \underline{t}} - \ldots - d\lambda_j \frac{\partial f_j}{\partial \underline{t}} \right) \tag{E.3}$$

Thus, a formulation for the plastic multiplier, $d\lambda$ is required, which is derived by, for instance, Skau et al. [33]. This relation is presented in Equation E.4 and is used to obtain the elasto-plastic stiffness matrix, $\boldsymbol{K}^{ep}$.

$$\underline{d\lambda} = \begin{bmatrix} d\lambda_1 \\ d\lambda_2 \\ \vdots \\ d\lambda_j \end{bmatrix} = \begin{bmatrix} a_{11} + A_1 & a_{12} & \cdots & a_{1j} \\ a_{21} & a_{22} + A_2 & \cdots & a_{2j} \\ \vdots & \vdots & \ddots & \vdots \\ a_{j1} & a_{j2} & \cdots & a_{jj} + A_j \end{bmatrix} \begin{bmatrix} f_1 \\ f_2 \\ \vdots \\ f_j \end{bmatrix} = \boldsymbol{\Xi}^{-1} \underline{f} \tag{E.4}$$

With a_{ik} and A_k as stated in Equation E.5.

$$a_{ik} = \left\{ \frac{\partial f_i}{\partial \underline{t}} \right\}^T \boldsymbol{K}^e \left\{ \frac{\partial g_k}{\partial \underline{t}} \right\} \quad , \quad A_k = \left\{ \frac{\partial f_k}{\partial \underline{t}} \right\}^T \boldsymbol{K}_k^p \left\{ \frac{\partial g_k}{\partial \underline{t}} \right\} \tag{E.5}$$

According to Skau et al. [33], the vector $\underline{f}$ may also be written as in Equation E.6.

$$\underline{f} = \begin{bmatrix} \frac{\partial f_1}{\partial \underline{t}} \boldsymbol{K^e}\, d\underline{v} \\ \frac{\partial f_2}{\partial \underline{t}} \boldsymbol{K^e}\, d\underline{v} \\ \vdots \\ \frac{\partial f_j}{\partial \underline{t}} \boldsymbol{K^e}\, d\underline{v} \end{bmatrix} \tag{E.6}$$

Substituting Equation E.6 in Equation E.4 and consequently including this in Equation E.3 gives Equation E.7 for $d\underline{t}$.

$$d\underline{t} = \boldsymbol{K}^e \, d\underline{v} - \boldsymbol{K}^e \left(\left(\Xi^{-1} \begin{bmatrix} \frac{\partial f_1}{\partial \underline{t}} \boldsymbol{K^e} \, d\underline{v} \\ \frac{\partial \bar{f}_2}{\partial \underline{t}} \boldsymbol{K^e} \, d\underline{v} \\ \vdots \\ \frac{\partial f_j}{\partial \underline{t}} \boldsymbol{K^e} \, d\underline{v} \end{bmatrix} \right)_1 \frac{\partial f_1}{\partial d\underline{t}} + \ldots + \left(\Xi^{-1} \begin{bmatrix} \frac{\partial f_1}{\partial \underline{t}} \boldsymbol{K^e} \, d\underline{v} \\ \frac{\partial \bar{f}_2}{\partial \underline{t}} \boldsymbol{K^e} \, d\underline{v} \\ \vdots \\ \frac{\partial f_j}{\partial \underline{t}} \boldsymbol{K^e} \, d\underline{v} \end{bmatrix} \right)_j \frac{\partial f_j}{\partial d\underline{t}} \right) \tag{E.7}$$

As $\boldsymbol{K}^{ep}$ is defined as $\frac{d\underline{t}}{d\underline{v}}$, the obtained formulation of $\boldsymbol{K}^{ep}$ is as is given by Equation E.8.

$$\boldsymbol{K}^{ep} = \boldsymbol{K}^e - \boldsymbol{K}^e \left(\left(\Xi^{-1} \begin{bmatrix} \frac{\partial f_1}{\partial \underline{t}} \boldsymbol{K^e} \\ \frac{\partial \bar{f}_2}{\partial \underline{t}} \boldsymbol{K^e} \\ \vdots \\ \frac{\partial f_j}{\partial \underline{t}} \boldsymbol{K^e} \end{bmatrix} \right)_1 \frac{\partial f_1}{\partial d\underline{t}} + \ldots + \left(\Xi^{-1} \begin{bmatrix} \frac{\partial f_1}{\partial \underline{t}} \boldsymbol{K^e} \\ \frac{\partial \bar{f}_2}{\partial \underline{t}} \boldsymbol{K^e} \\ \vdots \\ \frac{\partial f_j}{\partial \underline{t}} \boldsymbol{K^e} \end{bmatrix} \right)_j \frac{\partial f_j}{\partial d\underline{t}} \right) \tag{E.8}$$

Thus, as expected, the elasto-plastic stiffness matrix is dependent on the number of active yield surfaces. Please note, in case only the first yield surface is active, the formulation reduces to the formulation for $\boldsymbol{K}^{ep}$, as given by, for instance, Nordal [62].

E.2 Implementation in the 2DoF Macro-Element Model

The expression for $\boldsymbol{K}^{ep}$ is included in the 2DoF macro-element model that is developed for the project thesis [41]. The analysis is performed for a macro-element model exposed to pure shear loading. Figure E.1 illustrates the load path (left) and the response in the load-displacement plane (right). Further, Figure E.2 shows the movement of the yield surface in load space. Finally, Figure E.3 presents the development of K_{11} of the elasto-plastic stiffness matrix for the one hysteresis loop (loading-unloading-reloading).

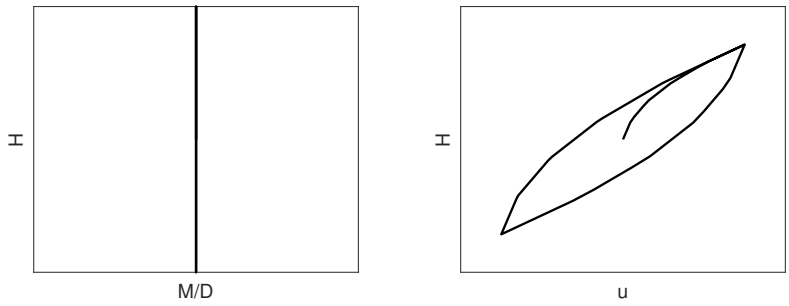

Figure E.1: Load path in load space for pure shear loading (left) and corresponding hysteretic response (right)

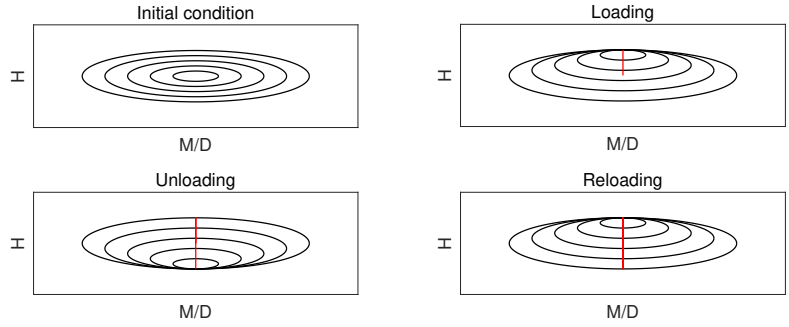

Figure E.2: Movement of yield surfaces (——) in load space when exposed to pure shear loading (——).

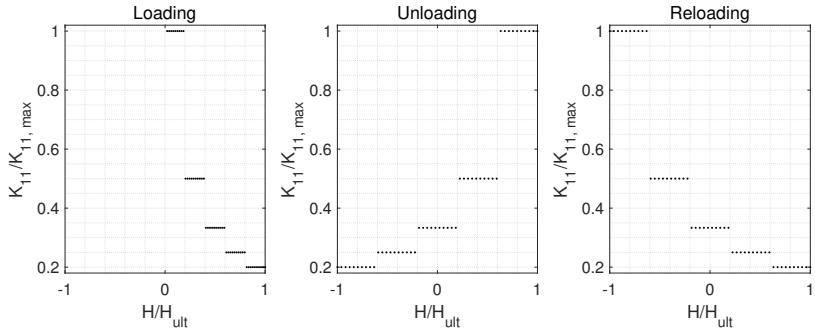

Figure E.3: Stiffness matrix coefficient K_{11} versus applied load level (H) for one hysteresis loop.

From Figure E.3 it is observed that the gradient of the stiffness matrix is discontinuous. This is caused by the yield surfaces: upon activation of a yield surface, the total $\boldsymbol{K}^{ep}$ reduces. As the 2DoF model consists of five surfaces only, this is conform expectations. For a larger number of surfaces, even infinite surfaces [70], the development of the elasto-plastic stiffness matrix will resemble more continuous degradation of the stiffness.

Definitions

Co-directional The direction of the wind and wave loads is aligned.

Hysteretic damping Frequency independent damping, that is often dependent on the displacement amplitude. Energy loss due to yielding or internal friction of the material and is therefore also known as material damping.

Integrated design analyses Design philosophy that focuses on a simultaneous optimisation of the support structure, instead of separately designing the foundation and tower.

Macro-element model Foundation model that condenses the soil-foundation interaction to a force-displacement formulation, usually at mudline. When denoted in this thesis, the REDWIN multi-directional macro-element model for monopile foundations developed by Page et al. [39] is meant.

Masing rules Rules that determine the hysteretic behaviour of a material that is exposed to cyclic loading. The combination of the work of Masing [47] and later work by Pyke [48] are known as the extended Masing rules.

Modal damping Determination of critical damping that is mode dependent.

Monopile Single large-diameter steel tube, used as foundation for offshore wind turbines.

Soil structure interaction The mechanism where the motion of the structure is determined by the response of the soil and vice versa.

Uni-directional The environmental loads are excited in one direction.

Viscous damping Damping that may be used as an equivalent viscous force in the equation of motion. The viscous damping is typically obtained from a summation of the various sources of damping.

Winkler model Foundation model that models the soil-structure interaction as a beam supported by uncoupled elastic springs along the embedded length.

Bibliography

[1] DNV - GL, "*Support structures for wind turbines*," design standard, Oslo, Norway, Apr. 2016.

[2] D. Kallehave, B. W. Byrne, C. LeBlanc Thilsted, and K. K. Mikkelsen, "Optimization of monopiles for offshore wind turbines," *Philosophical Transactions of the Royal Society of London A: Mathematical, Physical and Engineering Sciences*, vol. 373, no. 2035, 2015.

[3] United Nations, "Report of the Conference of the Parties on its twenty-first session, held in Paris from 30 November to 13 December 2015," 2016.

[4] European Parliament, "*Energy: new target of 32% from renewables by 2030 agreed by MEPs and ministers*," press release, 2018.

[5] Bart Zuidervaart, "*Record-low bids in offshore wind should make policy makers rethink post-2020 ambition levels*," 2017. https://www.trouw.nl/groen/rutte-iii-presenteert-een-ambitieus-maar-risicovol-klimaatplan~a9f230bc/ [Accessed: 15-03-2019].

[6] Klimaatberaad, "Ontwerp van het Klimaatakkoord," tech. rep., 2018.

[7] WindEurope, "*Offshore Wind in Europe - key trends and statistics*," report, WindEurope, 2018.

[8] B. W. Byrne and G. T. Houlsby, "Foundations for Offshore Wind Turbines," *Philosophical Transactions of the Royal Society of London A: Mathematical, Physical and Engineering Sciences*, vol. 361, no. 1813, pp. 2909–2930, 2003.

[9] WindEurope, "*Wind in power 2017 - Annual combined onshore and offshore wind energy statistics*," report, WindEurope, 2018.

[10] R. Koelemeijer, B. Daniëls, P. Boot, P. Koutstaal, S. Kruitwagen, G. Gellenkirchen, M. Menkveld, J. Ros, G. J. van den Born, S. Lensink, and M. van Hout, "Analyse regeerakkoord Rutte-III: effecten op klimaat en energie," note, PBL and ECN, 2017.

[11] C. Kost, S. Shammugan, V. Juelch, H.-T. Nguyen, and T. Schlegl, "*Levelised Cost of Electricity Renewable Energy Technologies*," tech. rep., Fraunhofer Institute for Solar Energy Systems ISE, 2018.

[12] IRENA, "*Innovation Outlook: Off shore Wind, International Renewable Energy Agency*," 2016. Abu Dhabi.

[13] EWEA, "*Deep Water - The next step for Offshore Wind Energy*," report, European Wind Energy Association, 2013.

[14] Ørsted, "*DONG Energy awarded three German offshore wind projects*," 2017. https://orsted.com/en/Company-Announcement-List/2017/04/1557851 [Accessed: 12-10-2018].

[15] Vattenfall, "*Vattenfall wins tender Hollandse Kust Zuid*," 2018. https://group.vattenfall.com/press-and-media/news--press-releases/pressreleases/2018/vattenfall-wins-tender-hollandse-kust-zuid [Accessed: 12-10-2018].

[16] WindEurope, "*Record-low bids in offshore wind should make policy makers rethink post-2020 ambition levels*," 2017. https://windeurope.org/newsroom/news/record-low-bids-in-offshore-wind-should-make-policy-makers-rethink-post- 2020-ambition-levels/ [Accessed: 20-11-2018].

[17] Wood Mackenzie, "Asia-Pacific offshore wind capacity to rise 20-fold in next decade," 2018. https://www.woodmac.com/press-releases/asia-pacific-offshore-wind-capacity-to-rise-20-fold-in-next-decade/[Accessed: 14-06-2019].

[18] K. Hermans and J. Peeringa, "*Future XL monopile foundation design for a 10 MW wind turbine in deep water*," technical report, ECN, 2016. ECN-E–16-069.

[19] R. Haghi, T. Ashuri, P. L. van der Valk, and D. P. Molenaar, "Integrated multidisciplinary constrained optimization of offshore support structures," in *Journal of Physics: Conference Series*, vol. 555, p. 012046, IOP Publishing, 2014.

[20] M. Seidel, S. Voormeeren, and J.-B. van der Steen, "State-of-the-art design processes for offshore wind turbine support structures: Practical approaches and pitfalls during different stages in the design process," *Stahlbau*, vol. 85, no. 9, pp. 583–590, 2016.

[21] W. G. Versteijlen, J. M. de Oliveira Barbosa, K. N. van Dalen, and A. V. Metrikine, "Dynamic soil stiffness for foundation piles: Capturing 3d continuum effects in an effective, non-local 1d model," *International Journal of Solids and Structures*, vol. 134, pp. 272–282, 2018.

[22] API, "*Recommended Practice for Planning, Designing and Constructing Fixed Offshore Platforms âĂŤ Working Stress Design*," design standard, Washington D.C., USA,

Dec. 2000.

[23] P. Doherty and K. Gavin, "Laterally loaded monopile design for offshore wind farms," *Energy*, vol. 165, pp. 7–17, 2011.

[24] H. G. Poulos and T. S. Hull, "The Role of Analytical Geomechanics in Foundation Engineering," in *Foundation engineering: Current principles and practices*, pp. 1578–1606, ASCE, 1989.

[25] B. Byrne, R. McAdam, H. Burd, G. Houlsby, C. Martin, L. Zdravković, D. Taborda, D. Potts, R. Jardine, M. Sideri, *et al.*, "New design methods for large diameter piles under lateral loading for offshore wind applications," in *3rd International Symposium on Frontiers in Offshore Geotechnics (ISFOG 2015), Oslo, Norway, June*, pp. 10–15, 2015.

[26] B. Byrne, R. McAdam, H. Burd, G. Houlsby, C. Martin, W. Beuckelaers, L. Zdravkovic, D. Taborda, D. Potts, R. Jardine, *et al.*, "PISA: New Design Methods for Offshore Wind Turbine Monopiles," *Proceedings of the 8th Offshore Site Invesigation & Geotechnics (OSIG) International Conference*, pp. 142–161, 2017. London, UK.

[27] T. Hald, C. Mørch, L. Jensen, C. Bakmar, and K. Ahle, "Revisiting monopile design using py curves. Results from full scale measurements on Horns Rev," in *Proceedings of European Offshore Wind 2009 Conference*, 2009.

[28] W. G. Versteijlen, F. W. Renting, P. L. C. van der Valk, J. Bongers, K. N. van Dalen, and A. V. Metrikine, "Effective soil-stiffness validation: Shaker excitation of an in-situ monopile foundation," *Soil Dynamics and Earthquake Engineering*, vol. 102, pp. 241–262, 2017.

[29] W. G. Versteijlen, A. V. Metrikine, and K. N. van Dalen, "A method for identification of an effective winkler foundation for large-diameter offshore wind turbine support structures based on in-situ measured small-strain soil response and 3d modelling," *Engineering Structures*, vol. 124, pp. 221–236, 2016.

[30] H. J. Burd, B. Byrne, R. Mcadam, G. Houlsby, C. Martin, W. Beuckelaers, L. Zdravković, D. Taborda, D. Potts, R. Jardine, *et al.*, "Design aspects for monopile foundations," in *Proc. TC209 Workshop, 19th International Conference on Soil Mechanics and Geotechnical Engineering (ICSMGE)*, pp. 35–44, 2017.

[31] W. J. A. P. Beuckelaers, *Numerical Modelling of Laterally Loaded Piles for Offshore Wind Turbines*. PhD thesis, University of Oxford, 2017.

[32] A. M. Page, *Monopile foundation models for dynamic structural analysis of Offshore Wind Turbines*. PhD thesis, Norwegian University of Science and Technology, 2018.

[33] K. S. Skau, G. Grimstad, A. M. Page, G. R. Eiksund, and H. P. Jostad, "A macro-element for integrated time domain analyses representing bucket foundations for offshore wind

turbines," *Marine Structures*, vol. 59, pp. 158 – 178, 2018.

[34] R. Nova and L. Montrasio, "Settlements of shallow foundations on sand," *Géotechnique*, vol. 41, no. 2, pp. 243–256, 1991.

[35] G. Gazetas, "Formulas and charts for impedances of surface and embedded foundations," *Journal of geotechnical engineering*, vol. 117, no. 9, pp. 1363–1381, 1991.

[36] S. Aasen, A. M. Page, K. S. Skau, and T. A. Nygaard, "Effect of foundation modelling on the fatigue lifetime of a monopile-based offshore wind turbine," *Wind Energy Science*, vol. 2, no. 2, pp. 361–376, 2017.

[37] A. M. Page, V. Næss, J. B. De Vaal, G. R. Eiksund, and T. A. Nygaard, "Impact of foundation modelling in offshore wind turbines: comparison between simulations and field data," *Accepted by Marine Structures*, 2019.

[38] G. Katsikogiannis, E. E. Bachynski, and A. M. Page, "Fatigue sensitivity to foundation modelling in different operation states for the DTU 10MW monopile-based offshore wind turbine," *Submitted for publication*, 2019.

[39] A. M. Page, G. Grimstad, G. R. Eiksund, and H. P. Jostad, "A macro-element model for multidirectional cyclic lateral loading of monopiles in clay," *Computers and Geotechnics*, vol. 106, pp. 314–326, 2019.

[40] A. M. Page, G. Grimstad, G. R. Eiksund, and H. P. Jostad, "A macro-element pile foundation model for integrated analyses of monopile-based offshore wind turbines," *Ocean Engineering*, vol. 167, pp. 23 – 35, 2018.

[41] S.C. van Hoogstraten, "*The Macro-Element Method for Integrated Analyses of Offshore Wind Turbines - Literature Review on capturing Nonlinear Hysteretic Soil-Monopile Behaviour*," 2018. Project Thesis, Norwegian University of Science and Technology.

[42] A. M. Page, S. Schafhirt, G. R. Eiksund, K. S. Skau, H. P. Jostad, and H. Sturm, "Alternative Numerical Pile Foundation Models for Integrated Analyses of Monopile-based Offshore Wind Turbines," *Proceedings of the Twenty-sixth International Ocean and Polar Engineering Conference - ISOPE 2016*, pp. 111–119, 2016.

[43] G. T. Houlsby and B. W. Byrne, "Suction caisson foundations for offshore wind turbines and anemometer masts," *Wind engineering*, vol. 24, no. 4, pp. 249–255, 2000.

[44] S. Bhattacharya, "Challenges in design of foundations for offshore wind turbines," *Engineering & Technology Reference*, vol. 1, no. 1, pp. 1–9, 2014.

[45] K. S. Skau, *Modelling of skirted foundations for offshore wind turbines*. PhD thesis, Norwegian University of Science and Technology, 2018.

[46] A. M. Page, K. S. Skau, H. P. Jostad, and G. R. Eiksund, "A New Foundation Model for Integrated Analyses of Monopile-based Offshore Wind Turbines," *Energy Procedia*,

vol. 137, pp. 100 – 107, 2017. 14th Deep Sea Offshore Wind R&D Conference, EERA DeepWind'2017.

[47] G. Masing, "Eigenspannungen und verfestigung beim messing," *Proceedings of the 2nd International Congress of Applied Mechanics*, pp. 332–335, 1926.

[48] R. M. Pyke, "Nonlinear soil models for irregular cyclic loadings," *Journal of geotechnical and geoenvironmental engineering*, vol. 105, no. ASCE 14642 Proceeding, 1979.

[49] C. N. Abadie, B. W. Byrne, and G. T. Houlsby, "Rigid pile response to cyclic lateral loading: laboratory tests," *Géotechnique*, pp. 1–14, 2018.

[50] A. Kaynia and K. Andersen, "Development of nonlinear foundation springs for dynamic analysis of platforms," *Frontiers in Offshore Geotechnics III, Oslo*, 2015.

[51] S. Pranjoto and M. Pender, "Gapping effects on the lateral stiffness of piles in cohesive soil," in *Proceedings of Pacific Conference on Earthquake Engineering, Christchurch, New Zealand*, pp. 13–15, 2003.

[52] M. Heidari, M. Jahanandish, H. El Naggar, and A. Ghahramani, "Nonlinear cyclic behavior of laterally loaded pile in cohesive soil," *Canadian Geotechnical Journal*, vol. 51, no. 2, pp. 129–143, 2013.

[53] G. T. Houlsby, C. N. Abadie, W. J. A. P. Beuckelaers, and B. W. Byrne, "A model for nonlinear hysteretic and ratcheting behaviour," *International Journal of Solids and Structures*, vol. 120, pp. 67–80, 2017.

[54] S. Schafhirt, A. Page, G. R. Eiksund, and M. Muskulus, "Influence of soil parameters on the fatigue lifetime of offshore wind turbines with monopile support structure," *Energy Procedia*, vol. 94, pp. 347–356, 2016.

[55] L. Andersen, "Assessment of lumped-parameter models for rigid footings," *Computers & structures*, vol. 88, no. 23-24, pp. 1333–1347, 2010.

[56] Z. Li, P. Kotronis, S. Escoffier, and C. Tamagnini, "A hypoplastic macroelement for single vertical piles in sand subject to three-dimensional loading conditions," *Acta Geotechnica*, vol. 11, no. 2, pp. 373–390, 2016.

[57] A. Foglia, G. Gottardi, L. Govoni, and L. B. Ibsen, "Modelling the drained response of bucket foundations for offshore wind turbines under general monotonic and cyclic loading," *Applied Ocean Research*, vol. 52, pp. 80–91, 2015.

[58] A. Løkke, A. M. Page, and K. S. Skau, *REDWIN: Reducing cost of offshore wind by integrated structural and geotechnical design - 3D foundation model library*. NGI, 2018. Manual.

[59] V. Næss, "*Optimization of Piles Supporting Monopile-Based Offshore Wind Turbines by Improved Foundation Models*," Master's thesis, Norwegian University of Science

and Technology, 2018.

[60] G. Grimstad and T. Benz, "*Lecture Notes PhD Course BA8305 Soil Modeling - Part 3 of 3*," September 2018. Norwegian University of Science and Technology.

[61] G. Houlsby, M. Cassidy, and I. Einav, "A generalised Winkler model for the behaviour of shallow foundations," *Géotechnique*, vol. 55, no. 6, pp. 449–460, 2005.

[62] S. Nordal, "*Lecture Notes PhD Course BA8305 Soil Modeling - Part 1 of 3*," September 2018. Norwegian University of Science and Technology.

[63] W. D. Iwan, "On a class of models for the yielding behavior of continuous and composite systems," *Journal of Applied Mechanics*, vol. 34, no. 3, pp. 612–617, 1967.

[64] Z. Mróz, "On the description of anisotropic workhardening," *Journal of the Mechanics and Physics of Solids*, vol. 15, no. 3, pp. 163 – 175, 1967.

[65] G. Grimstad, J. Rønningen, and H. Nøst, "Use of Iwan models for modelling anisotropic and cyclic behavior of clays," *Numererical Methods in Geotechnical Engineering*, vol. 1, pp. 49–55, 2014.

[66] W. Prager, "The theory of plasticity: a survey of recent achievements," *Proceedings of the Institution of Mechanical Engineers*, vol. 169, no. 1, pp. 41–57, 1955.

[67] H. Ziegler, "A modification of Pragers hardening rule," *Quarterly of Applied mathematics*, vol. 17, no. 1, pp. 55–65, 1959.

[68] F. J. Montáns and M. A. Caminero, "On the consistency of nested surfaces models and their kinematic hardening rules," *International journal of solids and structures*, vol. 44, no. 14-15, pp. 5027–5042, 2007.

[69] A. M. Puzrin and G. T. Houlsby, "On the non-intersection dilemma in multiple surface plasticity," *Géotechnique*, vol. 51, no. 4, pp. 369–372, 2001.

[70] A. Puzrin and G. T. Houlsby, "Fundamentals of kinematic hardening hyperplasticity," *International journal of Solids and Structures*, vol. 38, no. 21, pp. 3771–3794, 2001.

[71] W. T. Koiter, "Stress-strain relations, uniqueness and variational theorems for elastic-plastic materials with a singular yield surface," *Quarterly of Applied Mathematics*, vol. 11, no. 3, pp. 350–354, 1953.

[72] PLAXIS, "Plaxis 3D 2017 - Reference Manual," *Plaxis BV*, 2018.

[73] The MathWorks, Inc., "*MATLAB and Statistics Toolbox Release 2018a*," 2018. Natick, Massachusetts, United States.

[74] J. Velarde, "Design of monopile foundations to support the DTU 10 MW offshore wind turbine," Master's thesis, Norwegian University of Science and Technology, 2016.

[75] W. Higgins, C. Vasquez, D. Basu, and D. Griffiths, "Elastic solutions for laterally loaded piles," *Journal of Geotechnical and Geoenvironmental Engineering*, vol. 139,

pp. 1096–1103, 07 2013.

[76] J. Hutchinson, "Shear coefficients for timoshenko beam theory," *Journal of Applied Mechanics*, vol. 68, no. 1, pp. 87–92, 2001.

[77] S. Li, Y. Zhang, and H. P. Jostad, "Drainage conditions around monopiles in sand," *Applied Ocean Research*, vol. 86, pp. 111–116, 2019.

[78] T. Benz, P. Vermeer, and R. Schwab, "A small-strain overlay model," *International journal for numerical and analytical methods in geomechanics*, vol. 33, no. 1, pp. 25–44, 2009.

[79] K. H. Andersen, "Cyclic soil parameters for offshore foundation design," *Frontiers in offshore geotechnics III*, vol. 5, 2015.

[80] T. Benz, R. Schwab, and P. Vermeer, "Small-strain stiffness in geotechnical analyses," *Bautechnik*, vol. 86, no. S1, pp. 16–27, 2009.

[81] W. G. Versteijlen, *Identification of effective 1D soil models for large-diameter offshore wind turbine foundations based on in-situ seismic measurements and 3D modelling*. PhD thesis, Delft University of Technology, 2018.

[82] E. Kementzetzidis, S. Corciulo, W. G. Versteijlen, and F. Pisanò, "Geotechnical aspects of offshore wind turbine dynamics from 3d non-linear soil-structure simulations," *Soil Dynamics and Earthquake Engineering*, vol. 120, pp. 181–199, 2019.

[83] DNV - GL, "*Loads and site conditions for wind turbines*," design standard, Oslo, Norway, Nov. 2016.

[84] G. Murphy, D. Igoe, P. Doherty, and K. Gavin, "3d fem approach for laterally loaded monopile design," *Computers and Geotechnics*, vol. 100, pp. 76 – 83, 2018.

[85] W. G. Versteijlen, A. Metrikine, J. Hoving, E. Smidt, and W. De Vries, "Estimation of the vibration decrement of an offshore wind turbine support structure caused by its interaction with soil," in *Proceedings of the EWEA Offshore 2011 Conference, Amsterdam, The Netherlands, 29 November-1 December 2011*, European Wind Energy Association, 2011.

[86] A. P. Jeary, "The description and measurement of nonlinear damping in structures," *Journal of Wind Engineering and Industrial Aerodynamics*, vol. 59, no. 2-3, pp. 103–114, 1996.

[87] R. H. Rand, "Lecture notes on nonlinear vibrations," 2005. Cornell University.

[88] M. Feldman, "Hilbert transform in vibration analysis," *Mechanical systems and signal processing*, vol. 25, no. 3, pp. 735–802, 2011.

[89] G. Houlsby and M. Cassidy, "A plasticity model for the behaviour of footings on sand under combined loading," *Géotechnique*, vol. 52, no. 2, pp. 117–129, 2002.

[90] B. Bienen, B. Byrne, and G. Houlsby, "Six degree-of-freedom loading of a circular flat footing on loose sand: experimental data," *Report no. OUEL*, vol. 2289, no. 05, 2006.

[91] D. Salciarini and C. Tamagnini, "A hypoplastic macroelement model for shallow foundations under monotonic and cyclic loads," *Acta Geotechnica*, vol. 4, no. 3, pp. 163–176, 2009.

[92] G. Buscarnera, R. Nova, M. Vecchiotti, C. Tamagnini, and D. Salciarini, "Settlement analysis of wind turbines," *Soil-Foundation-Structure Interaction*, p. 163, 2010.